Frequency Domain Algorithms For Simulating Large Signal Distortion in Semiconductor Devices

A DISSERTATION

SUBMITTED TO THE DEPARTMENT OF ELECTRICAL ENGINEERING

AND THE COMMITTEE ON GRADUATE STUDIES

OF STANFORD UNIVERSITY

IN PARTIAL FULFILLMENT OF THE REQUIREMENTS

FOR THE DEGREE OF

DOCTOR OF PHILOSOPHY

By

Boris Troyanovsky

November 1997

I certify that I have read this dissertation and that in my opinion it is fully adequate, in scope and quality, as a dissertation for the degree of Doctor of Philosophy.

Robert W. Dutton (Principal Advisor)

I certify that I have read this dissertation and that in my opinion it is fully adequate, in scope and quality, as a dissertation for the degree of Doctor of Philosophy.

Zhiping Yu (Associate Advisor)

I certify that I have read this dissertation and that in my opinion it is fully adequate, in scope and quality, as a dissertation for the degree of Doctor of Philosophy.

Abbas El-Gamal

Approved for the University Committee on Graduate Studies:

Abstract

The rapid growth of wireless communication systems has placed increasing demands on the design of semiconductor devices for analog applications. In particular, large signal distortion effects are of critical importance in microwave and RF communication circuitry. Physics-based device-level simulation of these effects can be an important aid in the analog device design process. However, the transient analysis capability present in traditional semiconductor device simulators is inadequate for large signal distortion analysis. The most notable shortcomings of conventional transient analysis are its inability to directly capture the steady state response of systems driven by quasiperiodic inputs, along with its poor performance in the presence of widely separated spectral components.

To address the aforementioned shortcomings of traditional time domain methods, a harmonic balance analysis capability was added to the PISCES-II device simulator. Harmonic balance, a frequency domain steady state solution technique for analyzing nonlinear systems, is well-suited for high-frequency analog applications such as RF and microwave communication systems. Algorithms for applying the harmonic balance method to large-scale systems of semiconductor device equations are presented, and the suitability of the techniques for practical problems is demonstrated. In particular, Krylov subspace solution techniques with special-purpose preconditioners are introduced to solve the large systems of equations that arise. Algorithms for reduced memory usage are presented. Device-level harmonic balance analysis is applied to simulating harmonic and intermodulation distortion in industrial device structures, and the simulation results are compared to experimental measurements. Competing algorithms, such as the circuit envelope technique and the shooting method, are briefly reviewed and compared to harmonic balance.

Acknowledgments

I would like to express my deepest gratitude to Professor Robert W. Dutton, my advisor, for his guidance, advice, and support throughout the course of my graduate studies. The thesis topic and the direction of this work are direct products of his suggestions and ideas. I would also like to thank Professor Zhiping Yu, my associate advisor, for providing constant encouragement, technical advice, and countless valuable suggestions during the course of this research.

I would like to acknowledge the support I've received during the past two years from many co-workers at Hewlett-Packard's EEsof Division. Dr. Niranjan Kanaglekar, my project manager, and Jeffrey W. Meyer, my section manager, have both been extremely supportive. I'd like to thank David D. Sharrit for the many clear, concise technical explanations he's supplied over the years on numerous topics in circuit simulation. Dr. Marek Mierzwinski's advice and assistance is also gratefully acknowledged. During the early portion of my graduate studies, I benefited greatly from summers spent at Hewlett-Packard Laboratories. I would like to express my appreciation to Dr. Norman Chang, Dr. Gregory Gibbons, Dr. Lee Barford, Dr. Richard Dowell, Randy Coverstone, Dr. Ken Lee, and Al Barber for the valuable learning experience.

During my graduate studies at Stanford, I was fortunate enough to collaborate with several very talented industrial partners. I would like to especially thank Ms. Junko Sato-Iwanaga of Matsushita Electronics Corporation for providing numerous simulation examples and critically important feedback regarding this research. Dr. Torkel Arnborg of Ericsson Components provided additional examples and some much-appreciated enthusiasm and motivation. Toward the latter stages of this work, it has been a pleasure to work with Francis M. Rotella in integrating the harmonic balance module into his mixed-level circuit / device PISCES simulator. Many thanks go to Alvin Loke, Anthony Chou,

Freddy Sugihwo, Adrian Ong, Maria Perea, and Fely Barrera for helping to make my Stanford experience an enjoyable one.

I would like to thank Professor Abbas El-Gamal for being a member of my oral thesis defense committee, and for being a 3rd reader of this manuscript. I would also like to thank Professor David A. B. Miller for serving as the oral defense chairman.

Most of all, I would like to express my appreciation to my parents, Alex and Inna, for their overwhelming love and kindness during these first twenty-seven years of my life. This thesis is dedicated to them.

To my parents

Chapter 1

Chapter 2

Chapter 3

Chapter 5

Chapter 6

Chapter 7

List of Tables

List of Figures

Chapter 1

Introduction

Semiconductor device simulation has played a key role in the design and development of novel device structures and technologies. Although analog device designs have benefited greatly from physics-based device simulation, the important area of large signal steady-state analysis has been somewhat neglected by the device simulation community. With the rapid growth of wireless communication systems and other analog designs where harmonic distortion is critical, there has been an ever-increasing need for such analysis capabilities at the device simulation level.

This work presents algorithms, results, and application examples aimed at solving nonlinear frequency domain steady-state device simulation problems. Stanford University's popular device simulator, PISCES-II [10], is extended to support a harmonic balance analysis capability. Harmonic balance, a frequency domain steady state analysis method for nonlinear systems, is well-suited for high-frequency analog applications such as RF and microwave communication systems. Algorithms for applying the harmonic balance method to large scale systems of semiconductor device equations are presented, and the suitability of the techniques for practical problems is demonstrated.

1.1 Background

Analog circuit designers have long recognized the drawbacks and limitations of SPICE-like [12] transient analysis. Although extremely effective on many problems, traditional time domain approaches often fall short when applied to simulating the steady state response of systems with long time constants or widely separated spectral components. Many analog designs require the simulation of steady-state quantities such as harmonic distortion, and fall precisely into the aforementioned domain. The presence of stiff bias elements (such as RF chokes and blocking capacitors) along with potentially narrowband high-Q filters introduces the long time constants, and thus necessitates simulation over a prohibitively large number of periods to reach steady state. In addition, many high-frequency linear elements accounting for dispersion, loss, and parasitic components are extremely difficult to model in the time domain.

The recognition of these difficulties by high-frequency circuit designers has led to demand for and the development of alternate circuit simulators over the past decade. Harmonic balance [21][22][27], a nonlinear frequency domain analysis technique, has emerged as a widely accepted solution to many of the shortcomings that conventional time domain simulators have in the high-frequency analog arena. With the introduction of UC Berkeley's nonlinear frequency domain Spectre simulator [27], and the development of commercial harmonic balance simulators by Hewlett-Packard, EEsof[1], and Compact Software, nonlinear frequency domain analysis has assumed its current position as the method of choice for simulating most nonlinear microwave designs, and for analyzing a large number of the RF designs as well.

1.2 Motivation

To demonstrate the inherent limitations of transient analysis in the context of RF simulation, we present an illustrative example. The example is a small mixer circuit which highlights the major problem areas associated with standard time domain simulation algorithms. In this section, we will approach the example from a circuit-level perspective,

1. Subsequently acquired by Hewlett-Packard.

since the points made are equally applicable to both the circuit and device simulation areas. Subsequent chapters will focus on the problem from a device-level perspective, and the example will be revisited in the context of device simulation in Section 6.3.

The circuit configuration shown in Figure 1.1 below is designed to downconvert an RF

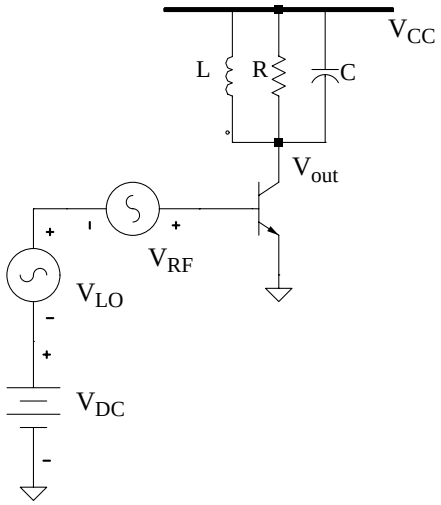

Figure 1.1 A single-transistor downconverting mixer circuit. The resonant filter is tuned to the difference of the RF and LO frequencies.

signal at some frequency f_{rf} to an output IF signal at frequency $f_{if} = f_{rf} - f_{lo}$. The downconversion is accomplished by mixing the RF input with a local oscillator (LO) sinusoid having frequency $f_{lo} < f_{rf}$. In addition to the desired IF output signal, the BJT nonlinearities introduce large undesired harmonic distortion products at $2f_{if}$, $3f_{if}$, ..., along with an LO feedthrough term at f_{lo} [1]. The purpose of the tuned RLC filter is to remove these undesired distortion products from the output waveform, while retaining the desired signal at f_{if}. The center frequency of the filter

1. In general, the harmonic content of the IF output signal will include terms of the form $mf_{rf} + nf_{lo}$ for integer combinations of *m* and *n*.

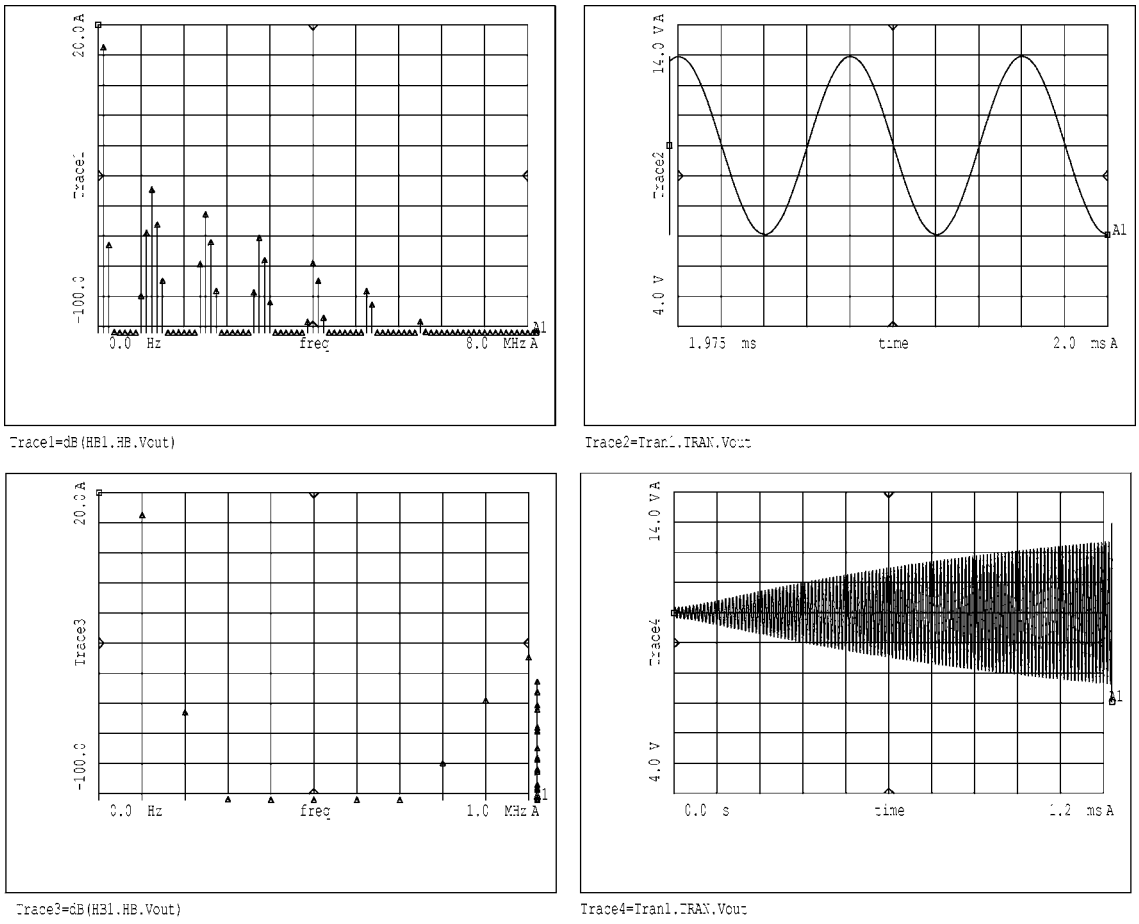

Figure 1.2 Simulation results for Q=100. The two plots on the left side show the IF output spectrum at steady state. The top plot on the right side illustrates the time domain IF waveform once steady state has been reached, while the bottom right plot shows the transient build-up.

$$f_0 = \frac{1}{2\pi\sqrt{LC}} \tag{1.1}$$

must be chosen such that $f_0 = f_{if}$, and the quality factor

$$Q = R\sqrt{\frac{C}{L}} \tag{1.2}$$

needs to be selected so that the bandwidth of the filter ($f_{bw} = f_0/Q$) is tight enough to remove the distortion components at frequencies of $2f_{if}$ and above.

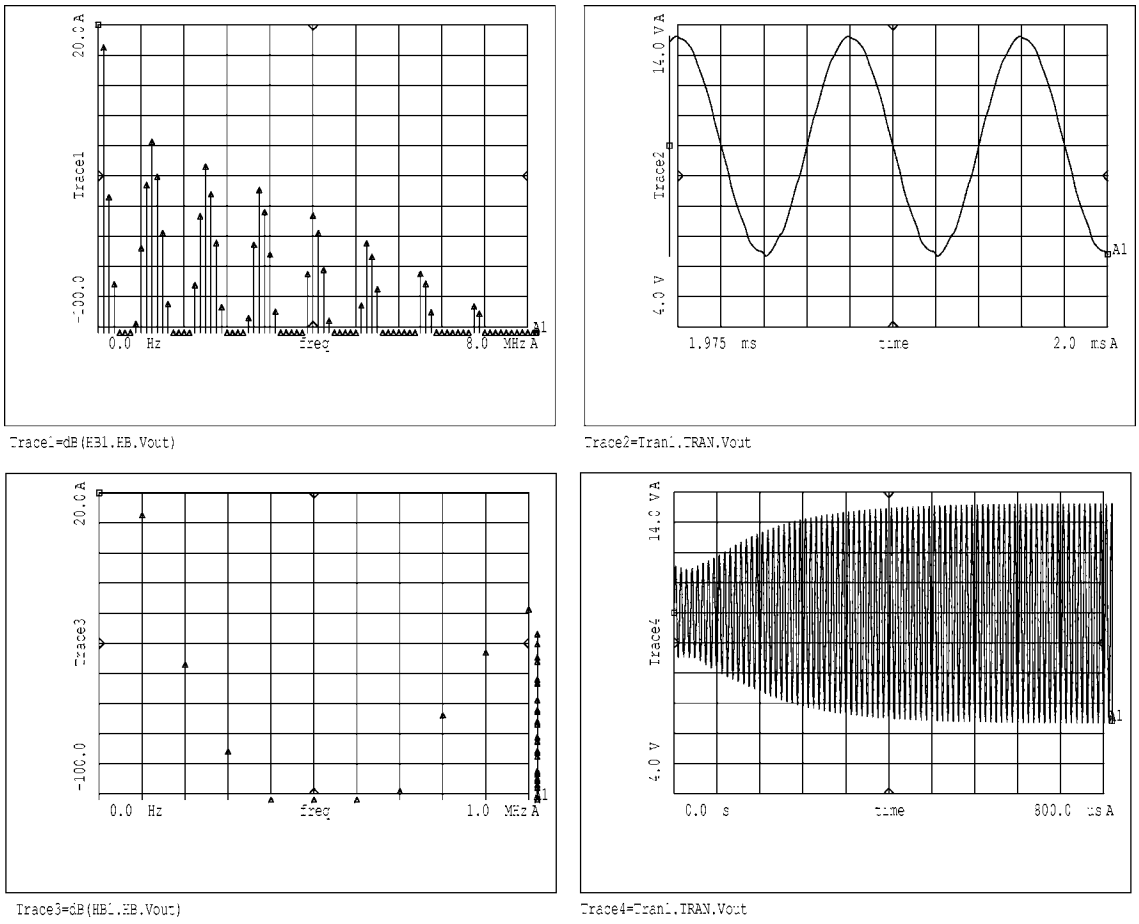

Figure 1.3 Simulation results for Q=40. The two plots on the left side show the IF output spectrum at steady state. The top plot on the right side illustrates the time domain IF waveform once steady state has been reached, while the bottom right plot shows the transient build-up.

Figure 1.2 and Figure 1.3 show simulation results obtained with HP's Microwave Design System [13] for Q values of 100 and 40, respectively, with R = 15 kΩ, f_{rf} = 1.1 MHz, f_{lo} = 1.0 MHz, and f_{if} = 100 kHz. The two plots on the left side of each figure show the harmonic content of the IF output waveform at steady state, with the lower left plot containing a zoomed-in version (0 Hz - 1 MHz) of the upper left plot. The plots on the right side of each figure show the corresponding time domain results, with the upper right

plot showing the IF waveform after steady state has been reached, and the lower right plot showing the transient build-up to steady state.

Transient analysis faces two major difficulties in coping with examples such the one presented here. The first of these difficulties has to do with the potentially long time constants introduced by passive components like high-Q (narrowband) filters. Because analog circuit designers are typically interested in the steady state response of nonlinear systems, a conventional time domain simulator must integrate over the start up transients until they decay to the point where they are negligible. The lower-right plot of Figure 1.2 shows the initial transient behavior when the Q of the RLC filter is 100. As expected, the corresponding plot of Figure 1.3 shows that the transient region is smaller when the Q is reduced to 40. Long time constants are not restricted solely to narrow bandwidth filtering circuitry; they also arise in connection with other passive elements (such as RF chokes and DC blocks) critical to many RF circuits.

A second major difficulty faced by standard transient simulators has to do with the wide range of frequencies present in many practical RF and microwave circuits. For example, the IF frequency of the example in this section is 100 kHz, which corresponds to a period of 10 μs. The RF frequency, on the other hand, is at 1.1 MHz, corresponding to a period of less than 1 μs. Furthermore, harmonics of the RF and LO must be accounted for, potentially pushing the associated period to around 0.1 μs if, for example, 9 harmonics are needed. This wide disparity in the length of the periods means that transient simulators must integrate over a large number of time points to cover a full IF period (see the lower right plots of the figures above for an illustration). Furthermore, as we saw in the preceding paragraph, the simulator must cover many periods of the IF signal in order to reach steady state. It should be pointed out that the example frequencies chosen in this section actually *understate* the problems faced by transient analysis. In reality, it is very common to encounter microwave systems having signals that include spectral components ranging from the kHz to the GHz range. We picked a relatively low RF frequency only for ease of plotting and presenting the data.

1.3 Overview and Outline

The shortcomings of conventional transient analysis at the RF/microwave circuit level have led to the development of nonlinear frequency domain simulation techniques such as

harmonic balance. The goal of this work is to extend the applicability of harmonic balance to the semiconductor device simulation level. By far the largest obstacle to employing harmonic balance for device simulation problems is the extremely large size and relatively high density of the semiconductor device Jacobian when compared to its circuit counterpart. We will demonstrate that this obstacle can be overcome through use of algorithms that carefully exploit the special structure of the device Jacobian.

This thesis consists of seven chapters. The current chapter presents the background and motivation for this work, and outlines the organization of the thesis. Chapter 2 then proceeds to give an overview of the kinds of nonlinear state equations that arise in circuit and device simulation, along with a discussion of how the nonlinearities lead to large signal distortion. Some standard metrics and figures of merit (e.g., gain compression and intercept points) commonly used by RF and microwave designers are briefly discussed. The details of formulating the constitutive equations for both circuit and semiconductor device simulation problems are then presented, including a subsection on how mixed circuit- and device-level simulation matrices may be formulated. The chapter concludes with a brief discussion of standard transient methods that can be used for solving the nonlinear state equations.

The harmonic balance algorithm is presented in Chapter 3. Solution methods based on direct factorization techniques are discussed, and shown to be inadequate for handling the large Jacobians encountered in HB-based device analysis. Algorithms to successfully cope with these kinds of problems are developed in Chapter 4. Linear iterative solvers (in particular, the GMRES algorithm) are employed in conjunction with special-purpose preconditioners developed specifically for semiconductor device applications. Specific techniques for efficiently applying Krylov subspace solution methods to the device-level harmonic balance problem are discussed.

The algorithms of Chapter 4 are the foundation on which this work is based; Chapter 5 provides an overview of two competitive algorithms that have unique strengths and weaknesses relative to the methods of Chapter 4. The algorithms reviewed are circuit envelope simulation and the matrix-implicit shooting method. These are compared to the harmonic balance algorithms chosen as the foundation of this work.

Chapter 6 provides several practical examples originating from both industrial and academic sources. These provide valuable benchmark data, and serve as testimonials to the code’s applicability to solving realistic problems. Examples include both amplifiers

and mixers, with device technologies ranging from silicon BJTs and MOSFETs to GaAs MESFET structures. The thesis concludes with Chapter 7, which summarizes the work and discusses directions for future research.

Chapter 2

Nonlinear State Equations and Large Signal Distortion

Nonlinearities are absolutely critical to the proper operation of analog communication circuits. In some applications, such as in highly linear amplifier design, the goal is to generate an amplified replica of the input signal, and minimize any nonlinear effects that lead to distortion of the waveform. In other designs, such as mixers or frequency-doublers, nonlinearities are purposely used to introduce desired frequency-translated components into the output signal. In the latter case, undesired spurious products are minimized through careful design and the use of balancing and/or linear filtering techniques.

In this chapter, we review the static and dynamic mechanisms responsible for nonlinear distortion, as well as several ‘‘figures of merit’’ related to characterizing the levels of distortion present in a given system. There are several levels of hierarchy that can be used in modeling nonlinear components — the behavioral (or system) level, the circuit level, and the physical device level. At the circuit and system level, a given ‘‘compact model’’ typically consists of less than a dozen or so state variables, and is based on either phenomenological or approximate physics-based analysis [17][18]. In this work, we primarily concentrate our efforts at the physical device level, where the model is based on solution of partial differential equations, and the number of time domain state variables is in the thousands.

2.1 Large Signal Distortion

2.1.1 Nonlinearities, Power Series, and Distortion

As a simple but illustrative example, we consider the inverting single-transistor BJT amplifier of Figure 2.1. At low frequencies, the device can be modeled to first order by the equations accompanying the schematic below:

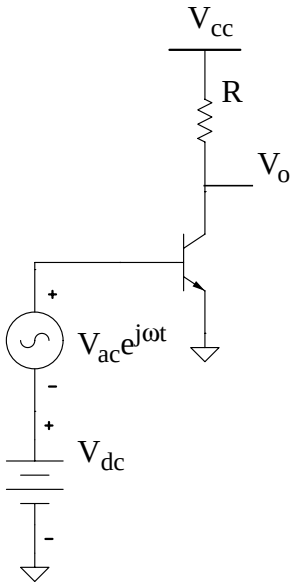

$$I_C = I_S \exp\left(\frac{qV_{BE}}{kT}\right)$$

$$I_B = \frac{I_S}{\beta} \exp\left(\frac{qV_{BE}}{kT}\right)$$

$$I_E = -\left(1 + \frac{1}{\beta}\right) I_S \exp\left(\frac{qV_{BE}}{kT}\right)$$

Figure 2.1 Inverting BJT amplifier biased in the forward active region of operation.

By inspection, the unloaded response of the amplifier under large signal ac drive is

$$V_0 = V_{cc} - I_S R \exp\left(\frac{qV_{dc}}{kT}\right) \exp\left(\frac{qV_{ac}\cos(\omega t)}{kT}\right), \tag{2.1}$$

and the incremental voltage (the instantaneous voltage minus the quiescent value) is

$$v_0 = I_S R \exp\left(\frac{qV_{dc}}{kT}\right)\left(1 - \exp\left(\frac{qV_{ac}\cos(\omega t)}{kT}\right)\right). \tag{2.2}$$

Letting $a_0 = -I_S R \exp(qV_{dc}/kT)$ and $\hat{V}_{ac} = qV_{ac}/kT$ for notational convenience, and using the standard Taylor series expansion for $\exp(x)$, we obtain

$$v_0 = a_0 \sum_{n=1}^{\infty} \frac{1}{n!} (\hat{V}_{ac}\cos(\omega t))^n. \tag{2.3}$$

Assuming the input signal is small enough such that only the first three terms of (2.3) are significant, v_0 can be approximated as

$$\frac{v_0}{a_0} \approx \frac{1}{4}\hat{V}_{ac}^2 + \left(\hat{V}_{ac} + \frac{1}{8}\hat{V}_{ac}^3\right)\cos(\omega t) + \frac{1}{4}\hat{V}_{ac}^2\cos(2\omega t) + \frac{1}{24}\hat{V}_{ac}^3\cos(3\omega t)\ . \qquad (2.4)$$

In the limit of infinitesimally small AC input, the terms involving $\hat{V}_{ac}^2$ and $\hat{V}_{ac}^3$ become negligibly small, and the amplifier responds with an output incremental voltage at the fundamental frequency only:

$$\frac{v_0}{V_{ac}} \rightarrow \frac{q}{kT}a_0\cos(\omega t)\ . \qquad (2.5)$$

As the AC drive level is increased, distortion components begin to appear at harmonics of the fundamental, and at DC. The level of distortion that can be tolerated in a given circuit depends on the specific application involved, and must be weighed by the designer against other design priorities.

An interesting and important characteristic to observe in (2.4) is that the amplitudes of the various harmonics are completely independent of input frequency. As we will see in more detail later, this is a general property of resistive nonlinearities — i.e., nonlinearities that are not frequency dependent.

2.1.2 Multi-Tone Distortion and Intermodulation

In the preceding section, the large signal AC input was restricted to a single fundamental frequency. As is evident from (2.4), the distortion components produced by this single-tone stimulus are all harmonics of the fundamental frequency. When the input consists of two or more independent tones, additional distortion components are produced. Such distortion terms arise from nonlinear ‘‘mixing’’ of the independent input tones, and are often referred to as intermodulation products, spurious harmonics, or mixing terms.

Referring back to the example of Figure 2.1, we consider the case where the input AC signal is composed of two sinusoids at independent frequencies ω_A and ω_B:

$$v_{in}(t) = V_A\cos(\omega_A t) + V_B\cos(\omega_B t) \qquad (2.6)$$

Introducing the normalized amplitudes $\hat{V}_A = qV_A/kT$, $\hat{V}_B = qV_B/kT$, and using the power series (2.3) allows us to write the amplifier’s incremental output voltage as

$$v_0 = a_0 \sum_{n=1}^{\infty} \frac{1}{n!}\left(\hat{V}_A \cos(\omega_A t) + \hat{V}_B \cos(\omega_B t) \right)^n . \tag{2.7}$$

If, as before, the power series is approximated by its first three terms,[1] we obtain the following rather unwieldy but informative expression:

$$\begin{aligned}
\frac{v_0}{a_0} \approx{}& \frac{1}{4}\hat{V}_A^2 + \frac{1}{4}\hat{V}_B^2 \\
&+ \left(\hat{V}_A + \frac{1}{8}\hat{V}_A^3 + \frac{1}{4}\hat{V}_A\hat{V}_B^2 \right)\cos(\omega_A t) + \left(\hat{V}_B + \frac{1}{8}\hat{V}_B^3 + \frac{1}{4}\hat{V}_A^2\hat{V}_B \right)\cos(\omega_B t) \\
&+ \frac{1}{4}\hat{V}_A^2 \cos(2\omega_A t) + \frac{1}{4}\hat{V}_B^2 \cos(2\omega_B t) \\
&+ \frac{1}{24}\hat{V}_A^3 \cos(3\omega_A t) + \frac{1}{24}\hat{V}_B^3 \cos(3\omega_B t) \\
&+ \frac{1}{8}\hat{V}_A\hat{V}_B^2 \cos(\omega_A t - 2\omega_B t) + \frac{1}{8}\hat{V}_A^2\hat{V}_B \cos(2\omega_A t - \omega_B t) \\
&+ \frac{1}{2}\hat{V}_A\hat{V}_B \cos(\omega_A t - \omega_B t) + \frac{1}{2}\hat{V}_A\hat{V}_B \cos(\omega_A t + \omega_B t) \\
&+ \frac{1}{8}\hat{V}_A^2\hat{V}_B \cos(2\omega_A t + \omega_B t) + \frac{1}{8}\hat{V}_A\hat{V}_B^2 \cos(\omega_A t + 2\omega_B t)
\end{aligned} \tag{2.8}$$

Thus, in addition to harmonic distortion components at $\omega_A, 2\omega_A, 3\omega_A, \ldots$ and $\omega_B, 2\omega_B, 3\omega_B, \ldots$, there are also new intermodulation product terms at the frequencies $\omega_A \pm \omega_B, 2\omega_A \pm \omega_B, \omega_A \pm 2\omega_B, \ldots$. More generally, input sources at M independent fundamentals can be expected to introduce distortion components at integer combinations of the independent driving frequencies (see (3.14)).

An intermodulation component at a given frequency $k_A\omega_A + k_B\omega_B$ is said to have order $|k_A| + |k_B|$. For example, the distortion terms at frequencies $2\omega_A$ and $\omega_A \pm \omega_B$ are second-order products, whereas the components at $3\omega_B$, $2\omega_A \pm \omega_B$, and $\omega_A \pm 2\omega_B$ are third-order. From equation (2.8) (which we stress again is valid only for low AC drive levels), we see that distortion products of order *m* are polynomials of order *m*. This is a

1. Symbolic analysis packages such as Mathematica [73] can conveniently simplify complex algebraic expressions. Equation (2.8) was obtained with Mathematica's Expand[, Trig->True] function.

general property which is used in the subsequent section to compute so-called intercept points, a widely used metric for distortion in nonlinear systems.

2.1.3 Characterizing Large Signal Distortion

There are several commonly used metrics, or figures of merit, for quantifying the levels of distortion present in a given waveform. For single-tone distortion measurements, the *n*th harmonic distortion factors HD_n are widely employed. Given a waveform with Fourier expansion

$$v(t) = \Re e\{V_0 + V_1 \exp(j\omega t) + V_2 \exp(j2\omega t) + V_3 \exp(j3\omega t) + \ldots\}, \qquad (2.9)$$

HD_n is defined to be the magnitude of the ratio of the nth harmonic to the fundamental:

$$HD_n = \left|\frac{V_n}{V_1}\right|, \; n \geq 2. \qquad (2.10)$$

For example, the amplifier response of (2.4) has a second-harmonic distortion factor of

$$HD_2 = \frac{\hat{V}_{ac}}{4 + \frac{1}{2}\hat{V}_{ac}^2} \qquad (2.11)$$

To characterize the level of distortion in the entire waveform (as opposed to the distortion at a given harmonic), the total harmonic distortion (*THD*) is defined to be

$$THD = \frac{\sqrt{\sum_{n=2}^{\infty} |V_n|^2}}{|V_1|} \qquad (2.12)$$

The values of THD that can be tolerated in a given design are highly application-dependent. In audio applications, for example, the THD must typically be kept well below 0.01, or 1%.

When the driving signal is multi-tone, intermodulation terms are introduced into the response. For these spurious terms, the *n*th order intermodulation distortion factors IM_n are defined analogously to the HD_n. A key difference in the multi-tone case, however, is that there are, in general, several different frequency components having the same order. For example, we see from (2.8) that there are 6 distinct third-order terms at frequencies $3\omega_A$, $3\omega_B$, $2\omega_A + \omega_B$, $2\omega_A - \omega_B$, $\omega_A + 2\omega_B$, and $\omega_A - 2\omega_B$. Four of these are intermodulation, or mixing, products, with the remaining two being harmonics of a

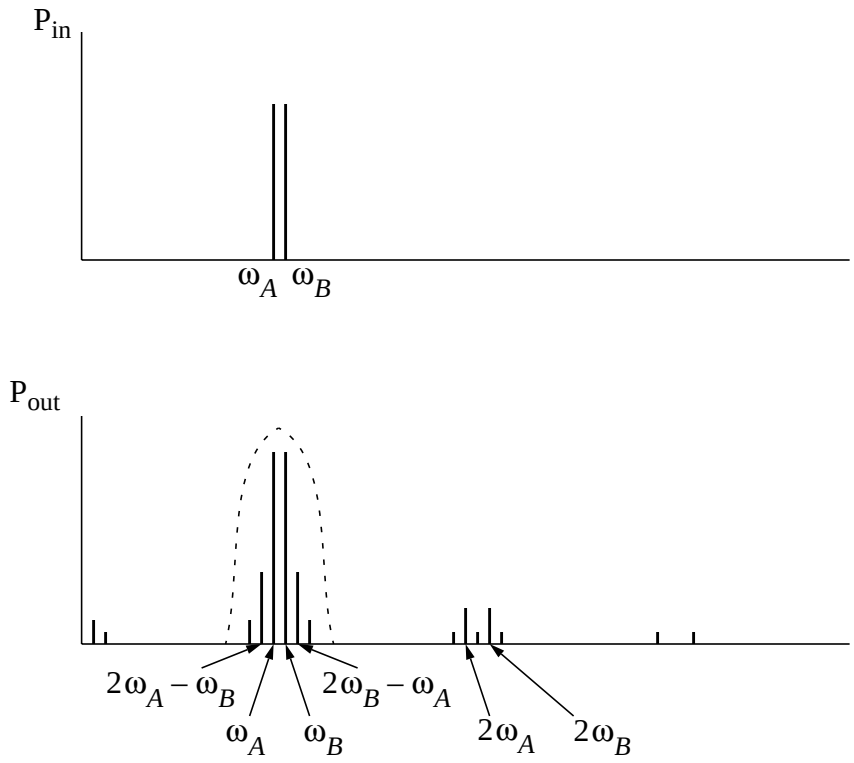

Figure 2.2 A two-tone test of a (hypothetical) bandpass amplifier. The two-tone input signal (top) generates a spectrum of harmonics at the output (bottom). Note the third order terms landing within the passband — unlike the second order terms, they cannot be easily filtered out.

fundamental. Thus, in specifying a value for IM_n, it is also necessary to state which particular third-order harmonic is being used, along with which fundamental is intended as the ‘‘real output’’ for use in the ratio.

The choice of frequencies used to define IM_n, along with the distortion order n of interest, is application-dependent. Consider a narrowband amplifier, for instance. A common distortion test in this case is to apply two very closely spaced input signals of equal amplitude at frequencies ω_A and ω_B, such that both are within the amplifier passband. The third-order distortion products falling at frequencies $2\omega_A - \omega_B$ and $2\omega_B - \omega_A$ are of primary interest in this example, since they fall directly in the passband (Figure 2.2). Letting $V_A = V_B = V_{tst}$, and using the approximate low-distortion model of (2.8), we obtain

$$IM_3 = \frac{\hat{V}_{tst}^2}{8 + 3\hat{V}_{tst}^2} \tag{2.13}$$

In this example, the numerical value of IM_3 is the same regardless of whether $2\omega_A - \omega_B$ or $2\omega_B - \omega_A$ is used. In general, however, the IM_3 value may be different for these two frequencies, in which case an explicit distinction must be made. For instance, another common test used for receiver design employs a small ‘‘desired’’ signal at a frequency ω_A, while a large ‘‘interfering’’ (sometimes called blocking, or jamming) signal is applied at a nearby frequency ω_B to determine the third-order distortion that is introduced. In this case, the asymmetry in input signals will produce different values of IM_3 at the various third-order terms. Similarly, linear and nonlinear frequency dependent elements may introduce such asymmetries even in the case of identical input amplitudes.

2.1.4 Gain Compression and Intercept Points

The simplified transistor model of Figure 2.1 is valid only in the forward active region of operation, and even then only in the low-distortion regime. As AC power is increased, the collector voltage will swing low enough at the peak of the input sinusoid to send the transistor into saturation. In addition to introducing even more distortion components, this phenomenon will also compress the gain of the amplifier. Gain compression is an effect that is of significant interest to the analog designer, and is an important metric for determining the distortion properties of nonlinear systems.

Figure 2.3 shows the general shape of input-output power curves for a typical amplifier. P_{in} is defined to be the available power of the fundamental input tone

$$P_{in} = \frac{|V_{ac}|^2}{8R_s} \tag{2.14}$$

where R_s is the source resistance; P_{out} is defined to be the rms power dissipated in the load. Depending on the application, the second- and third-order distortion components plotted in the figure may correspond either to harmonics of the fundamental, or to specific intermodulation components (Section 2.1.3).

As equations (2.4) and (2.8) indicate, the slopes of the first-, second-, and third-order components in the low-power linear region on a log-log plot are 1 dB/dB, 2 dB/dB, and 3 dB/dB, respectively. In Figure 2.3, dashed lines are used to extrapolate the slopes to higher

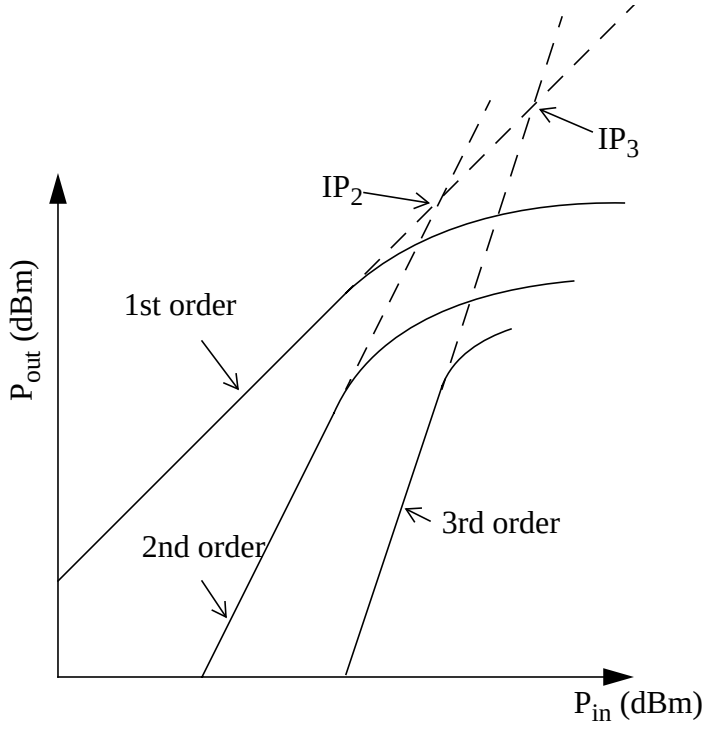

Figure 2.3 Input-output power curves for the first-, second-, and third-order distortion terms for a typical amplifier.

power levels. The gain compression at a given input power level is defined to be the value of the extrapolated (dashed) extension of the first-order distortion term divided by its actual compressed value (solid line). The 2nd-order intercept point (sometimes referred to as SOI, for ‘‘second-order intercept’’) is the intersection of the first- and second-order linear extrapolations. Similarly, the 3rd-order intercept point (TOI) is defined to be the intersection of the first- and third-order extrapolations. Arbitrary *n*th order intercept points may be defined in an analogous manner.

Before concluding this section, we point out a few implicit assumptions regarding intercept-point measurements. The first of these assumptions is that the input amplitudes in the multi-tone input case must track each other during the power sweep for the slope relations of the preceding paragraph to hold true. The second assumption is that the linear low-power region is identifiable in the general case. While this is certainly true in the simulation domain, actual physical measurements of real-world systems may show some

ripple and curvature all the way down to the noise floor. Nevertheless, most practical systems do have identifiable linear regions, and the definition of intercept points can be made such that the concept has validity.

2.2 The Large Signal Steady State

The purely resistive nonlinearities examined in Section 2.1 are not adequate for representing realistic systems operating under time-varying inputs.[1] Additional dynamic effects arising from linear and nonlinear capacitors and inductors, filtering circuitry, parasitics, and transmission lines are critical to proper modeling, and must be carefully accounted for by any accurate simulation tool. Some dynamic elements, especially linear components such as large inductors (RF chokes), large capacitors (DC blocks), and narrowband filters can introduce extremely long time constants into a circuit network. Since the analog designer is usually most interested in steady state quantities, time domain transient simulators must be run until all the start-up transients have died out. In the subsections below, we define the meaning of steady state solutions and briefly examine some dynamic effects that illustrate the usefulness of steady state solution algorithms like harmonic balance.

2.2.1 The Various Types of Steady State

A steady state solution of a system of differential equations is a solution that is asymptotically approached as the effect of the initial conditions dies out [27][33]. In general, a given system of differential equations can have no steady-state solutions, a single steady state solution, or several such solutions. In the latter case, the actual solution seen will depend upon the initial conditions. Most practical analog designs will have at least one steady state solution.

There are several types of steady state problems which are of interest in analog applications. The first of these is the DC steady state, where both the stimulus and the solution are constant in time. Strictly linear systems[2] driven by sinusoidal inputs will

1. At very low frequencies, however, purely resistive models can be adequate in the absence of very large capacitors and inductors.

reach an AC steady state, which consists of a sinusoid superposed on a DC offset term. Similarly, it is possible to assume that the AC input is infinitesimally small, linearize a nonlinear system of differential equations, and compute the small-signal AC response from this linearization. Both the DC and small-signal AC steady state problems are addressed by existing device simulation codes, and will not be discussed at length in this work.

The periodic large signal steady state results either from an external periodic stimulus (for non-autonomous systems such as amplifiers and mixers) or from a self-oscillation (for autonomous systems such as oscillators). In the periodic steady state, the solution state vector $\boldsymbol{x}(t)$ satisfies the periodicity condition

$$\boldsymbol{x}(t+T) = \boldsymbol{x}(t) \tag{2.15}$$

for $-\infty < t < \infty$ for some period T. Consequently, $\boldsymbol{x}(t)$ can be represented in the frequency domain by a countable (though possibly infinite) number of Fourier series terms. In practice, a finite number of Fourier harmonics is adequate for representing $\boldsymbol{x}(t)$ to any required degree of accuracy.

The quasiperiodic large signal steady state is similar to the periodic steady state of the preceding paragraph, with the exception that the stimulus and response frequencies need not be harmonically related. For instance, a nonlinear system driven by multiple sinusoids at harmonically unrelated frequencies will typically respond at the sum and difference frequencies of the driving tones. The resulting spectrum will consist of a countable number of spectral lines, corresponding to the quasi-Fourier components of the response.

It is possible for nonlinear systems to have steady-state responses that do not fit in any of the categories presented above (e.g., chaotic circuits [33]). Such systems are not representative of most practical analog designs, and are not considered in this work.

2.2.2 Distributed Linear Elements in the Sinusoidal Steady State

Distributed linear elements are a category of linear components that can be difficult to simulate outside the steady state, and can make the transient ‘‘settling time’’ (the time to reach steady state) prohibitively long. Distributed elements include transmission line components (possibly with dispersion or loss) to model high-frequency interconnects such

2. We assume here that the linear system is ‘‘passive’’ — i.e., that its eigenvalues lie exclusively in the left half plane.

as microstrip transmission lines, non-ideal power planes, and distributed filters. These distributed linear elements are best characterized in the frequency domain, where network analyzers or electromagnetic simulation tools can be used to extract S-parameter matrix descriptions as a function of frequency. Assuming a constant reference impedance Z_0 for all measurement ports, the S-parameter description of an *N*-port linear device takes the form [16]

$$\begin{bmatrix} V_1^-(\omega) \\ | \\ V_N^-(\omega) \end{bmatrix} = \begin{bmatrix} S_{11}(\omega) & \dots & S_{1N}(\omega) \\ | & \backslash & | \\ S_{N1}(\omega) & \dots & S_{NN}(\omega) \end{bmatrix} \begin{bmatrix} V_1^+(\omega) \\ | \\ V_N^+(\omega) \end{bmatrix} \tag{2.16}$$

where the incident voltage waves $V_n^+(\omega)$ are defined as

$$V_n^+(\omega) = \frac{1}{2}\left(V_n(\omega) + Z_0 I_n(\omega)\right) \tag{2.17}$$

and the reflected voltage waves $V_n^-(\omega)$ are defined as

$$V_n^-(\omega) = \frac{1}{2}\left(V_n(\omega) - Z_0 I_n(\omega)\right) \tag{2.18}$$

In the periodic or quasiperiodic steady state, it is trivial to operate with such frequency domain descriptions. Given a spectrum corresponding to, say, $V_n^+(\omega)$ as a sequence of phasors at the quasiperiodic frequencies of interest, the corresponding spectrum of $V_m^-(\omega)$ can be computed from (2.16) through complex-valued multiplications.

In the time domain, operations with constitutive equations of the form (2.16) are potentially much more problematic. The frequency domain products of the preceding paragraph become convolution integrals

$$v_m^-(t) = \sum_{n=1}^{N} \int_{-\infty}^{t} s_{mn}(t-\tau)\, v_n^+(\tau)\, d\tau \tag{2.19}$$

where $s_{mn}(t)$ is the impulse response (i.e., inverse Fourier transform) of $S_{mn}(\omega)$. Because the measured spectrum of $S_{mn}(\omega)$ consists of only a finite number of samples over a limited frequency range, construction of a passive and causal $s_{mn}(t)$ can prove to be non-trivial. In addition, the long transients associated with some impulse responses (such as those of high-Q narrowband filters) can make both the integration in (2.19) and the overall transient simulation very time consuming if it has to be run until steady state is reached.

2.3 Circuit-Level Modeling

Compact models used in circuit simulation typically consist of linear and nonlinear resistors, capacitors, and inductors. In time domain simulators capable of convolution-based analysis, distributed linear models (such as lossy, dispersive transmission lines) can also be described through impulse response matrices. A number of methods have been used to formulate the state equations in nonlinear circuit simulators. The most prominent of these methods include the sparse tableau approach and the modified nodal analysis (MNA) approach [35]. Because our ultimate focus is on device level simulation, we consider only the latter approach here, as it is more relevant to our needs. The reader is referred to [36] for a detailed exposition of the sparse tableau formulation.

An *N*-terminal device is a nonlinear resistive element if its constitutive equations take the form

$$\begin{aligned} i_1 &= g_1(v_1, v_2, \ldots, v_N) \\ i_2 &= g_2(v_1, v_2, \ldots, v_N) \\ &\vdots \\ i_N &= g_N(v_1, v_2, \ldots, v_N) \end{aligned} \quad . \tag{2.20}$$

In the two-terminal case, a nonlinear resistor's constitutive relation can be written as

$$i = g(v) \; . \tag{2.21}$$

At a given voltage v_0 across the resistor, the associated small-signal conductance is $g'(v_0)$. For the *N*-terminal resistive element, the small-signal admittance matrix is the $N \times N$ Jacobian of (2.20).

The constitutive equations for an *N*-terminal nonlinear capacitor are

$$\begin{aligned} i_1 &= \frac{d}{dt} q_1(v_1, v_2, \ldots, v_N) \\ i_2 &= \frac{d}{dt} q_2(v_1, v_2, \ldots, v_N) \\ &\vdots \\ i_N &= \frac{d}{dt} q_N(v_1, v_2, \ldots, v_N) \end{aligned} \quad , \tag{2.22}$$

where the functions q_n represent stored charge. The corresponding equations for a nonlinear inductor are simply the dual of (2.22), with nonlinear inductor flux functions φ_n taking the place of q_n:

$$\begin{aligned} v_1 &= \frac{d}{dt}\varphi_1(i_1, i_2, \ldots, i_N) \\ v_2 &= \frac{d}{dt}\varphi_2(i_1, i_2, \ldots, i_N) \\ &\vdots \\ v_N &= \frac{d}{dt}\varphi_N(i_1, i_2, \ldots, i_N) \end{aligned} \quad . \tag{2.23}$$

An important observation is that while nonlinear resistors (2.20) and nonlinear capacitors (2.22) are voltage-controlled elements, nonlinear inductors are current-controlled. Consequently, a state equation assembly method based on pure KCL nodal analysis is inapplicable to circuits containing inductors, since the inductor currents are not explicitly available as a function of the voltage state variables.

To overcome this limitation, the modified nodal analysis technique (MNA) [35] was introduced. Like straight KCL nodal analysis, MNA uses the voltages at every node as state variables. In addition, however, MNA augments the state vector with inductor currents as well. In assembling KCL equations at nodes connected to inductors, the inductor currents are summed into the appropriate node, and *N* extra branch equations of the form

$$\begin{aligned} v_1 - \frac{d}{dt}\varphi_1(i_1, i_2, \ldots, i_N) &= 0 \\ v_2 - \frac{d}{dt}\varphi_2(i_1, i_2, \ldots, i_N) &= 0 \\ &\vdots \\ v_N - \frac{d}{dt}\varphi_N(i_1, i_2, \ldots, i_N) &= 0 \end{aligned} \tag{2.24}$$

are introduced for every *N*-terminal inductor. As a concrete example, consider formulating the state equations at node 1 of Figure 2.4. The KCL equation at the node will be

$$g(v_3 - v_1) + i_L + \frac{d}{dt}q(v_2 - v_1) = 0\,. \tag{2.25}$$

In addition, a single branch equation will be introduced for the nonlinear inductor:

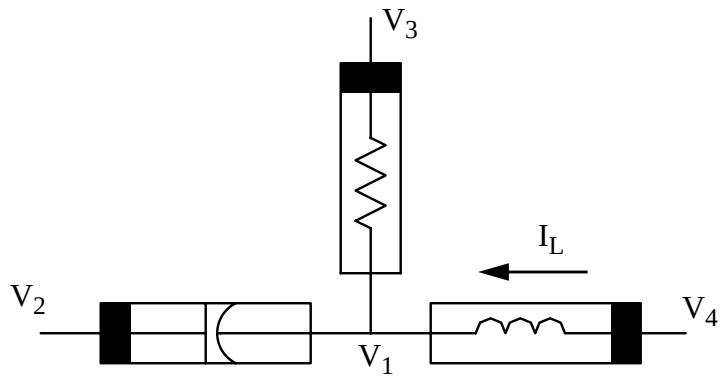

Figure 2.4 Formulating the state equations in the presence of current-controlled state elements.

$$i_L - \frac{d}{dt}\varphi(v_4 - v_1) = 0. \tag{2.26}$$

Constant current sources are readily incorporated by simply adding their values to the right hand side. Voltage sources are typically handled by introducing an additional auxiliary equation.[1] Assuming that a voltage source of value V_{app} is connected between nodes n_1 and n_2, a branch equation of the form

$$v_{n_1} - v_{n_2} - V_{app} = 0 \tag{2.27}$$

is added to the system of equations, and a new state variable i_{src} (representing the current through the voltage source) is summed into node n_1 and out of node n_2.

Taken together, the preceding steps in the MNA methodology result in systems of circuit state equations having form

$$\boldsymbol{g}(\boldsymbol{x}(t)) + \frac{d}{dt}\boldsymbol{q}(\boldsymbol{x}(t)) + y(t) \otimes \boldsymbol{x}(t) - \boldsymbol{w}(t) = 0, \tag{2.28}$$

where $\boldsymbol{x}(t)$ is a state vector of node voltages and inductor/voltage (branch) currents, $\boldsymbol{g}(\boldsymbol{x}(t))$ is the sum of nonlinear resistive and branch currents at each node, $\boldsymbol{q}(\boldsymbol{x}(t))$ is the vector of capacitor charges and inductor fluxes, and $\boldsymbol{w}(t)$ is a vector of voltage/

1. Optionally, voltage sources may be added by removing one of the voltage state variables that the voltage source is attached to, and symbolically setting the removed state variable to be equal to the sum of the remaining state variable and the voltage source. This approach has the disadvantage of not explicitly allowing the current through the source to be computed. However, it does have the advantage of reducing the number of state variables by 2.

current source excitations. The term $y(t) \otimes \boldsymbol{x}(t)$ is the nodal contribution of distributed devices handled through a convolution operation; $y(t) \in \Re^{N \times N}$ is a sparse matrix of time domain impulse responses which characterize the distributed devices present in the network.

2.4 Physics-Level Modeling of Semiconductor Devices

In the previous two sections, the large signal nonlinear steady state problem was examined from a circuit-level, compact model perspective. In this section, we show that the discretized partial differential equations modeling the physics of semiconductor devices have the same form (2.28) as the circuit equations. Furthermore, we will see that modified nodal analysis can be used to form the mixed-level circuit and device equations, while still retaining the basic form (2.28).

2.4.1 The Drift-Diffusion Equations

The drift-diffusion system of semiconductor equations takes the form

$$\nabla \bullet (-\varepsilon \nabla \psi) = q\left(p - n + N_D^+ - N_A^- \right) \tag{2.29}$$

$$\frac{\partial n}{\partial t} = \frac{1}{q} \nabla \bullet J_n - U$$

$$\frac{\partial p}{\partial t} = -\frac{1}{q} \nabla \bullet J_p - U$$

where in addition we have

$$J_n = qD_n \nabla n - q\mu_n n \nabla \psi \tag{2.30}$$

$$J_p = -qD_p \nabla p - q\mu_p p \nabla \psi$$

In the preceding equations, ψ represents the electrostatic potential, n and p are the electron and hole carrier concentrations, respectively, U is the recombination rate, N_D^+ and N_A^- are the ionized donor and acceptor concentrations, and J_n and J_p are the electron and hole current densities. External circuit elements (either lumped or distributed) may be included through the introduction of additional KCL/MNA equations, as will be shown in Section 2.4.5.

To numerically solve (2.29), we must first discretize the partial differential equations over the device domain, and convert them to a finite number of nonlinear differential-algebraic equations. For the drift-diffusion system of equations, each grid node *k* inside the device has three state variables associated with it: ψ_k, n_k, and p_k. In transient analysis, the time dimension is handled by a discretization as well. The focus of this thesis is on frequency domain simulation, where the time axis is not discretized (Chapter 3). Consequently, we review only the spatial discretization here, and defer handling the time dependencies until later.

2.4.2 Discretizing the Drift-Diffusion Equations

Numerous techniques exist for the spatial discretization of the semiconductor drift-diffusion equations. A detailed survey of these is beyond the scope of this work, which is focused more on the temporal dimension of the equations. Consequently, we present here only the most common algorithms for two-dimensional spatial discretization — those that are used by the PISCES simulator on which we base our work. Our goal is to establish a general mathematical form for the discretized system of algebraic equations, so that this form may be exploited in the derivations of subsequent chapters.

PISCES uses a spatial discretization scheme known as the ‘‘generalized box’’ (sometimes called ‘‘control volume’’ or ‘‘finite box’’) method [45]. The scheme is based on a finite-difference formulation, and is applied in the context of triangular grids. An example of such gridding applied to a bipolar device structure is shown in Figure 2.5. It is clear that a given rectangular grid can be transformed to a triangular grid by suitable partitioning of each rectangle into two triangular regions. As shown in the aforementioned figure, however, the grid need not in general be rectangular.

After a triangular mesh has been formed, the entire device domain is partitioned into non-overlapping ‘‘control volumes.’’ These are polygons, each corresponding to some node *k*, ideally having the property that the points within them fall into an area closer to node *k* than to any other node in the device domain. Given a triangular grid, a control volume partitioning may be readily established by splitting each triangle into three regions defined by the perpendicular bisectors of each side. As long as each triangle is acute (i.e., no angle is greater than $90°$), the partitioning satisfies the Voronoi condition that the control volume corresponding to a given node is closer to that node than to any other.

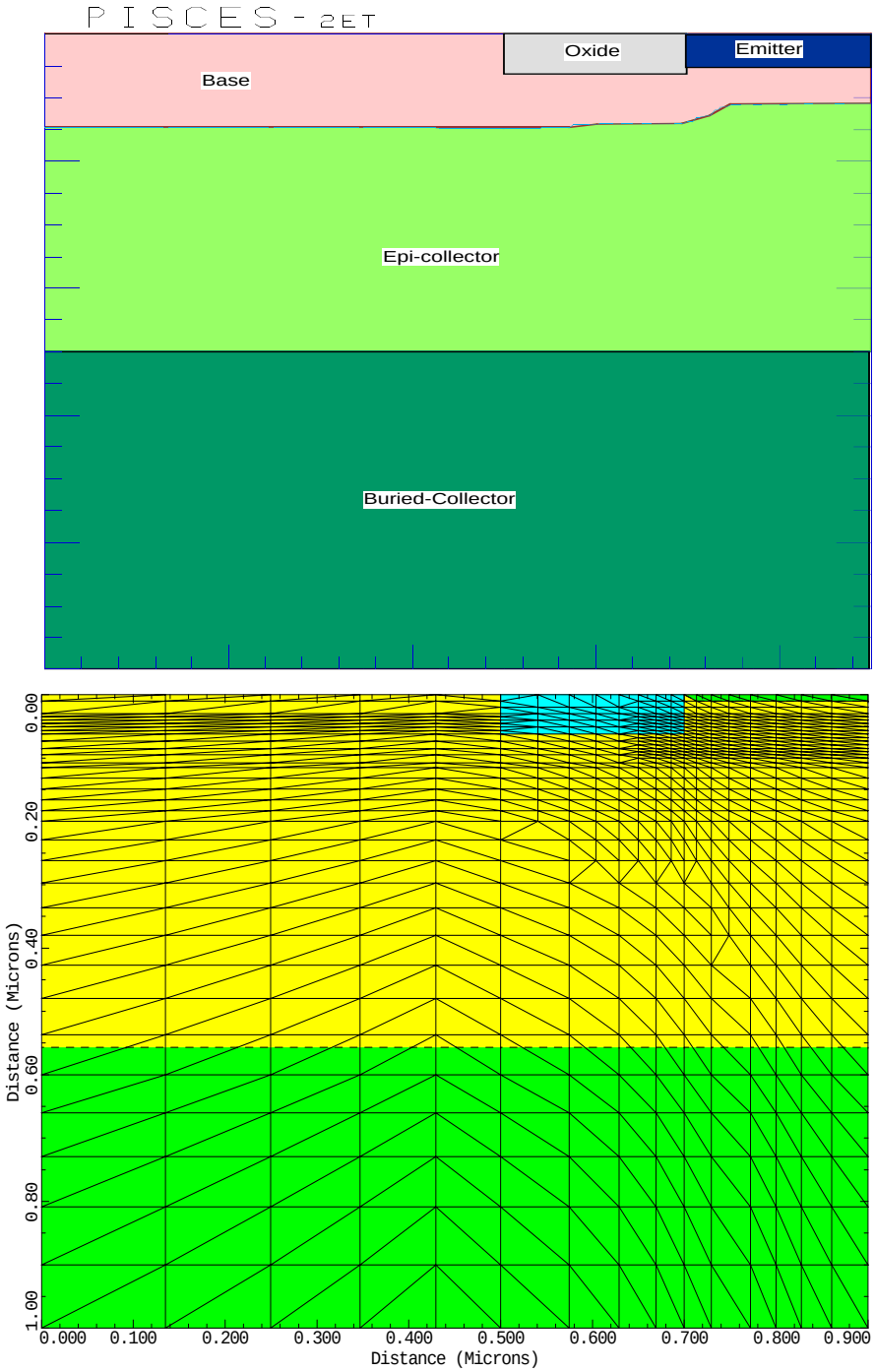

Figure 2.5 A bipolar transistor structure (top) and its triangular mesh (bottom).

However, if obtuse triangles exist, then the Voronoi condition may be violated, leading to some undesirable numerical consequences [45].

To discretize the semiconductor equations on a triangular grid, we first use the divergence theorem to express (2.29) in terms of integrals over the control volumes and surfaces. For each control volume A_k and surface $\partial\Omega_k$, the divergence theorem is applied to derive the three equations

$$\oint_{\partial\Omega_k} \varepsilon \boldsymbol{E} \cdot d\boldsymbol{S} = \iint_{A_k} q\left(p - n + N_D^+ - N_A^- \right) dA \tag{2.31}$$

$$\oint_{\partial\Omega_k} \boldsymbol{J}_n \cdot d\boldsymbol{S} = \iint_{A_k} q\left(U + \frac{\partial n}{\partial t} \right) dA$$

$$\oint_{\partial\Omega_k} \boldsymbol{J}_p \cdot d\boldsymbol{S} = \iint_{A_k} -q\left(U + \frac{\partial p}{\partial t} \right) dA$$

where for simplicity we've made use of the relation between electric field and electrostatic potential, $\boldsymbol{E} = -\nabla\psi$. To integrate the surface integrals on the left-hand side of (2.31), the electric field $\boldsymbol{E}$ and the current densities $\boldsymbol{J}_n$, $\boldsymbol{J}_p$ are assumed to be constant along each triangle edge. For instance, consider an edge e_{km} (in the direction of a unit vector $\boldsymbol{s}_{km}$) connecting two nodes k and m. To carry out the Poisson surface integral over the

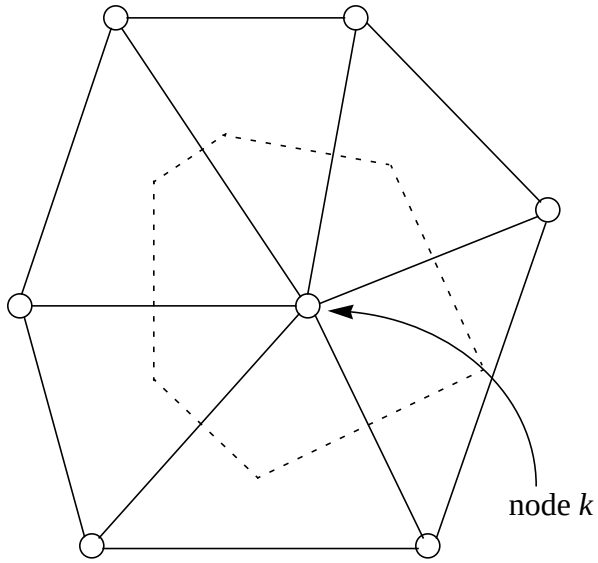

Figure 2.6 Control volume around node k, determined by the perpendicular bisectors (dashed).

perpendicular bisector corresponding to this edge, a finite-difference approximation is used for the dot product:

$$\boldsymbol{E} \cdot \boldsymbol{s}_{km} = \frac{\psi_m - \psi_k}{d_{km}}. \tag{2.32}$$

The situation is somewhat more complicated for the continuity equations. These could, in principle, be evaluated along each edge through use of (2.30) with simple first-order finite-difference approximations for ∇n and $\nabla\psi$. As pointed out by Scharfetter and Gummel [14], however, it turns out that such an approach results in numerical instability when the potential difference along an edge exceeds $2k_BT/q$. To remedy this situation, the Scharfetter-Gummel discretization scheme was proposed. We leave the detailed derivation to [14] [45], and merely state the result here:

$$\boldsymbol{J}_n \cdot \boldsymbol{s}_{km} = \frac{q\bar{\mu}_{km}\bar{\beta}_{km}}{d_{km}}\left[n_k B\left(\frac{\psi_k - \psi_m}{\bar{\beta}_{km}} \right) - n_m B\left(\frac{\psi_m - \psi_k}{\bar{\beta}_{km}} \right) \right], \tag{2.33}$$

where $B(x)$ is the Bernoulli function

$$B(x) = \frac{x}{e^x - 1}, \tag{2.34}$$

$\bar{\mu}_{km}$ is the effective average mobility along the edge, and

$$\bar{\beta}_{km} = \frac{\beta_k - \beta_m}{\ln(\beta_k/\beta_m)} \text{ with } \beta = \frac{D_n}{\mu_n}. \tag{2.35}$$

A result directly analogous to (2.33) applies to the hole continuity equation. By evaluating (2.32) and (2.33) for each side of the control volume polygon and summing the results, all the surface integrals (i.e., the left-hand sides) of (2.31) can be computed.

The area integrals on the right-hand side of (2.31) are evaluated by assuming that the integrand is approximately constant across the control volume. Since the control volume around node *k* has area A_k, the area integrals are computed as

$$\iint_{A_k} q\left(p - n + N_D^+ - N_A^- \right) dA = q\left(p_k - n_k + N_{Dk}^+ - N_{Ak}^- \right) A_k \tag{2.36}$$

$$\iint_{A_k} q\left(U + \frac{\partial n}{\partial t} \right) dA = q\left(U_k + \frac{\partial n_k}{\partial t} \right) A_k$$

$$\iint_{A_k} -q\left(U + \frac{\partial p}{\partial t} \right) dA = -q\left(U_k + \frac{\partial p_k}{\partial t} \right) A_k$$

From (2.32), (2.33), and (2.36) we see that the system of semiconductor equations at an internal device node *k* takes the form

$$\begin{aligned} g^{\psi}_{3k-2}(\boldsymbol{x}(t)) &= 0 \\ \frac{dx_{3k-1}}{dt} + g^{n}_{3k-1}(\boldsymbol{x}(t)) &= 0 \\ \frac{dx_{3k}}{dt} + g^{p}_{3k}(\boldsymbol{x}(t)) &= 0 \end{aligned} \tag{2.37}$$

where the state vector $\boldsymbol{x}(t)$ contains the electrostatic potential and carrier concentration variables[1]

$$\boldsymbol{x} = [\psi_1, n_1, p_1, \ldots, \psi_K, n_K, p_K] \, . \tag{2.38}$$

2.4.3 Boundary Conditions

The preceding section discussed the discretization and assembly procedures for nodes which are strictly within the interior of the device domain. Grid nodes at the semiconductor device boundary, however, must be handled differently depending on the type of boundary condition (BC) present at a given boundary node. In general, the boundary conditions in semiconductor device problems are either homogeneous Neumann, non-homogeneous Neumann, or Dirichlet, and can be different for any one of the three drift-diffusion equations. As an example, the surface recombination boundary condition used to model Schottky contacts places a Dirichlet BC on the Poisson equation, and a non-homogeneous Neumann BC on the continuity equations.

We begin by considering the contour of integration around a node on the device boundary (Figure 2.7). The line integrals can be split into two integrations over two disjoint sets — $\partial\Omega_{int}$, the internal portion of the contour, and $\partial\Omega_{ext}$, the external portion:

1. In general, the state vector may also contain additional variables if the semiconductor device is embedded in an external circuit network (Section 2.4.5). The state equations at the internal device nodes, however, will not be a function of these additional variables, and (2.37)-(2.38) remain valid.

$$\oint_{\partial\Omega_k} \varepsilon \boldsymbol{E} \cdot d\boldsymbol{S} = \int_{\partial\Omega_{k,\,int}} \varepsilon \boldsymbol{E} \cdot d\boldsymbol{S} + \int_{\partial\Omega_{k,\,ext}} \varepsilon \boldsymbol{E} \cdot d\boldsymbol{S}$$
$$\oint_{\partial\Omega_k} \boldsymbol{J}_n \cdot d\boldsymbol{S} = \int_{\partial\Omega_{k,\,int}} \boldsymbol{J}_n \cdot d\boldsymbol{S} + \int_{\partial\Omega_{k,\,ext}} \boldsymbol{J}_n \cdot d\boldsymbol{S} \qquad (2.39)$$
$$\oint_{\partial\Omega_k} \boldsymbol{J}_p \cdot d\boldsymbol{S} = \int_{\partial\Omega_{k,\,int}} \boldsymbol{J}_p \cdot d\boldsymbol{S} + \int_{\partial\Omega_{k,\,ext}} \boldsymbol{J}_p \cdot d\boldsymbol{S}$$

The integrals over $\partial\Omega_{k,\,int}$ (i.e., $\oint_{\partial\Omega_k} \varepsilon \boldsymbol{E} \cdot d\boldsymbol{S}$, $\oint_{\partial\Omega_k} \boldsymbol{J}_n \cdot d\boldsymbol{S}$, and $\oint_{\partial\Omega_k} \boldsymbol{J}_p \cdot d\boldsymbol{S}$) can still be evaluated in the same manner as before, via equations (2.32) and (2.33). On the boundary edges e_{km} and e_{kn}, however, the integration must be carried out in a different manner, subject to the boundary conditions present on that edge.

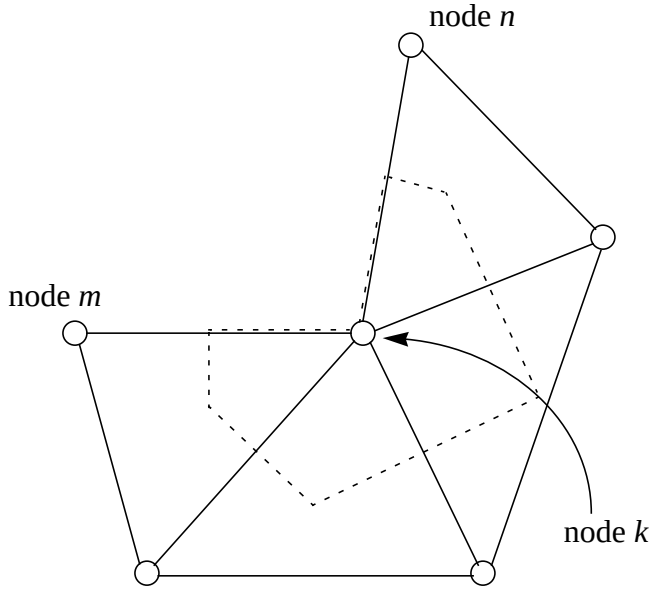

Figure 2.7 A boundary grid node.

For a homogeneous Neumann boundary condition, the current flux relation at a relevant edge is

$$\int_{\text{edge}} \boldsymbol{J} \cdot d\boldsymbol{S} = 0\,. \qquad (2.40)$$

Such boundary conditions exist at the edges of the device, where no current flux is allowed to pass. Implementation of homogeneous Neumann boundary conditions is

immediate, since the integration over the boundary edge is simply omitted. Non-homogeneous Neumann BCs, on the other hand, have the form

$$\frac{\boldsymbol{J}\cdot d\boldsymbol{S}}{|d\boldsymbol{S}|} = \phi(\psi_k, n_k, p_k) \tag{2.41}$$

when applied to a half-edge touching node k, and are handled by a discretized approximation at each half-edge. For instance, integration over half-edge e_{kn} yields

$$\int_{e_{kn}} \boldsymbol{J}\cdot d\boldsymbol{S} = \phi(\psi_k, n_k, p_k)\frac{1}{2}d_{kn} \tag{2.42}$$

In the case of Schottky contacts (the primary situation for using non-homogeneous Neumann BCs), the flux functions ϕ are given by

$$\phi^n = \sigma_n\cdot(n_k - n_{eq}), \quad \phi^p = \sigma_p\cdot(p_k - p_{eq}) \tag{2.43}$$

where σ_n and σ_p are the electron and hole surface recombination velocities, respectively. Equation (2.42) is applied for each boundary edge about a given boundary node, with the results summed to yield the total value of the integration about $\partial\Omega_{k,\,int}$. Thus, for the example of Figure 2.7, we would have

$$\begin{aligned}\int_{\partial\Omega_{k,\,ext}} \boldsymbol{J}_n\cdot d\boldsymbol{S} &= \phi^n(\psi_k, n_k, p_k)\frac{1}{2}d_{kn} + \phi^n(\psi_k, n_k, p_k)\frac{1}{2}d_{km}\\ \int_{\partial\Omega_{k,\,ext}} \boldsymbol{J}_p\cdot d\boldsymbol{S} &= \phi^p(\psi_k, n_k, p_k)\frac{1}{2}d_{kn} + \phi^p(\psi_k, n_k, p_k)\frac{1}{2}d_{km}\end{aligned}. \tag{2.44}$$

Dirichlet boundary conditions are present on the Poisson and continuity equations for ohmic contacts. Dirichlet BCs fix the given boundary node at some constant value, and are thus implemented through removal of the relevant differential equation and its replacement with $\psi_k = \psi_{\mathrm{BC},\,k}$ for a Dirichlet Poisson BC, or $n_k = n_{\mathrm{BC},\,k}$, $p_k = p_{\mathrm{BC},\,k}$ for appropriate continuity equation BCs. It is understood that in the above equations, $\psi_{\mathrm{BC},\,k}$, $n_{\mathrm{BC},\,k}$, and $p_{\mathrm{BC},\,k}$ are constants which are fixed for the duration of the simulation run.

In the case of the Dirichlet boundary conditions, equations (2.31) and (2.39) must still hold physically, and flux conservation must be satisfied. Although the boundary contour integrals are never evaluated explicitly in the Dirichlet case, their values may be computed once the relevant Dirichlet node values have been fixed. For instance, in the Poisson case, we have the relation

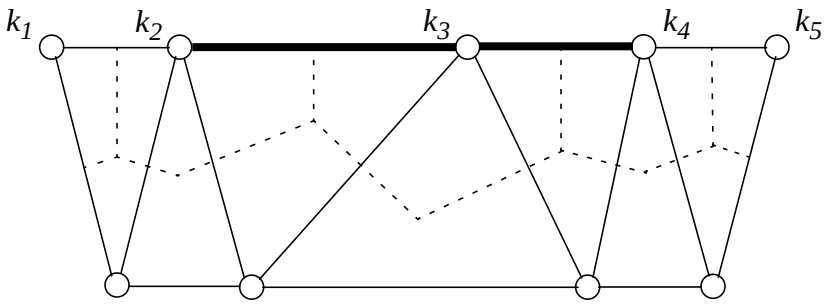

Figure 2.8 Grid near an electrode. The electrode segment is denoted by the thick bold line.

$$\int_{\partial\Omega_{k,\,ext}} \varepsilon \boldsymbol{E} \cdot d\boldsymbol{S} \;=\; q\Big(p_k - n_k + N_{Dk}^{+} - N_{Ak}^{-} \Big) A_k - \int_{\partial\Omega_{k,\,int}} \varepsilon \boldsymbol{E} \cdot d\boldsymbol{S}\,, \tag{2.45}$$

where $\int_{\partial\Omega_{k,\,int}} \varepsilon \boldsymbol{E} \cdot d\boldsymbol{S}$ is evaluated through repeated application of (2.32) for each internal polygon edge. This allows the convenient computation of electric field fluxes and free carrier currents at the electrode contacts, a topic which is the subject of the next section.

2.4.4 Terminal Current Evaluation

Terminal current values are perhaps the single most important set of quantities for many users of semiconductor device simulation tools. Ultimately, it is the device's terminal characteristics that determine how applicable it is to a given circuit-level design. While the electrostatic potential and free carrier distributions inside the device can offer important clues for optimizing device structure, these optimizations are typically valuable only insofar as they contribute to the ''bottom line'' — improved current-voltage output characteristics.

To illustrate how terminal currents are evaluated in the generalized box formulation, we make use of Figure 2.8. The total current flowing through the electrode includes the free carrier current components $\boldsymbol{J}_n$ and $\boldsymbol{J}_p$, along with the displacement current $\frac{\partial \boldsymbol{D}}{\partial t}$. The expression for current per unit width flowing through terminal l is

$$I_{Tl} = \int_{\partial\Omega_{Tl}} \left(\boldsymbol{J}_n + \boldsymbol{J}_p + \frac{\partial \boldsymbol{D}}{\partial t} \right) \cdot d\boldsymbol{S} \tag{2.46}$$
$$= \int_{\partial\Omega_{Tl}} (\boldsymbol{J}_n + \boldsymbol{J}_p) \cdot d\boldsymbol{S} + \frac{d}{dt} \int_{\partial\Omega_{Tl}} \varepsilon \boldsymbol{E} \cdot d\boldsymbol{S}$$

The integration above is carried out over the boundary edges comprising the electrode of interest. In our example of Figure 2.8, this boundary $\partial\Omega_{Tl}$ would consist of the two edges $e_{k_2 k_3}$ and $e_{k_3 k_4}$.

Application of equation (2.45) over each point of the electrode boundary domain already gives us the integral of the electrostatic displacement $\boldsymbol{D} = \varepsilon \boldsymbol{E}$ over the electrode. The current density integrals may be taken in an analogous manner —

$$\int_{\partial\Omega_{Tl}} \boldsymbol{J}_n \cdot d\boldsymbol{S} = \sum_{k \in \partial\Omega_{Tl}} \int_{\partial\Omega_{k,\,ext}} \boldsymbol{J}_n \cdot d\boldsymbol{S} \tag{2.47}$$
$$= \sum_{k \in \partial\Omega_{Tl}} \left[q\left(U_k + \frac{\partial n_k}{\partial t} \right) A_k - \int_{\partial\Omega_{k,\,int}} \boldsymbol{J}_n \cdot d\boldsymbol{S} \right]$$

where the notation $k \in \partial\Omega_{Tl}$ refers to nodes k that are on the electrode $\partial\Omega_{Tl}$, and the integral $\int_{\partial\Omega_{k,\,int}} \boldsymbol{J}_n \cdot d\boldsymbol{S}$ is taken by repeated application of (2.33). The hole current density integral is evaluated by a directly analogous expression. We point out that (2.47) holds in the non-homogeneous Neumann, as well as in the Dirichlet, case. The non-homogeneous term $\phi(\psi_k, n_k, p_k)$ doesn't appear in (2.47), but is used in setting up the appropriate discretization to satisfy the continuity equations on the electrode boundary. We also note that (2.44) offers an alternate method for evaluating the current through purely Schottky contacts once the simulation has converged.

Before closing out this section, we take the important step of symbolically expressing the total current per unit area at a given electrode l as

$$I_l(t) = g_l^{\text{cond}}(\boldsymbol{x}(t)) + \frac{d}{dt} g_l^{\text{disp}}(\boldsymbol{x}(t)) \tag{2.48}$$

The function $g_l^{\text{cond}}(\boldsymbol{x})$ represents the electron and hole currents, and is a scalar algebraic function of the state variable vector $\boldsymbol{x}$. Similarly, $g_l^{\text{disp}}(\boldsymbol{x})$ is an algebraic function representing the flux of electrostatic displacement through the electrode. It is clear that both functions are (loosely speaking) ‘‘structurally sparse’’ in the sense that they directly depend only on the values of the boundary node state variables, and not on the state variables associated with internal nodes.

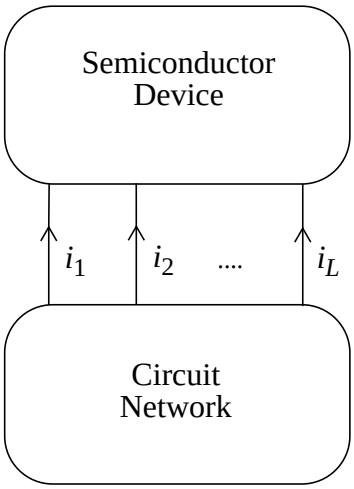

Figure 2.9 A semiconductor device interfaced to a circuit network.

2.4.5 Mixed Level Circuit and Device Simulation

In high-frequency analog applications, it is rarely sufficient to only analyze completely stand-alone intrinsic semiconductor devices. Typically, the circuit environment that the semiconductor device is embedded in will have a critical impact on device performance. The surrounding circuitry will, in general, include components to model parasitics, matching networks, biasing circuitry, and so forth. Consequently, it is extremely important for an analog device simulator to have a mixed circuit/device level simulation capability.

Figure 2.9 shows a block-diagram of an L-terminal semiconductor device connected to L terminals of a general circuit network. The circuit network is assumed to contain independent voltage and current sources, while the semiconductor device is represented solely by the drift-diffusion system (2.29)-(2.30) with no internal stimulus. To formulate a mixed level circuit/device system of equations, we employ the modified nodal analysis technique. Assuming that the semiconductor device has K nodes, there will be $3K$ nonlinear equations, along with a corresponding number of device state variables, representing the device. We assume that the circuit network portion can be described by N_{ckt} equations having the standard MNA circuit form

$$\boldsymbol{g}(\boldsymbol{x}_{ckt}(t)) + \frac{d}{dt}\boldsymbol{q}(\boldsymbol{x}_{ckt}(t)) + y(t) \otimes \boldsymbol{x}_{ckt}(t) - \boldsymbol{i}_{ckt}(t) = \boldsymbol{w}(t) \tag{2.49}$$

where $\boldsymbol{x}_{ckt}(t) \in \Re^{N_{ckt} \times 1}$ is the state vector for the circuit network, $\boldsymbol{w}(t) \in \Re^{N_{ckt} \times 1}$ is the vector of independent voltage/current source excitations, and $\boldsymbol{i}_{ckt}(t) \in \Re^{N_{ckt} \times 1}$ is a vector containing i_l in the *m*th position if device current i_l flows into circuit node *m*.

To join the circuit and device systems, the L state variables i_1, i_2, ..., i_L are introduced into the overall state vector. Likewise, the overall system is augmented with L additional coupling equations of the form

$$g_l^{\text{cond}}(\boldsymbol{x}_{dev}(t)) + \frac{d}{dt} g_l^{\text{disp}}(\boldsymbol{x}_{dev}(t)) - i_l(t) = 0 \tag{2.50}$$

The overall circuit-device system of equations has dimensionality $3K+N_{ckt}+L$.

2.5 Solving the State Equations By Transient Analysis

Transient analysis is by far the most commonly used method for simulating nonlinear circuits and semiconductor devices driven by large signal sources. The standard versions of tools such as PISCES and SPICE include only transient capability for analyzing systems under large signal time-varying input. In this section, we briefly review the standard time domain algorithms used in solving the systems of circuit/device equations formulated in the preceding sections. The overview is provided as a basis for comparing general-purpose transient analysis with special-purpose algorithms like harmonic balance, which are geared specifically toward solving the large signal sinusoidal steady-state problems arising in analog communication system design.

Transient analysis is based on approximating the d/dt operator in (2.28) by a finite-difference formula. Assuming that the state vector $\boldsymbol{x}(t)$ is known at time instants t_0, t_1, …, t_{k-1}, standard transient analysis approximates the derivative of the charge/flux vector at time t_k by formulas such as

$$\frac{d}{dt}\boldsymbol{q}(\boldsymbol{x}(t_k)) \approx \frac{\boldsymbol{q}(\boldsymbol{x}(t_k)) - \boldsymbol{q}(\boldsymbol{x}(t_{k-1}))}{t_k - t_{k-1}} \text{ (Backward Euler)} \tag{2.51}$$

or

$$\frac{d}{dt}\boldsymbol{q}\left(\boldsymbol{x}\left(t_k\right)\right) \approx \frac{\left(\boldsymbol{q}\left(\boldsymbol{x}\left(t_k\right)\right) - \boldsymbol{q}\left(\boldsymbol{x}\left(t_{k-1}\right)\right)\right)}{\frac{1}{2}\left(t_k - t_{k-1}\right)} - \frac{d}{dt}\boldsymbol{q}\left(\boldsymbol{x}\left(t_{k-1}\right)\right) \text{ (Trapezoidal)} \quad (2.52)$$

The above are two examples of first-order finite-difference schemes; there exist many other schemes of various orders [33][34], including Forward Euler, Gear's formulas, Adams-Bashforth and Adams-Moulton algorithms, and the TR-BDF2 algorithm [19]. For simplicity, we restrict ourselves to the Backward Euler formulation in this section. The state equations (2.28) are then discretized to have the form

$$\boldsymbol{g}\left(\boldsymbol{x}\left(t_k\right)\right) + \frac{\boldsymbol{q}\left(\boldsymbol{x}\left(t_k\right)\right) - \boldsymbol{q}\left(\boldsymbol{x}\left(t_{k-1}\right)\right)}{t_k - t_{k-1}} + \int_0^{t_k} y\left(t_k - \tau\right)\boldsymbol{x}\left(\tau\right)d\tau - \boldsymbol{w}\left(t_k\right) = \mathbf{0} \quad (2.53)$$

The convolution integral in the above equation can be approximated as

$$\int_0^{t_k} y\left(t_k - \tau\right)\boldsymbol{x}\left(\tau\right)d\tau = \int_0^{t_{k-1}} y\left(t_k - \tau\right)\boldsymbol{x}\left(\tau\right)d\tau + \int_{t_{k-1}}^{t_k} y\left(t_k - \tau\right)\boldsymbol{x}\left(\tau\right)d\tau \quad (2.54)$$

$$\approx A_k + B_k\boldsymbol{x}\left(t_k\right)$$

by straightforward integration, as is shown in [15]. With this formula, (2.53) becomes a system of nonlinear equations which is to be solved for the unknown vector

$$\boldsymbol{x}_k = \boldsymbol{x}\left(t_k\right). \quad (2.55)$$

The solution step is almost always carried out using the Newton-Raphson iterative process.

One fact that is immediately apparent from the above discussion is that the time step

$$\Delta t_k = t_k - t_{k-1} \quad (2.56)$$

must be selected small enough so that the finite-difference scheme in (2.53) is a good approximation to the actual derivative. This can be particularly problematic in the case where multi-tone signals are present at widely separated frequencies, as is common in many RF and microwave designs. For instance, consider the function

$$f(t) = \cos\left(2\pi \cdot 10^3 t\right) + \cos\left(2\pi \cdot 10^9 t\right), \quad (2.57)$$

which represents the superposition of a 1 GHz sinusoid and a 1 kHz sinusoid. Because of the presence of the fast sinusoid, the time step Δt_k should be less than a hundredth of a nanosecond to achieve decent accuracy. At the same time, the presence of the slow 1 kHz sinusoid means that the overall period is 1 millisecond. Thus, hundreds of millions of time steps would need to be taken, resulting in an extremely expensive simulation.

2.6 Summary

The nonlinear constitutive equations for both semiconductor devices and circuit networks share a common form. In analog applications, the steady state response of these nonlinear systems to large signal sinusoidal drive is of key interest. This chapter began with some background material on single- and multi-tone distortion effects, along with a discussion of several figures of merit requiring steady state analysis. Some common methodologies for formulating circuit and device equations were discussed, and a concise treatment of the spatial discretization algorithms used in PISCES-II was presented. The chapter ended with a brief discussion of conventional transient simulation algorithms, with some attention being given to their shortcomings in analog applications. Subsequent chapters will present frequency domain algorithms designed to overcome these shortcomings.

Chapter 3

Harmonic Balance Fundamentals

Harmonic balance (HB) is a nonlinear frequency domain analysis technique which is well-suited for handling multi-tone steady state distortion problems. For many high frequency (RF and microwave) applications, the solution of the state equations by standard transient methods can be prohibitively expensive. The difficulties faced by time domain methods stem from several causes:

- The applied voltage sources are typically sinusoids which may have very narrowly or very widely spaced frequencies. It is not uncommon for the highest frequency present in the response to be many orders of magnitude greater than the lowest frequency. This necessitates an integration over an enormous number of periods of the highest frequency sinusoid. To complicate matters further, if the input frequencies are not commensurate, then (in principle) a nearly infinite number of periods must be used to accurately resolve the distortion products.
- Designers are usually most interested in the system's steady state behavior. The presence of stiff linear bias and filtering circuitry around the semiconductor device can introduce extremely long time constants. This requires conventional transient methods to integrate over many periods of the lowest-frequency sinusoid to reach steady state, further exacerbating the problems brought about by very wide or very narrow frequency spacings.

- Many linear models at high frequencies are best represented in the frequency domain. Simulating such elements in the time domain via convolution often results in accuracy, causality, or stability problems.
- Many RF/microwave applications require very accurate resolution of low-level distortion products. Transient methods can have difficulties achieving the required levels of accuracy unless time points are spaced extremely close together, and all transients have decayed to negligible levels [25].

The harmonic balance technique addresses the above problems by solving the state equations in the frequency domain. It directly captures the large signal steady state response of nonlinear systems, and is almost completely insensitive to widely-varying time constants, tone spacings, and incommensurate frequencies. In addition, it exhibits excellent dynamic range for resolving low-level distortion products, and is ideal for handling linear circuit models characterized in the frequency domain. Highly nonlinear large signal problems do increase the computational resources that HB requires, and can greatly reduce its speed of convergence. However, we will demonstrate that harmonic balance is robust enough to routinely handle the levels of nonlinearity typically seen in the majority of RF/microwave applications.

Before proceeding towards a detailed description of the harmonic balance algorithm, we first take a moment to outline the basic idea. As we have seen before, the state equations describing semiconductor devices and circuit networks generally take the form

$$\boldsymbol{g}(\boldsymbol{x}(t)) + \frac{d}{dt}\boldsymbol{q}(\boldsymbol{x}(t)) + y(t) \otimes \boldsymbol{x}(t) - \boldsymbol{w}(t) = 0 . \tag{3.1}$$

In the HB technique, the state vector $\boldsymbol{x}(t)$ is assumed to be a Fourier series of sines and cosines, with unknown coefficients that the harmonic balance method will solve for. The state equations (3.1) are Fourier transformed into the frequency domain, with the transformation resulting in an algebraic set of nonlinear equations. During the solution process, the unknown Fourier coefficients are iteratively adjusted until the nonlinear system is satisfied to within some predetermined tolerance. Once finally obtained, the coefficients effectively characterize the system's steady state response for all time. We note that the choice of basis functions for $\boldsymbol{x}(t)$ effectively guarantees that the response we capture is indeed the steady state response, assuming that a steady state solution exists.

3.1 The Discrete Fourier Transform — Some Definitions and Notation

Since much of the work in subsequent sections will involve the Discrete Fourier Transform (DFT), we will take some time here to define the particular forms of the DFT that are used, and to establish some notational conventions. Because our formulation of the harmonic balance equations involves strictly real-valued time domain waveforms, a straightforward variant of the standard Discrete Fourier Transform, called the *single-sided* DFT, will typically be employed. Establishing a consistent notation and pointing out some subtleties in the transform's application will considerably simplify the presentation in subsequent sections.

3.1.1 The Double-Sided DFT

Consider the periodic waveform

$$x(t) = \sum_{h=-S+1}^{S} \tilde{X}_h \exp(jh\omega_0 t), \tag{3.2}$$

where $\tilde{X}_h = \tilde{X}_{-h}^*$, and $\tilde{X}_S$ is real to ensure that the resulting signal is strictly real-valued when sampled at the time points $t_s = \pi s/S\omega_0$. We assume an even number of Fourier coefficients ($\tilde{X}_{-S+1}, \ldots, \tilde{X}_{S-1}, \tilde{X}_S$) to make our formulation consistent with power-of-2 Fast Fourier Transform (FFT) algorithms. This choice of an even rather than odd DFT length forces the presence of the somewhat ''artificial'' component $\tilde{X}_S$. As mentioned above, this coefficient is forced to be real to ensure that the resulting time domain waveform is real, and thus cannot contain completely accurate information about the spectrum at that frequency bin. When transforming arbitrary waveforms from the time domain to the frequency domain, we must ensure that S is large enough so that only negligible energy due to aliasing lands in $\tilde{X}_S$.

The Fourier Transform Theorem guarantees that by sampling the periodic waveform (3.2) at the $2S$ time points $t_s = \pi s/S\omega_0$, $0 \le s \le 2S-1$, we can recover the coefficients $\tilde{X}_h$ from the waveform samples $x(t_s)$ (and vice-versa) through the analysis and synthesis formulas

$$\tilde{X}_h = \frac{1}{2S}\sum_{s=0}^{2S-1} x(t_s)\exp\left(-\frac{j2\pi sh}{2S}\right) \tag{3.3}$$

$$x(t_s) = \sum_{h=-S+1}^{S} \tilde{X}_h \exp\left(\frac{j2\pi sh}{2S}\right). \tag{3.4}$$

These relations can be cast into matrix form by defining the $2S \times 2S$ complex matrix

$$\tilde{\Gamma} = \frac{1}{2S}\begin{bmatrix} 1 & 1 & \cdots & 1 \\ W_{2S}^{1\cdot 0} & W_{2S}^{1\cdot 1} & \cdots & W_{2S}^{1\cdot(2S-1)} \\ | & | & \backslash & | \\ W_{2S}^{(2S-1)\cdot 0} & W_{2S}^{(2S-1)\cdot 1} & \cdots & W_{2S}^{(2S-1)\cdot(2S-1)} \end{bmatrix}, \tag{3.5}$$

where $W_{2S} = \exp\left(-\frac{2\pi j}{2S}\right)$. The Fourier Transform analysis and synthesis equations, (3.3) and (3.4), respectively, become

$$\begin{bmatrix} \tilde{X}_0 \\ \tilde{X}_1 \\ | \\ \tilde{X}_S \\ \tilde{X}_{-S+1} \\ | \\ \tilde{X}_{-1} \end{bmatrix} = \tilde{\Gamma}\begin{bmatrix} x_0 \\ x_1 \\ | \\ x_S \\ x_{S+1} \\ | \\ x_{2S-1} \end{bmatrix} \text{ and } \begin{bmatrix} x_0 \\ x_1 \\ | \\ x_S \\ x_{S+1} \\ | \\ x_{2S-1} \end{bmatrix} = \tilde{\Gamma}^{-1}\begin{bmatrix} \tilde{X}_0 \\ \tilde{X}_1 \\ | \\ \tilde{X}_S \\ \tilde{X}_{-S+1} \\ | \\ \tilde{X}_{-1} \end{bmatrix}. \tag{3.6}$$

3.1.2 The Single-Sided DFT

When dealing exclusively with real-valued time domain waveforms, it is redundant to store both the negative and positive sides of the spectrum, since these are simply complex conjugates of each other. An alternate representation of the periodic Fourier series is the so-called single-sided, or trigonometric, form involving only the positive-frequency coefficients:

$$x(t) = \Re e\left\{\sum_{h=0}^{S} X_h \exp(jh\omega_0 t)\right\} \tag{3.7}$$
$$= X_0^R + \sum_{h=1}^{S}\left(X_h^R \cos(h\omega_0 t) - X_h^I \sin(h\omega_0 t)\right)$$

where $X_h = 2\tilde{X}_h$ for $1 \le h \le S-1$, $X_0 = \tilde{X}_0$, $X_S = \tilde{X}_S$, and X_h^R, X_h^I are the real and imaginary parts, respectively, of X_h. These single-sided coefficients are consistent with conventional phasors used in AC analysis[1].

In the single-sided formulation, the forward (i.e., ‘‘analysis’’) part of the DFT simply becomes

$$X_h = \frac{2-\delta_h-\delta_{h-S}}{2S}\sum_{s=0}^{2S-1} x(t_s)\exp\left(-\frac{j2\pi sh}{2S}\right),\ 0 \le h \le S. \tag{3.8}$$

This is readily expressed in matrix form through use of an $(S+1)\times 2S$ complex transform matrix which maps the $2S$ real samples $x_0, x_1, \ldots, x_{2S-1}$ to the S+1 complex Fourier coefficients $X_0, X_1, \ldots, X_S$:

$$\begin{bmatrix} X_0 \\ X_1 \\ | \\ X_S \end{bmatrix} = \frac{1}{S}\begin{bmatrix} \frac{1}{2} & \frac{1}{2} & \cdots & \frac{1}{2} \\ W_{2S}^{1\cdot 1} & W_{2S}^{1\cdot 2} & \cdots & W_{2S}^{1\cdot(2S-1)} \\ | & | & \backslash & | \\ \frac{1}{2}W_{2S}^{S\cdot 1} & \frac{1}{2}W_{2S}^{S\cdot 2} & \cdots & \frac{1}{2}W_{2S}^{S\cdot(2S-1)} \end{bmatrix}\begin{bmatrix} x_0 \\ x_1 \\ | \\ x_{2S-1} \end{bmatrix}. \tag{3.9}$$

The reverse (i.e., synthesis) transform operator, however, cannot be represented as a single complex-valued matrix which maps the complex coefficients $X_0, X_1, \ldots, X_S$ to real samples $x_0, x_1, \ldots, x_{2S-1}$. This problem occurs because the time samples are no longer an analytic function of the Fourier coefficients:

$$x(t_s) = X_0 + \frac{1}{2}\sum_{h=1}^{S-1}\left[X_h \exp\left(\frac{j2\pi sh}{2S}\right) + X_h^* \exp\left(-\frac{j2\pi sh}{2S}\right)\right] + X_S \exp(-j\pi s)\ . \tag{3.10}$$

The presence of the conjugated terms in (3.10) leads to the aforementioned loss of analyticity, and has important implications for solving the harmonic balance system of

1. Except for the purely real ‘‘non-physical’’ phasor X_S.

equations. Briefly, it implies that the use of single-sided transforms and single-sided spectral representations leads to a system of nonlinear HB equations which is not analytic. Such systems must effectively be solved in the real number field, by separating the real and complex parts. This issue will be addressed more fully in Section 3.5.

Given the non-analytic nature of the single-sided transform operators, we abandon the complex field and define our vector of frequency domain coefficients as the purely real array $\boldsymbol{X} = \left[X_0^R, X_1^R, X_1^I, \ldots, X_{S-1}^R, X_{S-1}^I, X_S^R\right]^T$. The Fourier Transform relationships of equations (3.7) and (3.8) become, in matrix form,

$$\begin{bmatrix} X_0^R \\ X_1^R \\ X_1^I \\ | \\ X_{S-1}^R \\ X_{S-1}^I \\ X_S^R \end{bmatrix} = \Gamma \begin{bmatrix} x_0 \\ x_1 \\ x_2 \\ | \\ x_{2S-3} \\ x_{2S-2} \\ x_{2S-1} \end{bmatrix} \text{ and } \begin{bmatrix} x_0 \\ x_1 \\ x_2 \\ | \\ x_{2S-3} \\ x_{2S-2} \\ x_{2S-1} \end{bmatrix} = \Gamma^{-1} \begin{bmatrix} X_0^R \\ X_1^R \\ X_1^I \\ | \\ X_{S-1}^R \\ X_{S-1}^I \\ X_S^R \end{bmatrix}. \tag{3.11}$$

Here, Γ and Γ^{-1} are $2S \times 2S$ real matrices containing the sine and cosine terms of the trigonometric Discrete Fourier Transform:

$$\Gamma^{-1} = \begin{bmatrix} C_{00} & C_{01} & S_{01} & C_{02} & S_{02} & \cdots & C_{0,S} \\ C_{10} & C_{11} & S_{11} & C_{12} & S_{12} & \cdots & C_{1,S} \\ C_{20} & C_{21} & S_{21} & C_{22} & S_{22} & \cdots & C_{2,S} \\ | & | & | & | & | & \backslash & | \\ C_{2S-1,0} & C_{2S-1,1} & S_{2S-1,1} & C_{2S-1,2} & S_{2S-1,2} & \cdots & C_{2S-1,S} \end{bmatrix}, \tag{3.12}$$

$C_{rs} = \cos\left(\frac{2\pi rs}{2S}\right)$, $S_{rs} = -\sin\left(\frac{2\pi rs}{2S}\right)$. This is the transform relation that we will use in all subsequent work.

3.2 The Quasiperiodic Steady State

3.2.1 Representing Quasiperiodic Signals

A *quasiperiodic* waveform is defined to be one which consists of a linear combination of a finite number of sinusoids. Consider the set of M linearly independent (i.e., incommensurate[1]) fundamental frequencies $\Omega_1, \Omega_2, \ldots, \Omega_M$. Then $x(t)$ is a quasiperiodic waveform with M fundamentals if it can be expressed as

$$\begin{aligned} x(t) &= X_0 + \sum_{h=1}^{H} \left(X_h^R \cos(\omega_h t) - X_h^I \sin(\omega_h t) \right) \\ &= \Re e \left\{ \sum_{h=0}^{H} X_h \exp(j\omega_h t) \right\} \end{aligned} \tag{3.13}$$

where

$$\omega_h \in \{ \omega_{k_1 k_2 \ldots k_M} \,|\, \omega_{k_1 k_2 \ldots k_M} = k_1\Omega_1 + k_2\Omega_2 + \ldots + k_M\Omega_M \text{ for integer } k_i \} \tag{3.14}$$

Each frequency in the M-quasiperiodic waveform $x(t)$ is an integral combination of the fundamentals $\Omega_1, \Omega_2, \ldots, \Omega_M$. To each frequency component in the set (3.14), we assign an *order* equal to the absolute sum of its fundamental indices. That is, the component $\omega = k_1\Omega_1 + k_2\Omega_2 + \ldots + k_M\Omega_M$ has an order of $|k_1| + |k_2| + \ldots + |k_M|$ corresponding to it. Intuitively, for a system with finite energy, the spectral components at high enough orders should have vanishingly low amplitudes.

If a quasiperiodic signal $x(t)$ is passed through a resistive nonlinearity $g(x)$, the resulting waveform $g(x(t))$ will also be quasiperiodic. This becomes apparent if the nonlinearity is expanded in a Taylor series around $x = X_0$, and the multinomial theorem [23] is applied:

1. Two frequencies are said to be incommensurate if their ratio is not a rational number.

$$g(x(t)) = \Re e\left\{\sum_{k=0}^{\infty}\frac{g^{(k)}(X_0)}{k!}\left(\sum_{h=1}^{H}X_h\exp(j\omega_h t)\right)^k\right\} \tag{3.15}$$

$$= \Re e\left\{\sum_{k=0}^{\infty}\frac{g^{(k)}(X_0)}{k!}\sum_{h_1+\ldots+h_H=k}\frac{k!}{h_1!\ldots h_H!}X_1^{h_1}\ldots X_H^{h_H}\exp(j(h_1\omega_1+\ldots h_H\omega_H))\right\}$$

Since the frequencies present in the response waveform are integer combinations of those present in the *M*-quasiperiodic stimulus, we see that the response is also *M*-quasiperiodic.

3.2.2 Harmonic Truncation

In principle, there are an infinite number of frequencies present in the set (3.14). In practice, only a finite number of these spectral components contain significant energy. To represent a quasiperiodic waveform for simulation on a computer, the frequencies present in (3.14) must be truncated to some finite set, thus neglecting the energy present in the excluded components. For accurate results, the truncation must be chosen such that the excluded energy is negligible.

Two common methods for harmonic truncation are the so-called box and diamond truncations. In the box technique, a truncation of order *P* results in a set of frequencies where the index of each fundamental in a given frequency is less than *P*:

$$B_P = \{\omega|\omega = k_1\Omega_1 + k_2\Omega_2 + \ldots + k_M\Omega_M, |k_1| \le P, |k_2| \le P, \ldots, |k_M| \le P\}\ . \tag{3.16}$$

Since real-valued waveforms can be represented by single-sided spectra, it is redundant to include both the positive- and negative- valued frequencies in the set above. To ensure that such image frequencies don't occur, it is necessary to add to (3.16) the constraint that the first non-zero coefficient k_m be positive:

$$k_1 \ge 0\,,\ k_m \ge 0 \quad \text{if} \quad k_1 = k_2 = \ldots = k_{m-1} = 0 \tag{3.17}$$

Figure 3.1 illustrates the box truncation in the $M = 2$ case, for both the double- and single-sided forms. The single-sided form generates a total of $\frac{1}{2}\left((2P+1)^M + 1\right)$ frequencies, which reduces to $2P^2 + 2P + 1$ for two-tone problems.

In the diamond truncation, the set of included frequencies is chosen such that the absolute sum of the indices is less than or equal to the truncation order:

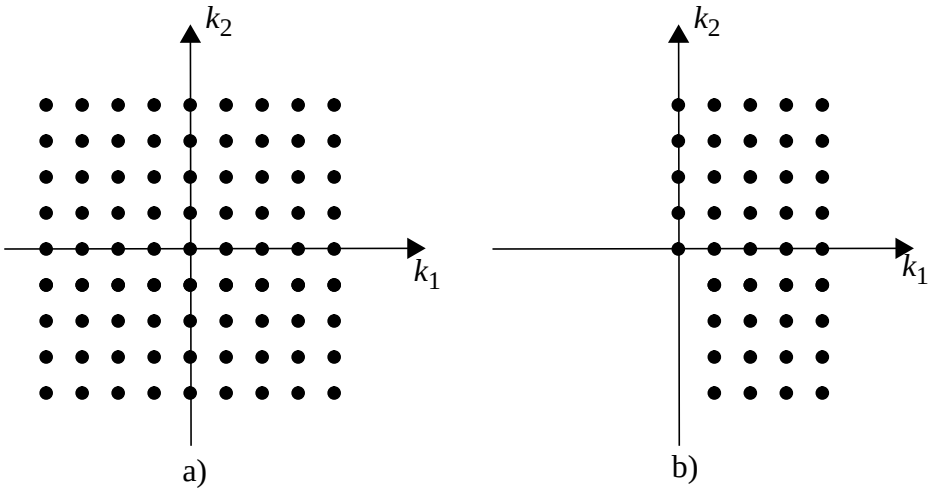

Figure 3.1 The two-tone box truncation of order $P = 4$ in the (a) double-sided formulation and the (b) single-sided formulation.

$$D_P = \{\omega | \omega = k_1\Omega_1 + k_2\Omega_2 + \ldots + k_M\Omega_M, |k_1| + |k_2| + \ldots + |k_M| \leq P\} . \quad (3.18)$$

To avoid image frequencies and employ the single-sideband waveform representation, the additional constraint

$$k_1 + k_2 > 0 \text{ or } (k_1 \geq 0 \text{ and } k_2 = -k_1) \quad (3.19)$$

must be invoked.[1] This latter constraint is perhaps somewhat less intuitive than its analog for box truncation; a detailed explanation of the rationale for this constraint is presented in Section 3.3.2. Figure 3.2 illustrates the diamond truncation graphically in the case of two-fundamentals, and shows why the diamond truncation yields roughly a factor of 2^{M-1} savings in the number of harmonics over its box counterpart. The diamond truncation is usually more efficient than box truncation, since the harmonics it neglects have a higher order than the largest harmonic of any fundamental, and should typically contain only negligible energy when the truncation order is chosen properly.

1. The constraint is given here for the case M=2.

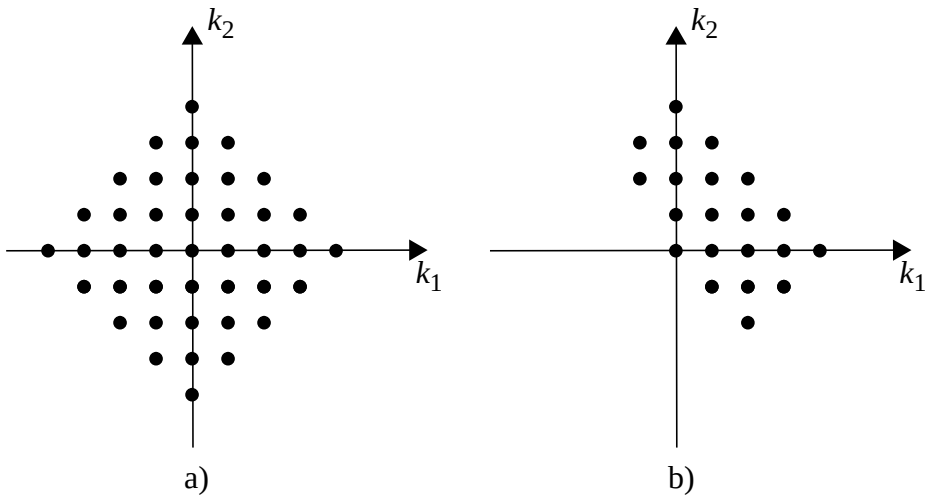

Figure 3.2 The two-tone diamond truncation of order $P = 4$ in the (a) double-sided formulation and the (b) single-sided formulation using constraint (3.19).

A somewhat more flexible truncation scheme than either the box or the diamond is used by HP's commercial simulators [13]. This variant can be viewed as a hybrid of the two standard truncations outlined above, and will be referred to as the ''modified diamond truncation.'' In this scheme, each fundamental m is assigned a separate order P_m. A harmonic of fundamental m is included in the truncated set if and only if its order is less than P_m. Mixing products (i.e., frequencies that are not harmonically related to a single fundamental) are included only if their order is less than an overall diamond truncation order P_{max}. The resulting set of frequencies may be formally specified by defining the two sets

$$T_1 = \{\omega | \omega = k_m \Omega_m, 1 \le m \le M, |k_m| \le P_m\}$$
$$T_2 = \{\omega | \omega = k_1\Omega_1 + \ldots + k_M\Omega_M, |k_1| + \ldots + |k_M| \le P_{max}, |k_1| \le P_1, \ldots, |k_M| \le P_M\} \quad (3.20)$$

and then taking the union of the two to obtain the modified diamond truncation

$$MD = T_1 \bigcup T_2 \tag{3.21}$$

In direct analogy to the diamond and box truncations, the modified diamond scheme can be purged of image frequencies by application of the additional constraint (3.17).

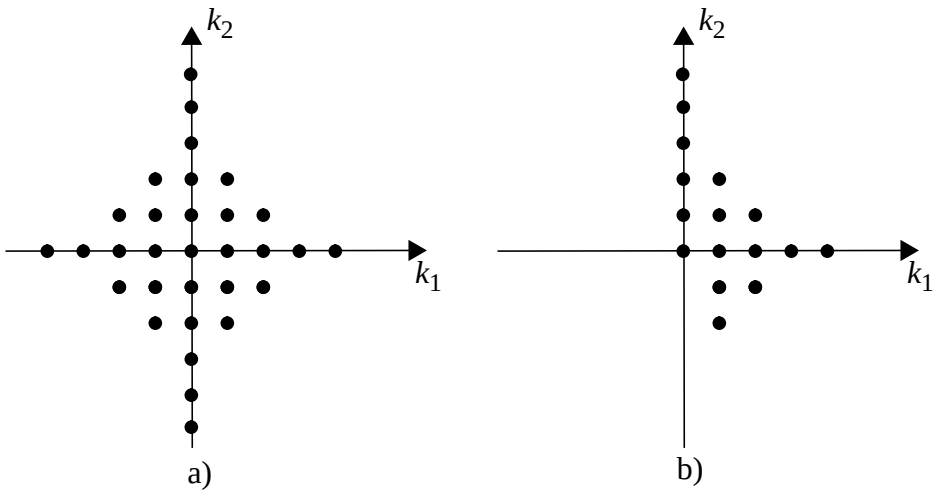

Figure 3.3 The two-tone modified diamond truncation of orders P_1=4, P_2=5, and P_{max}=3 and in the (a) double-sided formulation and the (b) single-sided formulation.

Graphical illustrations for both the double-sided truncation and the single-sided (image-free) truncation are provided in Figure 3.3.

Thus far, we've focused on fundamental frequencies that are purely incommensurate. In practice, it is common to have fundamentals which are harmonically related, but which nevertheless have a prohibitively large common period. For instance, if one fundamental is at 30 kHz and the other is at 1 GHz, then the two frequencies are commensurate because they are both harmonics of 10 kHz. In principle, then, the analysis can be carried out as a one-tone (M = 1) simulation with a fundamental frequency of 10 kHz. However, this would require a minimum of 10^5 harmonics (and likely several times more), because that many periods of 1 GHz fit into a single period of 10 kHz. Clearly, such large transform sizes are inefficient, and border on the impractical. The problem is easily avoided by treating the simulation as a two-tone analysis (i.e., M = 2), with fundamentals at 30 kHz

and 1 GHz. In doing so, one must be careful to ensure that the truncated frequencies do not overlap. For example, given a simulation with fundamentals of 10 Hz and 50 Hz, it would not permissible to use a truncation scheme of order 3. If such a scheme was used, multiple frequencies would land on the same bin — we would have $0 \cdot 50 + 3 \cdot 10 = 30$ Hz as a (0, 3) entry, along with $1 \cdot 50 - 2 \cdot 10 = 30$ Hz as a (1, -2) entry. To avoid such colliding harmonics in the case above, the problem should be formulated as a single-tone analysis at a fundamental frequency of 10 Hz.

3.3 Quasiperiodic Transforms

Given a periodic waveform $x(t)$, we can use the standard Discrete Fourier Transform to obtain a frequency-domain (Fourier series) representation of $g(x(t))$ for "well-behaved" algebraic functions *g*. Assuming that the waveform is periodic with period *T*, and that we can evaluate both *g* and *x* over their respective domains, there is the well-known Discrete Fourier Transform relationship for obtaining the harmonic coefficients:

$$G_h^R = \frac{2-\delta_h}{2H+2}\sum_{s=0}^{2H+1} g(x(t_s))\cos\left(\frac{2\pi hs}{2H+2}\right) \quad , 0 \le h \le H \tag{3.22}$$

$$G_h^I = -\frac{2-\delta_h}{2H+2}\sum_{s=0}^{2H+1} g(x(t_s))\sin\left(\frac{2\pi hs}{2H+2}\right)$$

where $t_s = \frac{sT}{2H+2}$. Assuming that *H*, the total number of non-DC harmonics, is large enough to adequately represent $g(x(t))$ with minimal aliasing, we have the relationship

$$g(x(t)) \approx G_0 + \sum_{h=1}^{H}\left(G_h^R\cos\left(\frac{2\pi h}{T}t\right) - G_h^I\sin\left(\frac{2\pi h}{T}t\right)\right). \tag{3.23}$$

For quasiperiodic waveforms, however, the standard Discrete Fourier Transform cannot be directly applied. Consider, for example, the quasiperiodic waveform $x(t) = \cos(2t) + \cos(2\pi t)$. Although it is the sum of two periodic signals, it is not periodic, because it consists of two separate waveforms with incommensurate periods of π and 1. Since π is irrational, it is clear that the there does not exist a common period, and that the DFT is not directly applicable to finding the Fourier representation of $g(x(t))$.

One approach to solving the problem would be to operate ‘‘symbolically’’ on the waveform in the manner of equation (3.15). Unfortunately, this requires the availability of

a potentially arbitrary number of derivatives of g, and is thus not practical for semiconductor device simulation. We note that such approaches have indeed been tried in the area of circuit simulation, where they are somewhat more practical. However, the need for such symbolic approaches has been effectively obsoleted by quasiperiodic transform algorithms which are presented below.

3.3.1 The Frequency-Remapped DFT/FFT

In examining equation (3.15), a key observation emerges: the amplitude of the sinusoidal component $\exp(j(h_1\omega_1 + \ldots h_H\omega_H)t)$ is independent of the frequencies $\omega_1, \ldots, \omega_H$, and thus independent of the actual values of the fundamentals $\Omega_1, \ldots, \Omega_M$. To illustrate this phenomenon in a less abstract fashion, we introduce the following example. Consider a two-tone signal $x(t) = A\cos(\Omega_A t) + B\cos(\Omega_B t)$, and the simple quadratic nonlinearity $g(x) = x^2$. Then, after some straightforward algebraic manipulation, we have

$$g(x(t)) = \frac{A^2 + B^2}{2} + \frac{A^2}{2}\cos(2\Omega_A t) + \frac{B^2}{2}\cos(2\Omega_B t) \quad . \tag{3.24}$$

$$+ AB\cos((\Omega_A - \Omega_B)t) + AB\cos((\Omega_A + \Omega_B)t)$$

The spectral coefficients (i.e., the coefficients of the cosines) are dependent only on the amplitudes A and B, and not on the fundamental frequencies Ω_A and Ω_B.

Since the exact numerical value of the fundamental frequencies is unimportant,[1] they can be remapped to multiples of a single fundamental for purposes of computing the Fourier coefficients. This is the key idea of the frequency-remapping technique. Although the new set of response frequencies will be different than the original set, the Fourier coefficients of each spectral component will be the same. Consequently, it is possible to use the harmonically related set of artificial frequencies to find the Fourier coefficients, and then switch back to the original frequency set once the coefficients have been obtained. This idea can work only if there exists a one-to-one relationship between the original and the remapped frequency set, and the remapping scheme must be chosen such that this is the case.

1. The exact values are unimportant provided that the truncation is such that collisions between the various frequencies don't occur; see the last paragraph of Section 3.2.2.

In remapping the original frequency set to multiples of a single fundamental, we are free to arbitrarily pick the new fundamental frequency. For convenience, it can be chosen to be 1, allowing all remapped frequency values to be integers. Rigorously, then, our problem is as follows: given a set of frequencies ω_h, $0 \le h \le H$, and a truncated frequency set such as (3.16), (3.18), or (3.21), we need to generate M artificial integer frequencies $\hat{\Omega}_1, \hat{\Omega}_2, \ldots, \hat{\Omega}_M$ with the following properties:

- Given that $\omega_h = k_1\Omega_1 + k_2\Omega_2 + \ldots + k_M\Omega_M$, the corresponding remapped frequency will be $\mu(h) = k_1\hat{\Omega}_1 + k_2\hat{\Omega}_2 + \ldots + k_M\hat{\Omega}_M$. μ is an integer-to-integer function which we will call the remapping function.
- μ must have the property that $\mu(h_1) \neq \mu(h_2)$ whenever $h_1 \neq h_2$. Put another way, no two remapped frequencies can correspond to the same ω_h.

With the proper mapping set up, it becomes possible to obtain the Fourier coefficients of $g(x(t))$ for quasiperiodic waveforms $x(t)$. Assuming that

$$x(t) = X_0 + \sum_{h=1}^{H} \left(X_h^R \cos(\omega_h t) - X_h^I \sin(\omega_h t) \right), \tag{3.25}$$

the artificial waveform $\hat{x}(t)$ is defined to have the same Fourier coefficients, but at the remapped frequencies:

$$\hat{x}(t) = X_0 + \sum_{h=1}^{H} \left(X_h^R \cos(\mu(h)\, t) - X_h^I \sin(\mu(h)\, t) \right). \tag{3.26}$$

Because $\hat{x}(t)$ is now periodic with period 2π, (3.22) can be applied to obtain the Fourier coefficients of $g(\hat{x}(t))$, assuming that H is large enough to make aliasing insignificant:

$$g(\hat{x}(t)) \approx G_0 + \sum_{h=1}^{H} \left(G_h^R \cos(\mu(h)\, t) - G_h^I \sin(\mu(h)\, t) \right). \tag{3.27}$$

By the arguments at the beginning of this section, we conclude that

$$g(x(t)) \approx G_0 + \sum_{h=1}^{H} \left(G_h^R \cos(\omega_h t) - G_h^I \sin(\omega_h t) \right), \tag{3.28}$$

and consequently that the G_h are indeed the Fourier coefficients of $g(x(t))$.

3.3.2 Remapping Functions

Having established the basic theory underlying the multi-tone frequency remap technique, we now present actual remapping functions μ to handle the box, diamond, and modified diamond truncations. For the two-tone diamond and box schemes, there exist remapping functions which are optimal in the sense that the remapped spectrum is ‘‘densely packed’’ — i.e., each remapped spectral line corresponds to a frequency in the truncation. For other truncations, the remapped spectrum is not densely packed in general, and the size of the DFT must be larger than the number of frequencies present in the truncation.[1]

We first consider the two-tone box truncation (3.16), which has the most straightforward remapping function. Letting $\hat{\Omega}_1$ and $\hat{\Omega}_2$ denote the integer-valued remapped fundamentals, a densely packed remapping function may be obtained by setting

$$\begin{aligned} \hat{\Omega}_1 &= 2P + 1 \\ \hat{\Omega}_2 &= 1 \end{aligned} \tag{3.29}$$

where P is the order of the truncation. Thus, a given frequency $\omega_h \in B_P$ having indices k_1 and k_2 such that

$$\omega_h = k_1\Omega_1 + k_2\Omega_2 \tag{3.30}$$

is remapped into the integer valued frequency

$$\begin{aligned} \mu_{B_P}(h) &= k_1\hat{\Omega}_1 + k_2\hat{\Omega}_2 \\ &= k_1(2P + 1) + k_2 \end{aligned} \tag{3.31}$$

If in addition the constraint (3.17) is applied to k_1 and k_2, $\mu(h)$ becomes strictly non-negative, and a single-sideband formulation is achieved.

The two-tone diamond truncation (3.18) may be densely packed through a remapping scheme presented by Hente and Jansen [26]. For a truncation of order *P*, the suitable remapping is achieved by setting

1. In addition, it is necessary to round the transform size up to nearest power of 2 to use efficient power-of-2 FFT algorithms.

$$\begin{aligned} \hat{\Omega}_1 &= P + 1 \\ \hat{\Omega}_2 &= P \end{aligned} \quad . \tag{3.32}$$

A given frequency $\omega_h \in D_P$ having indices k_1 and k_2 such that

$$\omega_h = k_1\Omega_1 + k_2\Omega_2 \tag{3.33}$$

will be assigned by μ to the integer bin

$$\begin{aligned} \mu_{D_P}(h) &= k_1\hat{\Omega}_1 + k_2\hat{\Omega}_2 \quad . \\ &= (k_1 + k_2)\,P + k_1 \end{aligned} \tag{3.34}$$

To constrain these remapped values to be non-negative, we proceed as follows. Since the diamond truncation of order P mandates that $|k_1| + |k_2| \le P$, k_1 must always satisfy the inequality $-P \le k_1 \le P$. Thus, for $k_1 + k_2 > 0$, μ_{D_P} will always be positive. For $k_1 + k_2 = 0$, μ_{D_P} will be positive if and only if $k_1 > 0$. For the case where $k_1 + k_2 < 0$, μ_{D_P} will always be negative. Consequently, invoking the constraint (3.19) ensures that only a single sideband is generated, and that it falls to strictly positive remapped frequencies.

The remapping strategies for the diamond and box truncations can be used as a basis for other truncation schemes, such as the modified diamond method. The remapping strategies may also be readily extended to more than two fundamental tones through recursive application of the two-tone scheme. It should be noted, however, that the remappings for the aforementioned truncations are not densely packed, and so require more remapped frequencies than are present in the truncation.

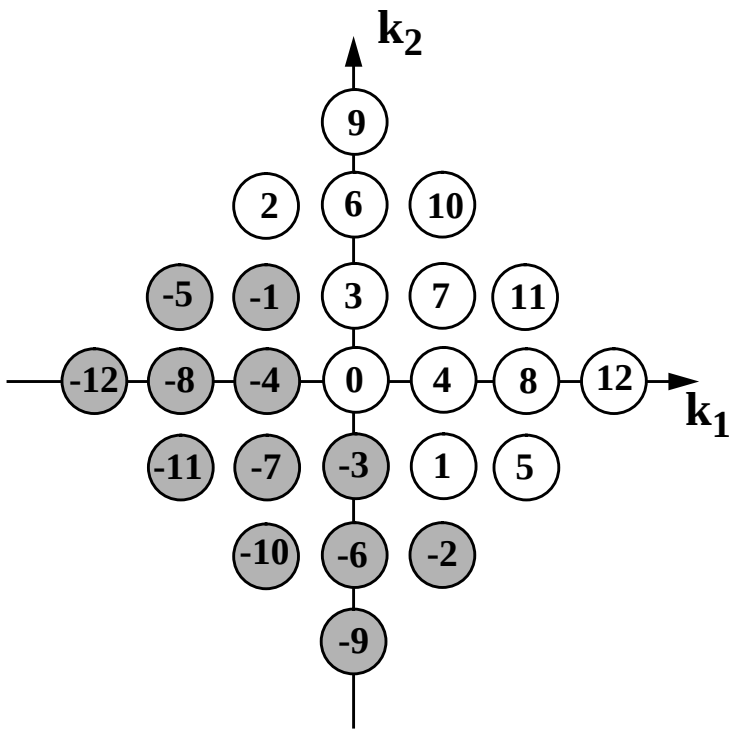

Figure 3.4 Remapping for diamond truncation of order P = 4. The shaded bins represent complex-conjugate ‘‘image’’ slots that are absent from the single-sided formulation.

3.3.3 A Remapping Example

To provide a concrete frequency remapping example, let’s consider a diamond truncation of order $P = 3$ for a problem with fundamental frequencies $f_1 = 100$ Hz and $f_2 = 1$ Hz. Following (3.32), the remapped frequencies are $\hat{\Omega}_1 = 4$ and $\hat{\Omega}_2 = 3$. A frequency mixing term falling at the physical frequency

$$k_1 f_1 + k_2 f_2 \tag{3.35}$$

is thus remapped to an integer frequency bin:

$$k_1 f_1 + k_2 f_2 \rightarrow k_1 \hat{\Omega}_1 + k_1 \hat{\Omega}_1 = 4k_1 + 3k_2 \tag{3.36}$$

The diamond pattern showing the remapped integer bin values corresponding to each (k_1,k_2) mixing term is shown in Figure 3.4.

$\mu(h)$	k_1	k_2	$\lvert f_h \rvert$ (Hz)
0	0	0	0
1	1	-1	99
2	-1	2	98
3	0	1	1
4	1	0	100
5	2	-1	199
6	0	2	2
7	1	1	102
8	2	0	200
9	0	3	3
10	1	2	102
11	2	1	201
12	3	0	300

Table 3.1 Correspondence between remapped and physical frequencies.

Table 3.1 above shows the correspondence between the physical and remapped frequencies. For purposes of evaluating the semiconductor device nonlinearities, each physical waveform

$$x(t) = X_0 + \sum_{h=1}^{H} \left(X_h^R \cos(\omega_h t) - X_h^I \sin(\omega_h t) \right) \tag{3.37}$$

is represented by a remapped waveform

$$\hat{x}(t) = X_0 + \sum_{h=1}^{H} \left(X_h^R \cos(\mu(h)\, t) - X_h^I \sin(\mu(h)\, t) \right) \tag{3.38}$$

which has a far more manageable spectrum. In this example, both the physical and the remapped waveforms are periodic. However, the number of samples needed by DFT/FFT transforms to explicitly compute the spectral representation of $g(x(t))$ is much larger than that needed to compute the transform of $g(\hat{x}(t))$. Figure 3.5 illustrates the situation for our example. In cases where the two fundamentals are incommensurate, the DFT/FFT approach cannot be used at all without resorting to a remapping[1] or a multi-tone

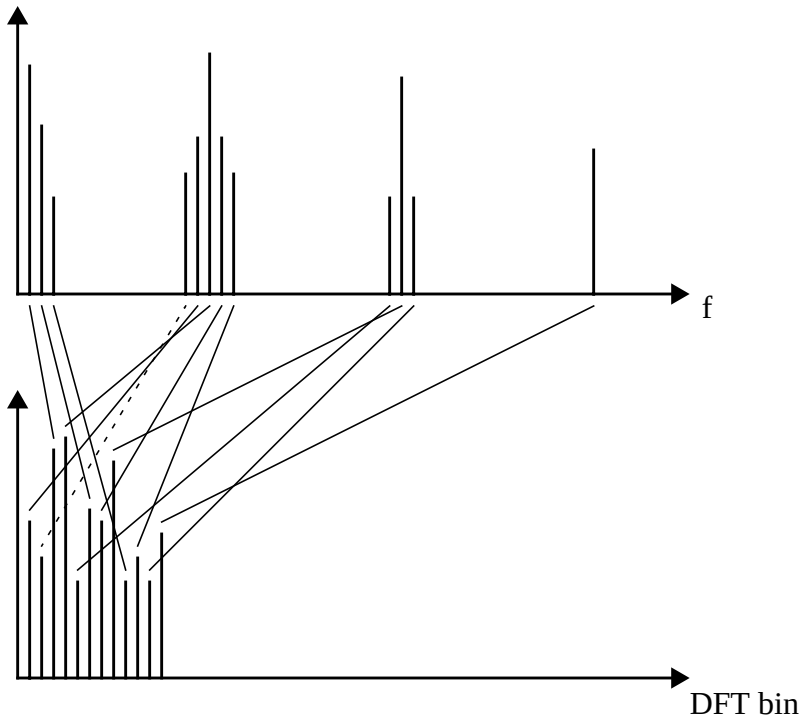

Figure 3.5 The physical and remapped spectral representations of *x(t)* (not to scale). Note how the effective transform size is reduced. The dashed line above corresponds to the (-1,2) mixing product which must be conjugated because its bin corresponds to the negative physical frequency -98 Hz.

transform. Although not used in this work, the latter approach is outlined in the next section below for the sake of completeness.

3.3.4 The Multi-Dimensional DFT/FFT

An alternate approach to multi-tone quasiperiodic transforms is the use of a multi-dimensional Discrete Fourier Transform [31]. This transform has been widely used in the

1. In practice, of course, incommensurate frequencies can be approximated arbitrarily closely by commensurate frequencies. However, the common period may become prohibitively long.

harmonic balance literature [32][30], and does not require the frequency remappings of Section 3.3.1. Before proceeding to describe its application to harmonic balance, we briefly review the basics of the *M*-dimensional DFT.

Suppose we have a scalar function $y(t_1, \ldots, t_M)$ of M time variables, which is periodic with period $T_m = 2\pi/\Omega_m$ in each dimension 1, 2, ..., *M*. In direct analogy to the 1-dimensional case, each of the *M* time dimensions of *y* may be sampled over its period to obtain an *M*-dimensional hypercube of samples

$$y_{n_1 \ldots n_M} = y\left(\frac{n_1 T_1}{N_1}, \ldots, \frac{n_M T_M}{N_M}\right), 0 \le n_m \le N_m \text{ for } 1 \le m \le M. \tag{3.39}$$

The *M*-dimensional Discrete Fourier Transform Theorem establishes the existence of the forward and backward DFT relations

$$Y_{k_1 \ldots k_M} = \frac{1}{N_{tot}} \sum_{n_1 = 0}^{N_1} \cdots \sum_{n_M = 0}^{N_M} y_{n_1 \ldots n_M} \exp\left[-2\pi j\left(\frac{k_1 n_1}{N_1} + \ldots \frac{k_M n_M}{N_M}\right)\right] \tag{3.40}$$

and

$$y_{n_1 \ldots n_M} = \sum_{k_1 = 0}^{N_1} \cdots \sum_{k_M = 0}^{N_M} Y_{k_1 \ldots k_M} \exp\left[2\pi j\left(\frac{k_1 n_1}{N_1} + \ldots \frac{k_M n_M}{N_M}\right)\right], \tag{3.41}$$

where

$$N_{tot} = \prod_{m = 1}^{M} (2P_m + 1) \tag{3.42}$$

is the total number of samples present in (3.39). The Fourier coefficients $Y_{k_1 \ldots k_M}$ which were computed in (3.40) allow the *M*-dimensional waveform *y* to be represented as

$$y(t_1, \ldots, t_M) \approx \sum_{k_1 = 0}^{N_1} \cdots \sum_{k_M = 0}^{N_M} Y_{k_1 \ldots k_M} \exp\left[j\left(k_1 \Omega_1 t_1 + \ldots k_M \Omega_M t_M\right)\right]. \tag{3.43}$$

Exact equality in the relation above is prevented only by aliasing errors introduced by inadequate sampling. These errors can be minimized to an arbitrarily low level by increasing the sampling orders $N_1, \ldots, N_M$. At time points corresponding to the time samples in (3.39), the relationship holds ‘‘exactly’’ (i.e., to floating point precision).

Recall that our goal is to compute the quasi-Fourier coefficients of $g(x(t))$ for quasiperiodic waveforms $x(t)$. The quasiperiodicity of $x(t)$ allows the waveform to be expressed as

$$x(t) = \sum_{k_1 = -P_1}^{P_1} \cdots \sum_{k_M = -P_M}^{P_M} X_{k_1 \ldots k_M} \exp\left[j\left(k_1\Omega_1 + \ldots k_M\Omega_M\right) t\right] \tag{3.44}$$

where M fundamentals have been assumed, and a dual-sided representation of the waveform has been used for notational convenience. Corresponding to this waveform, we define the M-variable function

$$\hat{x}(t_1, \ldots, t_M) = \sum_{k_1 = -P_1}^{P_1} \cdots \sum_{k_M = -P_M}^{P_M} X_{k_1 \ldots k_M} \exp\left[j\left(k_1\Omega_1 t_1 + \ldots k_M\Omega_M t_M\right)\right] \tag{3.45}$$

and observe that $x(t) = \hat{x}(t, \ldots, t)$. Defining the M-dimensional sets of samples

$$\hat{x}_{n_1 \ldots n_M} = \hat{x}\left(\frac{2\pi n_1}{\Omega_1 (2P_1 + 1)}, \ldots, \frac{2\pi n_M}{\Omega_M (2P_M + 1)}\right), -P_m \le n_m \le P_m \text{ for } 1 \le m \le M \tag{3.46}$$

and

$$\hat{g}_{n_1 \ldots n_M} = g\left(\hat{x}_{n_1 \ldots n_M}\right), -P_m \le n_m \le P_m \text{ for } 1 \le m \le M \tag{3.47}$$

allows the application of an M-dimensional Discrete Fourier Transform to calculate the Fourier coefficients of $g(\hat{x}(t_1, \ldots, t_M))$:

$$G_{k_1 \ldots k_M} = \frac{1}{N_{tot}} \sum_{n_1 = -P_1}^{P_1} \cdots \sum_{n_M = -P_M}^{P_M} \hat{g}_{n_1 \ldots n_M} \exp\left[-2\pi j\left(\frac{k_1 n_1}{2P_1 + 1} + \ldots \frac{k_1 n_M}{2P_M + 1}\right)\right] \tag{3.48}$$

Following the discussion of the preceding paragraph, the spectral representation of $g(\hat{x}(t_1, \ldots, t_M))$ can be written as

$$g(\hat{x}(t_1, \ldots, t_M)) \approx \sum_{k_1 = -P_1}^{P_1} \cdots \sum_{k_M = -P_M}^{P_M} G_{k_1 \ldots k_M} \exp\left[j\left(k_1\Omega_1 t_1 + \ldots k_M\Omega_M t_M\right)\right], \tag{3.49}$$

and so

$$g(x(t)) = g(\hat{x}(t, \ldots, t)) \approx \sum_{k_1 = -P_1}^{P_1} \cdots \sum_{k_M = -P_M}^{P_M} G_{k_1 \ldots k_M} \exp[j(k_1\Omega_1 + \ldots k_M\Omega_M)t] \tag{3.50}$$

Thus, the spectral coefficients $G_{k_1 \ldots k_M}$ computed in (3.48) are in fact the actual spectral coefficients of $g(x(t))$, as desired. We reiterate that for accurate simulations, the orders P_m must be chosen such that aliasing errors are negligible, in which case the approximate equality above becomes numerically exact.

3.4 Formulating the Harmonic Balance Equations

The transforms described in the previous section are central to formulating the harmonic balance equations. In the single-tone (i.e., one fundamental) case, the DFT/FFT is used to transform between the time and frequency domains. For multi-tone problems, the frequency-remapping technique is employed in our work, rather than the multi-dimensional DFT.

Harmonic balance analysis is applicable when the state equations

$$\boldsymbol{g}(\boldsymbol{x}(t)) + \frac{d}{dt}\boldsymbol{q}(\boldsymbol{x}(t)) + y(t) \otimes \boldsymbol{x}(t) - \boldsymbol{w}(t) = 0 \tag{3.51}$$

are driven by a quasiperiodic stimulus vector $\boldsymbol{w}(t)$, as is assumed here. Thus, we consider an M-tone stimulus of the form

$$\boldsymbol{w}(t) = \boldsymbol{W}_0 + \sum_{m=1}^{M} \left(\boldsymbol{W}_m^R \cos(\Omega_m t) - \boldsymbol{W}_m^I \sin(\Omega_m t) \right) , \tag{3.52}$$

where $\boldsymbol{W}_m^R$ and $\boldsymbol{W}_m^I$ are the real (cosine) and the imaginary (negative sine) portion of the stimulus vectors, respectively, for the m-th tone.[1] As discussed in Section 3.2.2, the steady state response to such an input will contain spectral components at the set of frequencies

1. In practice, the stimulus vector can also include spectral tones at mixing frequencies. This is not shown for notational simplicity.

$$\omega_{k_1 k_2 \ldots k_M} = k_1\Omega_1 + k_2\Omega_2 + \ldots + k_M\Omega_M . \tag{3.53}$$

Truncating this frequency set to a total of H harmonics allows us to expand each state variable as a quasi-Fourier series

$$x_n(t) = X_{n0} + \sum_{h=1}^{H} \left(X_{nh}^R \cos(\omega_h t) - X_{nh}^I \sin(\omega_h t) \right) , \tag{3.54}$$

where $\omega_h \in W_P, 0 \le h \le H$. P, and thus H, must be chosen large enough so that the contribution from the neglected frequencies is insignificant. The goal of the harmonic balance analysis is to determine the quasi-Fourier coefficients X_{nh}^R and X_{nh}^I such that (3.51) is satisfied for the given stimulus.

3.4.1 The HB "Right Hand Side" (RHS) Residual

To proceed toward solving the system, we define the time domain right-hand side (RHS) residual vector as

$$\boldsymbol{f}(\boldsymbol{x}(t);t) = \boldsymbol{g}(\boldsymbol{x}(t)) + \frac{d}{dt}\boldsymbol{q}(\boldsymbol{x}(t)) + y(t) \otimes \boldsymbol{x}(t) - \boldsymbol{w}(t) . \tag{3.55}$$

In general, since there are only $2H + 1$ degrees of freedom in the quasiperiodic expansion (3.54), we can expect to drive the residual vector to zero only at $2H + 1$ time points, which are sometimes referred to as ''collocation points.'' A variant of harmonic balance, dubbed waveform balance [28], formulates the nonlinear problem by using frequency domain state vectors (such as (3.54)) while representing the residual in the time domain at a finite number of collocation points. Four straightforward variants on harmonic balance are possible, since both the state vector and the residual can be represented either in the time or frequency domains. Although any of the four choices should have very similar nonlinear solve properties, their Jacobian matrices would at first glance appear to be quite different. However, because each of these four Jacobians are related to each other through pre- or post-multiplication with Fourier Transform matrices, the choice of which formulation to use should have minimal repercussions in practice.

In the standard harmonic balance algorithm [27], both the state vector and the residual are represented in the frequency domain. The convolution term $y(t) \otimes \boldsymbol{x}(t)$ becomes a simple frequency domain product. The nonlinearities $\boldsymbol{g}$ and $\boldsymbol{q}$, on the other hand, must be sampled in the time domain, and then transformed into the frequency domain through application of a quasiperiodic transform. For this purpose, we use the artificially remapped

waveforms $\hat{\boldsymbol{x}}(t)$, as in (3.26). Assuming that $2S$ samples are enough to adequately represent $\boldsymbol{g}(\hat{\boldsymbol{x}}(t))$ and $\boldsymbol{q}(\hat{\boldsymbol{x}}(t))$, the desired quasi-Fourier coefficients at the nth state equation can be computed through Γ, the single-sided DFT operator of Section 3.1.2:

$$\begin{bmatrix} G_{n0}^R \\ G_{n1}^R \\ G_{n1}^I \\ | \\ G_{n,S-1}^R \\ G_{n,S-1}^I \\ G_{n,S}^R \end{bmatrix} = \Gamma \begin{bmatrix} g_n(\hat{\boldsymbol{x}}(t_0)) \\ g_n(\hat{\boldsymbol{x}}(t_1)) \\ g_n(\hat{\boldsymbol{x}}(t_2)) \\ | \\ g_n(\hat{\boldsymbol{x}}(t_{2S-3})) \\ g_n(\hat{\boldsymbol{x}}(t_{2S-2})) \\ g_n(\hat{\boldsymbol{x}}(t_{2S-1})) \end{bmatrix} \text{ and } \begin{bmatrix} Q_{n0}^R \\ Q_{n1}^R \\ Q_{n1}^I \\ | \\ Q_{n,S-1}^R \\ Q_{n,S-1}^I \\ Q_{n,S}^R \end{bmatrix} = \Gamma \begin{bmatrix} q_n(\hat{\boldsymbol{x}}(t_0)) \\ q_n(\hat{\boldsymbol{x}}(t_1)) \\ q_n(\hat{\boldsymbol{x}}(t_2)) \\ | \\ q_n(\hat{\boldsymbol{x}}(t_{2S-3})) \\ q_n(\hat{\boldsymbol{x}}(t_{2S-2})) \\ q_n(\hat{\boldsymbol{x}}(t_{2S-1})) \end{bmatrix} \tag{3.56}$$

where $t_s = \frac{2\pi s}{2S}$. A suitable mapping function $\mu(h)$ allows us to form the frequency domain residual from the above coefficients:

$$F_{nh}(\boldsymbol{X}) = G_{n,\mu(h)}(\boldsymbol{X}) + j\omega_h Q_{n,\mu(h)}(\boldsymbol{X}) + \sum_{l=1}^{N} Y_{nl}(\omega_h) X_{lh} - W_{nh}, \tag{3.57}$$

where $0 \le h \le H$, $1 \le n \le N$, and $0 \le \mu(h) \le S-1$. This is the nonlinear system of harmonic balance equations which is to be solved for $\boldsymbol{X}$.

As mentioned in Section 3.1.1, the Fourier component in the highest bin of an even-order DFT (i.e., $G_{n,S}^R$ and $Q_{n,S}^R$) is "artificial" in the sense that it does not accurately represent the true spectral energy present in that bin. The constraint on μ in the preceding paragraph guarantees that harmonic balance residual equations will never be formed at this "non-physical" frequency. This implies that $2S$, the number of time samples, needs to satisfy the inequality $S-1 \ge H$.

The system (3.57) is written as a set of HN complex nonlinear equations in as many unknowns. Because the system is not analytic, we reformulate it by splitting it into real and imaginary parts. Since the DC sine component is always zero, the system can be represented as a set of $(2H+1)N$ real equations in as many unknowns:

$$F_{nh}^R = G_{n,\mu(h)}^R - \omega_h Q_{n,\mu(h)}^I + \sum_{l=1}^{N} \left(Y_{nl}^R(\omega_h) X_{lh}^R - Y_{nl}^I(\omega_h) X_{lh}^I \right) - W_{nh}^R \tag{3.58}$$

$$F^I_{nh} = G^I_{n,\mu(h)} + \omega_h Q^R_{n,\mu(h)} + \sum_{l=1}^{N} \left(Y^R_{nl}(\omega_h) X^l_{lh} + Y^I_{nl}(\omega_h) X^R_{lh} \right) - W^I_{nh} \quad (3.59)$$

In compact notation, we write

$$\boldsymbol{F}(\boldsymbol{X}) = \boldsymbol{0}, \quad (3.60)$$

where $\boldsymbol{F} \in \Re^{N(2H+1)\times 1}$ and $\boldsymbol{X} \in \Re^{N(2H+1)\times 1}$ denote the vectors of F_{nh} and X_{nh}, respectively:

$$\boldsymbol{F} = [\boldsymbol{F}_1, \boldsymbol{F}_2, \ldots, \boldsymbol{F}_N]^T, \ \boldsymbol{F}_n = \left[F^R_{n0}, F^R_{n1}, F^I_{n1}, \ldots, F^R_{nH}, F^I_{nH}\right]^T \quad (3.61)$$

and

$$\boldsymbol{X} = [\boldsymbol{X}_1, \boldsymbol{X}_2, \ldots, \boldsymbol{X}_N]^T, \ \boldsymbol{X}_n = \left[X^R_{n0}, X^R_{n1}, X^I_{n1}, \ldots, X^R_{nH}, X^I_{nH}\right]^T. \quad (3.62)$$

Some authors prefer, instead, to write down the harmonic balance equations in the complex domain, with an assumed complex-conjugate relationship between the positive- and negative-frequency components [39]. The two formulations are equivalent when matrix-implicit solution methods are brought to bear, but Jacobian storage for the real-only formulation is only half the size of the complex-conjugate formulation when direct methods are employed [27].

Although equations (3.58)-(3.59) are rigorously correct, they can be somewhat cumbersome to write down and work with (particularly when developing expressions for the Jacobian matrix). The notational difficulty comes largely from the presence of the remapping function $\mu(h)$, and can be removed by assuming a one-tone analysis where $\mu(h) = h$. With this simplification, the residual vector can be written in compact operator notation as

$$\boldsymbol{F}(\boldsymbol{X}) = \Gamma_N \boldsymbol{g}\left(\Gamma_N^{-1}\boldsymbol{X}\right) + \Omega_N \Gamma_N \boldsymbol{q}\left(\Gamma_N^{-1}\boldsymbol{X}\right) + Y\boldsymbol{X}, \quad (3.63)$$

where $\Gamma_N \in \Re^{N(2H+1)\times N(2H+1)}$ is a block-diagonal matrix of DFT blocks[1]

$$\Gamma_N = \begin{bmatrix} \Gamma & & \\ & \ddots & \\ & & \Gamma \end{bmatrix} \quad (3.64)$$

and $\Omega_N \in \Re^{N(2H+1)\times N(2H+1)}$ is a block-diagonal matrix representing the derivative operation:

1. This is not to be confused with an N-point DFT transform.

$$\Omega_N = \begin{bmatrix} \Omega & & \\ & \ddots & \\ & & \Omega \end{bmatrix}, \quad \Omega = \begin{bmatrix} \varpi_0 & & \\ & \ddots & \\ & & \varpi_H \end{bmatrix} \tag{3.65}$$

where $\varpi_h = \begin{bmatrix} 0 & -\omega_h \\ \omega_h & 0 \end{bmatrix}$ and $\varpi_0 = 0$.

In the simplified notation of the preceding paragraph, an odd DFT size of $(2H+1)$ was assumed. Practical implementations of the HB algorithm utilize a power-of-2 transform matrix to exploit the speed of the FFT. Remapping functions are applied to discard ‘‘unmapped’’ frequency bins, thus reducing the total number of harmonics for the nonlinear solve to $(2H+1)$. From here on out, unless specifically noted otherwise, we will use the simplified HB formulation of the preceding paragraph in deriving results. The extension of these results to scenarios with real-life remapping functions is straightforward in practice, though perhaps somewhat inconvenient notationally.

3.4.2 The HB Jacobian

The harmonic balance Jacobian can be derived by applying the chain rule to differentiate (3.63):

$$\boldsymbol{F}'(\boldsymbol{X}) = \frac{\partial \boldsymbol{F}}{\partial \boldsymbol{X}}(\boldsymbol{X}) = \Gamma_N \cdot \frac{\partial \boldsymbol{g}}{\partial \boldsymbol{x}}\left(\Gamma_N^{-1}\boldsymbol{X}\right) \cdot \Gamma_N^{-1} + \Omega_N \Gamma_N \cdot \frac{\partial \boldsymbol{q}}{\partial \boldsymbol{x}}\left(\Gamma_N^{-1}\boldsymbol{X}\right) \cdot \Gamma_N^{-1} + Y. \tag{3.66}$$

In the equation above, the derivative matrices $\partial \boldsymbol{g}/\partial \boldsymbol{x} \in \Re^{N(2H+1) \times N(2H+1)}$ and $\partial \boldsymbol{q}/\partial \boldsymbol{x} \in \Re^{N(2H+1) \times N(2H+1)}$ take the $N \times N$ block form

$$\frac{\partial \boldsymbol{g}}{\partial \boldsymbol{x}} = \begin{bmatrix} \frac{\partial \boldsymbol{g}_1}{\partial \boldsymbol{x}_1} & \frac{\partial \boldsymbol{g}_1}{\partial \boldsymbol{x}_2} & \cdots & \frac{\partial \boldsymbol{g}_1}{\partial \boldsymbol{x}_N} \\ \frac{\partial \boldsymbol{g}_2}{\partial \boldsymbol{x}_1} & \frac{\partial \boldsymbol{g}_2}{\partial \boldsymbol{x}_2} & \cdots & \frac{\partial \boldsymbol{g}_2}{\partial \boldsymbol{x}_1} \\ \vdots & \vdots & \ddots & \vdots \\ \frac{\partial \boldsymbol{g}_N}{\partial \boldsymbol{x}_1} & \frac{\partial \boldsymbol{g}_N}{\partial \boldsymbol{x}_2} & \cdots & \frac{\partial \boldsymbol{g}_N}{\partial \boldsymbol{x}_N} \end{bmatrix}, \tag{3.67}$$

where in turn each block $\frac{\partial \boldsymbol{g}_n}{\partial \boldsymbol{x}_m} \in \Re^{(2H+1)\times(2H+1)}$ is a diagonal matrix

$$\frac{\partial \boldsymbol{g}_n}{\partial \boldsymbol{x}_m} = \begin{bmatrix} \lambda_0 & & & \\ & \lambda_1 & & \\ & & \backslash & \\ & & & \lambda_{2H} \end{bmatrix}, \text{ where } \lambda_s = \frac{\partial g_n}{\partial x_m}(\boldsymbol{x}(t_s)) . \tag{3.68}$$

A completely analogous relationship holds for the charge derivative matrix $\partial \boldsymbol{q} / \partial \boldsymbol{x}$. We reiterate that the $(2H+1)\times(2H+1)$ time domain block size is used here strictly for notational simplicity, in order to avoid cumbersome remapping functions. In practice, the block size would be $2S \times 2S$, with S being a power-of-2 for FFT compatibility.

From the above discussion, it is apparent that the frequency domain Jacobian can be viewed as an $N \times N$ block matrix of $(2H+1)\times(2H+1)$ blocks.[1] That is, the Jacobian structure takes the form

$$\frac{\partial \boldsymbol{F}}{\partial \boldsymbol{X}}(\boldsymbol{X}) = \begin{bmatrix} \frac{\partial \boldsymbol{F}_1}{\partial \boldsymbol{X}_1} & \frac{\partial \boldsymbol{F}_1}{\partial \boldsymbol{X}_2} & \cdots & \frac{\partial \boldsymbol{F}_1}{\partial \boldsymbol{X}_N} \\ \frac{\partial \boldsymbol{F}_2}{\partial \boldsymbol{X}_1} & \frac{\partial \boldsymbol{F}_2}{\partial \boldsymbol{X}_2} & \cdots & \frac{\partial \boldsymbol{F}_2}{\partial \boldsymbol{X}_N} \\ | & | & \backslash & | \\ \frac{\partial \boldsymbol{F}_N}{\partial \boldsymbol{X}_1} & \frac{\partial \boldsymbol{F}_N}{\partial \boldsymbol{X}_2} & \cdots & \frac{\partial \boldsymbol{F}_N}{\partial \boldsymbol{X}_N} \end{bmatrix}, \tag{3.69}$$

where each block $\partial \boldsymbol{F}_n / \partial \boldsymbol{X}_m$ is written as

$$\begin{aligned} \frac{\partial \boldsymbol{F}_n}{\partial \boldsymbol{X}_m} &= \frac{\partial \boldsymbol{G}_n}{\partial \boldsymbol{X}_m} + \Omega \frac{\partial \boldsymbol{Q}_n}{\partial \boldsymbol{X}_m} + Y_{nm} \\ &= \Gamma \cdot \frac{\partial \boldsymbol{g}}{\partial \boldsymbol{x}}\left(\Gamma_N^{-1}\boldsymbol{X}\right) \cdot \Gamma^{-1} + \Omega\Gamma \cdot \frac{\partial \boldsymbol{q}}{\partial \boldsymbol{x}}\left(\Gamma_N^{-1}\boldsymbol{X}\right) \cdot \Gamma^{-1} + Y_{nm} \end{aligned} . \tag{3.70}$$

1. These frequency domain blocks truly are 2*H*+1 by 2*H*+1, regardless of the dimensionality of the time domain blocks.

Each such block is sometimes referred to as a conversion matrix. We point out that although each such conversion matrix may be structurally dense, the $N \times N$ block structure retains the sparsity pattern of the original scalar $N \times N$ time domain Jacobian.

3.5 Solving The Harmonic Balance Equations With Direct Methods

Historically, numerous approaches have been taken to solve the nonlinear system of harmonic balance equations. These have included the Newton-Raphson method (using both direct and iterative linear solvers), nonlinear programming techniques [21], and many different nonlinear relaxation schemes. Whether or not a given solution algorithm is optimal depends on several factors, the most important of which include the size of the problem and the levels of nonlinear distortion present in the system. In this section, we will focus on the direct Newton-Raphson method [24], which is perhaps the most widely used nonlinear solution technique in existence today. Although this technique is not directly applicable to large scale semiconductor device simulation problems, a good understanding of it is essential to developing more suitable algorithms. The two subsequent chapters will present such algorithms.

3.5.1 Newton's Method

The lth iteration ($l \geq 1$) of Newton-Raphson applied to (3.60) is

$$\boldsymbol{X}^{(l)} = \boldsymbol{X}^{(l-1)} - \left[\frac{\partial \boldsymbol{F}}{\partial \boldsymbol{X}}(\boldsymbol{X}^{(l-1)})\right]^{-1} \boldsymbol{F}\left(\boldsymbol{X}^{(l-1)}\right), \tag{3.71}$$

where $\boldsymbol{X}^{(l)}$ is the state vector at iteration l, with $\boldsymbol{X}^{(0)}$ being the initial guess. The key step in this procedure is the accurate construction and factorization of the harmonic balance Jacobian $\partial \boldsymbol{F} / \partial \boldsymbol{X}$. When this step is done with no approximations, the iterative process (3.71) will exhibit locally quadratic convergence under assumptions which are usually satisfied in practice.

As shown in the previous section, the HB Jacobian can be viewed as a sparse matrix of dense blocks. When direct LU-factorization methods are applied, the memory needed to store the factored matrix scales as $O(N^{\alpha}H^2)$, while the time needed to factor the matrix scales as $O(N^{\beta}H^3)$ (α and β are problem-specific constants which depend on the

sparsity of the time domain Jacobian, with $1 \le \alpha \le 2$ and $1 \le \beta \le 3$.) To appreciate the extremely rapid growth that occurs as the number of harmonics is increased, we consider a device structure that requires 10MB of RAM to simulate at DC. If this same structure were to be simulated via harmonic balance at only 15 harmonics, the memory required would top 9.5 GB. A two-tone analysis at 100 harmonics would require over 400 GB of RAM. To make matters worse, this quadratic growth in memory requirements is overshadowed by the *cubic* growth in simulation time.

Clearly, Newton's method based on direct LU-factorization is unsuitable for simulating large-scale semiconductor device structures. It is thoroughly impractical to explicitly form, much less factor, the harmonic balance Jacobian for realistic device simulation problems. Nevertheless, an understanding of the sparse matrix techniques and data structures used to directly factor ''small'' HB Jacobians is useful for a number of reasons. Some nonlinear relaxation-based methods [3], for example, make use of smaller Jacobians, and consequently can utilize direct LU factorization techniques. More importantly, the Krylov subspace solution methods described in Chapter 4 require direct factorization of preconditioning matrices which approximate the Jacobian. Valuable insight into their structure and decomposition can be gained by examining the algorithms for the explicit formation and factorization of the HB Jacobian. The subsequent two sections seek to offer concise coverage of these topics. For more detail from a slightly different perspective, the reader is referred to [27].

3.5.2 Explicitly Forming the Harmonic Balance Jacobian

The sine (or imaginary) part of the DC Fourier coefficient is always zero for real waveforms. Consequently, it is left out of our HB formulation (3.61) — (3.62). In those equations, each of the residual ($\boldsymbol{F}_n$) and state variable ($\boldsymbol{X}_n$) spectral expansions have dimensionality $2H+1$, rather than $2H+2$. However, for the purpose of direct LU factorization of the Jacobian $\partial \boldsymbol{F} / \partial \boldsymbol{X}$, it is convenient to use a dimensionality of $2H+2$ (i.e., to include the DC sine component) in order to avoid special-case handling of the DC harmonic. For the linear solution step, then, a ''padded'' right hand side residual vector of the form

$$\boldsymbol{F}_n = \left[F_{n0}^R, 0, F_{n1}^R, F_{n1}^I, \ldots, F_{nH}^R, F_{nH}^I\right]^T \tag{3.72}$$

will be used to match the increased dimensionality of the augmented matrix $\partial \boldsymbol{F} / \partial \boldsymbol{X}$. The augmentation will be such that the update $-(\partial \boldsymbol{F} / \partial \boldsymbol{X})^{-1} \boldsymbol{F}(\boldsymbol{X})$ contains identically zero entries for all DC sine components.

The entries of the explicit $N(2H+2) \times N(2H+2)$ harmonic balance Jacobian consist of the terms $\partial F_{nh}^R / \partial X_{mi}^R$, $\partial F_{nh}^R / \partial X_{mi}^I$, $\partial F_{nh}^I / \partial X_{mi}^R$, and $\partial F_{nh}^I / \partial X_{mi}^I$ for $1 \le n \le N$, $0 \le h \le H$. Each such collection corresponds to a *quad*, which is a 2×2 matrix of the form

$$\boldsymbol{\Phi}_{nm}^{hi} = \begin{bmatrix} \dfrac{\partial F_{nh}^R}{\partial X_{mi}^R} & \dfrac{\partial F_{nh}^R}{\partial X_{mi}^I} \\ \dfrac{\partial F_{nh}^I}{\partial X_{mi}^R} & \dfrac{\partial F_{nh}^I}{\partial X_{mi}^I} \end{bmatrix} \tag{3.73}$$

representing the derivative of the complex function[1] $F_{nh}(\boldsymbol{X}) = F_{nh}^R(\boldsymbol{X}) + jF_{nh}^I(\boldsymbol{X})$ with respect to the complex variable $X_{mi} = X_{mi}^R + jX_{mi}^I$. These quads are grouped into blocks (sometimes referred to as *conversion matrices*) having quad dimensionality $(H+1) \times (H+1)$ (or $(2H+2) \times (2H+2)$ if measured in reals as opposed to quads). There is a structurally non-zero harmonic balance block corresponding to every structurally non-zero time domain Jacobian entry $\partial f_n / \partial x_m$ (Figure 3.6). The conversion matrix associated with this (*n*, *m*) entry has the form

$$\frac{\partial \boldsymbol{F}_n}{\partial \boldsymbol{X}_m} = \begin{bmatrix} \boldsymbol{\Phi}_{nm}^{00} & \boldsymbol{\Phi}_{nm}^{01} & \cdots & \boldsymbol{\Phi}_{nm}^{0H} \\ \boldsymbol{\Phi}_{nm}^{10} & \boldsymbol{\Phi}_{nm}^{11} & \cdots & \boldsymbol{\Phi}_{nm}^{1H} \\ | & | & \backslash & | \\ \boldsymbol{\Phi}_{nm}^{H0} & \boldsymbol{\Phi}_{nm}^{H1} & \cdots & \boldsymbol{\Phi}_{nm}^{HH} \end{bmatrix}. \tag{3.74}$$

To compute the value of each quad, we differentiate (3.58)-(3.59) to obtain

$$\frac{\partial F_{nh}^R}{\partial X_{mi}^R} = \frac{\partial G_{nh}^R}{\partial X_{mi}^R} - \omega_h \frac{\partial Q_{nh}^I}{\partial X_{mi}^R} + Y_{nm}^R(\omega_h) \tag{3.75}$$

1. Quads, rather than complex numbers, are necessary to represent the derivative because F_{nh} is not in general analytic in our formulation.

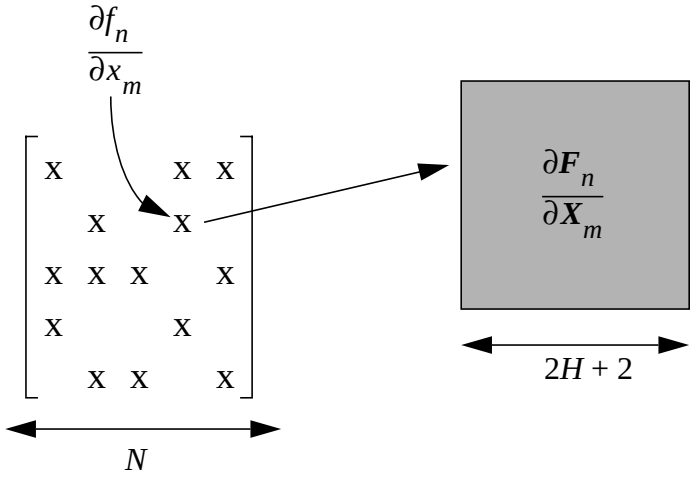

Figure 3.6 In forming the explicit harmonic balance Jacobian, each structurally non-zero entry in the DC/time-domain Jacobian (left) inflates into a dense $(2H + 2) \times (2H + 2)$ conversion matrix, or ‘‘block,’’ (right).

$$\frac{\partial F^R_{nh}}{\partial X^I_{mi}} = \frac{\partial G^R_{nh}}{\partial X^I_{mi}} - \omega_h \frac{\partial Q^I_{nh}}{\partial X^I_{mi}} - Y^I_{nm}(\omega_h) \tag{3.76}$$

$$\frac{\partial F^I_{nh}}{\partial X^R_{mi}} = \frac{\partial G^I_{nh}}{\partial X^R_{mi}} + \omega_h \frac{\partial Q^R_{nh}}{\partial X^R_{mi}} + Y^I_{nm}(\omega_h) \tag{3.77}$$

$$\frac{\partial F^I_{nh}}{\partial X^I_{mi}} = \frac{\partial G^I_{nh}}{\partial X^I_{mi}} + \omega_h \frac{\partial Q^R_{nh}}{\partial X^I_{mi}} + Y^R_{nm}(\omega_h) \tag{3.78}$$

The only step remaining is to determine the scalar derivatives $\partial G^R_{nh}/\partial X^R_{mi}$, $\partial G^R_{nh}/\partial X^I_{mi}$, $\partial G^I_{nh}/\partial X^R_{mi}$, $\partial G^I_{nh}/\partial X^I_{mi}$ along with their charge counterparts. We go through the derivation here for $\partial G^R_{nh}/\partial X^R_{mi}$; the calculation of the other quad components is directly analogous. Recall that, from earlier definitions,

$$G_{nh}^{R} = \frac{2-\delta_h}{2S}\sum_{s=0}^{2S-1} g_n(\hat{\mathbf{x}}(t_s))\cos\left(\frac{2\pi hs}{2S}\right), \tag{3.79}$$

and

$$\hat{x}_m(t_s) = X_{m0}^{R} + \sum_{h=1}^{H}\left(X_{mh}^{R}\cos\left(\frac{2\pi hs}{2S}\right) - X_{mh}^{I}\sin\left(\frac{2\pi hs}{2S}\right)\right) \tag{3.80}$$

Applying the chain rule to the above equations results in

$$\begin{aligned}\frac{\partial G_{nh}^{R}}{\partial X_{mi}^{R}} &= \frac{2-\delta_h}{2S}\sum_{s=0}^{2S-1}\left(\frac{\partial}{\partial x_m}g_n(\hat{\mathbf{x}}(t_s))\cdot\frac{\partial \hat{x}_m}{\partial X_{mi}^{R}}\right)\cos\left(\frac{2\pi hs}{2S}\right) \\ &= \frac{2-\delta_h}{2S}\sum_{s=0}^{2S-1}\left(\frac{\partial}{\partial x_m}g_n(\hat{\mathbf{x}}(t_s))\right)\cos\left(\frac{2\pi is}{2S}\right)\cos\left(\frac{2\pi hs}{2S}\right)\end{aligned} \tag{3.81}$$

Note that a naive application of (3.81) results in $O(S)$ floating point operations per quad entry. Since there are H^2 quads per block, the total workload would appear to be $O\left(H^2 S\right)$ at first glance. Although this computational expense would be partially masked by the fact that the matrix factorization algorithms themselves are $O\left(H^3\right)$, it would nevertheless pose a significant burden.

Kundert et al. [27] have presented an $O(H^2)$ algorithm for explicitly forming the harmonic balance blocks. The approach is based on Fourier transforming the samples

$$\lambda_s = \frac{\partial g_n}{\partial x_m}(\hat{\mathbf{x}}(t_s)) \tag{3.82}$$

into the frequency domain, and splitting each Jacobian block into a sum of Toeplitz and Hankel matrices.[1] This algorithm may be derived from (3.81) by multiplying out the matrices and using the sine and cosine product identities

$$\begin{aligned}\cos(\alpha)\cos(\beta) &= \frac{1}{2}(\cos(\alpha+\beta)+\cos(\alpha-\beta)) \\ \sin(\alpha)\sin(\beta) &= \frac{1}{2}(\cos(\alpha-\beta)-\cos(\alpha+\beta)) \\ \sin(\alpha)\cos(\beta) &= \frac{1}{2}(\sin(\alpha+\beta)+\sin(\alpha-\beta))\end{aligned} \tag{3.83}$$

1. Toeplitz matrices have entries given by $a_{ij}=t_{i-j}$. Hankel matrices have entries given by $a_{ij}=h_{i+j}$. See [48] for more details.

When the first of these identities is applied to $\partial G^R_{nh} / \partial X^R_{mi}$ in (3.81), we obtain

$$\frac{\partial G^R_{nh}}{\partial X^R_{mi}} = \frac{1 - \frac{1}{2}\delta_h}{2S}\left(\sum_{s=0}^{2S-1} \lambda_s \cos\left(\frac{2\pi (h+i)\, s}{2S} \right) + \sum_{s=0}^{2S-1} \lambda_s \cos\left(\frac{2\pi (h-i)\, s}{2S} \right) \right) \tag{3.84}$$
$$= \left(\frac{\Lambda^R_{h+i}}{2 - \delta_{h+i}} + \frac{\Lambda^R_{h-i}}{2 - \delta_{h-i}} \right)\left(1 - \tfrac{1}{2}\delta_h \right)$$

where $\left[\Lambda^R_0, 0, \Lambda^R_1, \Lambda^I_1, \ldots, \Lambda^R_{S-1}, \Lambda^I_{S-1}, \Lambda^R_S \right]^T$ is the single-sided Fourier transform of the samples λ_s. Applying the other two identities in (3.83) to the three remaining quad entries results in analogous formulas, and yields the Toeplitz-Hankel decomposition

$$\Phi^{hi} = \left(\frac{T_{h-i}}{2 - \delta_{h-i}} + \frac{H_{h+i}}{2 - \delta_{h+i}} \right)\left(1 - \tfrac{1}{2}\delta_h \right) \tag{3.85}$$

where the Toeplitz and Hankel quads are defined as

$$T_k = \begin{bmatrix} \Lambda^R_k & -\Lambda^I_k \\ \Lambda^I_k & \Lambda^R_k \end{bmatrix} \text{ and } H_k = \begin{bmatrix} \Lambda^R_k & \Lambda^I_k \\ \Lambda^I_k & -\Lambda^R_k \end{bmatrix}, \tag{3.86}$$

respectively. An important consequence of the preceding equations is that each quad $\Phi^{0i} = \frac{1}{2 - \delta_i} \frac{1}{2} (T_{-i} + H_i)$ in the top row of every block has the form

$$\Phi^{0i} = \frac{1}{2 - \delta_i} \begin{bmatrix} \Lambda^R_i & \Lambda^I_i \\ 0 & 0 \end{bmatrix} \tag{3.87}$$

Clearly, this implies that the Jacobian as given as by (3.86) is singular, because each of the N rows corresponding to the artificial DC-sine harmonic is identically zero. Given the artificial nature of the DC-sine term augmentation, this result is not particularly surprising. The situation is easily remedied by introducing a 1.0 entry into the (2,2) — or imag/imag — spot of the Φ^{00} quad of every block which is positioned on the matrix diagonal. This fixes the singularity without disturbing the desired solution, while at the same time ensuring that any update

$$\Delta \boldsymbol{X} = -\left(\frac{\partial \boldsymbol{F}}{\partial \boldsymbol{X}} \right)^{-1} \boldsymbol{F}(\boldsymbol{X}) \tag{3.88}$$

will result in identically zero DC-sine entries when $\boldsymbol{F}(\boldsymbol{X})$ has the form (3.72).

3.5.3 Factoring The Harmonic Balance Jacobian

LU factorization of the HB Jacobian is most effectively performed using block operations. Consider the block matrix

$$J = \begin{bmatrix} B_{11} & B_{12} & \cdots & B_{1N} \\ B_{21} & B_{22} & \cdots & B_{2N} \\ | & | & \backslash & | \\ B_{N1} & B_{N2} & \cdots & B_{NN} \end{bmatrix}, \tag{3.89}$$

where B_{ij} are all square blocks of identical dimensions. In direct analogy with standard LU factorization algorithms, the block variant of the decomposition finds a permutation matrix Π and block matrices L and U such that

$$J = \Pi^{-1}LU = \Pi^{-1}\begin{bmatrix} L_{11} & & \cdots & \\ L_{21} & L_{22} & \cdots & \\ | & | & \backslash & | \\ L_{N1} & L_{N2} & \cdots & L_{NN} \end{bmatrix}\begin{bmatrix} U_{11} & U_{12} & \cdots & U_{1N} \\ 0 & U_{22} & \cdots & U_{2N} \\ | & | & \backslash & | \\ 0 & 0 & \cdots & U_{NN} \end{bmatrix}, \tag{3.90}$$

where L_{ij} and U_{ij} are square blocks having the same dimension as the B_{ij}. The diagonal blocks L_{ii} / U_{ii} are lower- and upper- triangular, respectively, while the remaining L_{ij} / U_{ij} are potentially full. The permutation matrix Π represents the pivoting operations performed during the decomposition to preserve sparsity and maintain numerical stability.

Conceptually, the factorization process may be presented as follows. Assuming that the B_{11} block is the first pivot[1], the matrix is partitioned as

$$\begin{bmatrix} B_{11} & B_{12} & \cdots & B_{1N} \\ B_{21} & B_{22} & \cdots & B_{2N} \\ | & | & \backslash & | \\ B_{N1} & B_{N2} & \cdots & B_{NN} \end{bmatrix} = \left[\begin{array}{c|c} A_{11} & A_{12} \\ \hline A_{21} & A_{22} \end{array}\right] \tag{3.91}$$

where $A_{11} = B_{11}$ is the pivot block. By inspection, the block-LU decomposition is then

1. Otherwise, a permutation of the rows/columns would be performed to (conceptually) move the pivot block into the upper left-hand corner.

$$\begin{bmatrix} A_{11} & A_{12} \\ A_{21} & A_{22} \end{bmatrix} = \begin{bmatrix} L_{11} & 0 \\ A_{21}U_{11}^{-1} & I \end{bmatrix} \begin{bmatrix} U_{11} & L_{11}^{-1}A_{12} \\ 0 & A_{22} - \left(A_{21}U_{11}^{-1}\right)\left(L_{11}^{-1}A_{12}\right) \end{bmatrix} , \tag{3.92}$$

and the first column of L, along with the first row of U, may be determined:

$$\begin{bmatrix} L_{21} \\ | \\ L_{N1} \end{bmatrix} = A_{21} , \tag{3.93}$$

$$\begin{bmatrix} U_{12} & \cdots & U_{1N} \end{bmatrix} = A_{12} . \tag{3.94}$$

The above decomposition procedure is then applied recursively to the resultant matrix $A_{22} - A_{21}A_{11}^{-1}A_{12}$ to obtain the remaining rows and columns of L and U.

When applied to factoring the HB Jacobian, sparse solvers based on the block-oriented algorithm presented above have several advantages over standard packages. One such advantage is memory usage — typically, each non-zero entry in standard sparse data structures takes up several extra bytes of overhead due to the need to establish its position within the matrix. This cost is avoided when block-oriented algorithms are used, since the overhead is incurred only once for each block (that is, once per $O(H^2)$ elements). Furthermore, the block-oriented structure improves factorization speed substantially. Since the elements are stored in dense arrays, they can be accessed efficiently for block operations such as dense block multiplications, additions, and subtractions. An additional benefit is a dramatic speed-up of the ‘‘symbolic factorization’’ stage — i.e., the determination of the pivoting order. Pivoting is done on a block-by-block basis, and since the number of blocks is $O(H^2)$ times smaller than the total number of structurally non-zero entries, the improvement can be quite sizeable for large H.

When exact Jacobians are being used, each block is either structurally full or diagonal. In circuit simulation, the block at position *(n,m)* is diagonal if only linear components are connected between nodes *n* and *m*, and structurally full if at least one nonlinear device is connected. In semiconductor device simulation, the vast of majority of the blocks are full, since the models used in the constitutive equations typically imply at least weakly nonlinear interaction between the state variables at the grid nodes. Although strictly speaking a block becomes structurally full when it corresponds to a nonlinearity of any strength, the off-diagonal entries tend to become extremely small as the level of

nonlinearity is decreased (see Section 3.5.4). Furthemore, in the one-tone case, the magnitude of the off-diagonal terms decreases gradually as a function of their distance from the diagonal.[1] This leads to a natural approximation of structurally full Jacobian blocks by banded matrices. Kundert's Harmonic-Relaxation-Newton scheme [27], for example, selects the bandwidth *BW* for each block through a heuristic of the form

$$\Lambda_h \le \mu \Lambda_0 \text{ for } h \le BW. \tag{3.95}$$

Ideally, the threshold constant μ is picked small enough (10^{-4} is a typical value) such that nonlinear convergence remains robust.

Block-oriented matrix factorization algorithms are extremely effective in handling the aforementioned combination of diagonal, banded, and full blocks. To see why, we first note that the LU factorization of a banded block of bandwidth *b* results in *L* and *U* matrices having bandwidths *b* (see Figure 3.7). Subsequent elimination operations

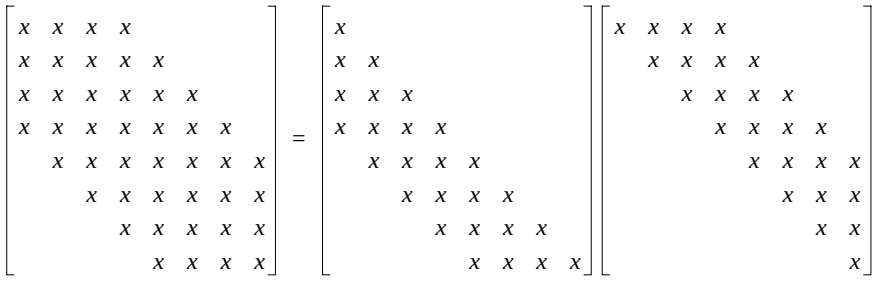

Figure 3.7 LU factorization of a banded harmonic balance pivot block. Note that the bandwidth of the L and U factors is equivalent to that of the original pivot block.

involve block products with L_{11}^{-1} and U_{11}^{-1}. These matrices are structurally diagonal if the pivot B_{11} is structurally diagonal, and so (in the diagonal case) do not increase the

1. In the multi-tone case, the situation is similar, but the stripes are spaced at constant intervals.

bandwidths of the blocks that they pre- or post-multiply. When the pivot is not purely diagonal, L_{11}^{-1} and U_{11}^{-1} become lower/upper triangular (respectively) and structurally full. Nevertheless, in harmonic balance applications the magnitude of the entries will decrease with distance from the diagonal, and a numerical bandwidth can be set. In general, when a block with bandwidth b_1 multiplies a block with bandwidth b_2, the resulting block will have a (structural) bandwidth $b_1 + b_2 - 1$. As the elimination process proceeds, the matrix blocks become more and more full. The pivoting algorithm should be chosen such that this level of fill is minimized. In particular, it is advantageous to pivot on those blocks which are diagonal, or, in the case where that's not possible, those that have a very small bandwidth.

3.5.4 The Harmonic Balance Jacobian at Low Distortion Levels

Studying the harmonic balance equations in the limiting case of low distortion is important for both practical and theoretical reasons. It is in the low distortion regime where harmonic balance exhibits its most significant performance advantages over transient simulation. There are numerous applications, such as highly linear single-transistor amplifier device design, where a very low level of distortion is precisely what the designer is trying to achieve. To analyze such problems, transient simulators must still place sample points closely enough to capture the sinusoidal waveforms, regardless of how few harmonics are being generated. Harmonic balance, on the other hand, can get away with expanding the waveforms into a small number of sinusoidal basis functions. Just as importantly, the harmonic balance Jacobian begins to assume a block diagonally-dominant form — a fact which can greatly speed its factorization, and provide an effective *preconditioner* for iterative linear solvers. This latter topic will be more fully explored in Chapter 4.

The non-autonomous systems of equations considered in this work have, by definition, zero AC response under DC-only stimulus (i.e., at zero AC input). We consider the case where the AC input is small enough such that the quasi-Fourier coefficients at each state variable

$$x_n(t) = X_{n0} + \sum_{h=1}^{H} \left(X_{nh}^R \cos(\omega_h t) - X_{nh}^I \sin(\omega_h t) \right) \tag{3.96}$$

satisfy the condition that

$$\sum_{h=1}^{H} \left| X_{nh} \right| \tag{3.97}$$

is ‘‘extremely small.’’ Letting $\boldsymbol{X}_{*,0} = [X_{10}, X_{20}, \ldots, X_{N0}]^T$ denote the state vector DC components, the nonlinear resistive functions can be approximated through a Taylor expansion as

$$g_n(\boldsymbol{x}(t)) \approx g_n(\boldsymbol{X}_{*,0}) + \sum_{m=1}^{N} \frac{\partial g_n}{\partial x_m}(\boldsymbol{X}_{*,0}) \sum_{h=1}^{H} \left(X_{mh}^R \cos(\omega_h t) - X_{mh}^I \sin(\omega_h t) \right) \tag{3.98}$$

which (by direct inspection) has the spectral representation

$$G_{n0} = g_n(\boldsymbol{X}_{*,0}) \tag{3.99}$$

$$G_{nh} = \sum_{m=1}^{N} \frac{\partial g_n}{\partial x_m}(\boldsymbol{X}_{*,0}) X_{mh}, \; h > 0. \tag{3.100}$$

In a directly analogous fashion, the spectral coefficients of the nonlinear charge functions q_n can be approximated as

$$Q_{n0} = q_n(\boldsymbol{X}_{*,0}) \tag{3.101}$$

$$Q_{nh} = \sum_{m=1}^{N} \frac{\partial q_n}{\partial x_m}(\boldsymbol{X}_{*,0}) X_{mh}, \; h > 0. \tag{3.102}$$

For notational convenience, we let $\Lambda_0^{nm} = (\partial g_n / \partial x_m)(\boldsymbol{X}_{*,0})$ denote the spectral resistive derivative DC coefficient, with $\Theta_0^{nm} = (\partial q_n / \partial x_m)(\boldsymbol{X}_{*,0})$ being the analogous capacitive DC term. Differentiating the equations (3.99) — (3.102) yields the result

$$\begin{aligned} \frac{\partial G_{nh}}{\partial X_{mi}} &= \delta_{h-i} \Lambda_0^{nm} \\ \frac{\partial Q_{nh}}{\partial X_{mi}} &= \delta_{h-i} \Theta_0^{nm} \end{aligned} \tag{3.103}$$

where δ_{h-i} is the Kronecker delta function — unity when $h = i$, and zero otherwise. Thus, we see that under the low distortion approximation of (3.98), differentiating the harmonic balance equations yields[1]

1. Here, we explicitly include the contribution from the convolution term of the constitutive equations.

$$\frac{\partial F_{nh}}{\partial X_{mh}} = \Lambda_0^{nm} + j\omega_h \Theta_0^{nm} + Y_{nm}(\omega_h) , \tag{3.104}$$

$$\frac{\partial F_{nh}}{\partial X_{mi}} = 0 \text{ for } i \neq h . \tag{3.105}$$

Written in matrix form, each Jacobian block has the representation

$$\frac{\partial \boldsymbol{F}_n}{\partial \boldsymbol{X}_m} = \begin{bmatrix} \Lambda_0^{nm} & 0 & \dots & 0 \\ 0 & \Lambda_0^{nm} & \dots & 0 \\ | & | & \backslash & | \\ 0 & 0 & \dots & \Lambda_0^{nm} \end{bmatrix} + \begin{bmatrix} j\omega_0 \Theta_0^{nm} & 0 & \dots & 0 \\ 0 & j\omega_1 \Theta_0^{nm} & \dots & 0 \\ | & | & \backslash & | \\ 0 & 0 & \dots & j\omega_H \Theta_0^{nm} \end{bmatrix} + \begin{bmatrix} Y_{nm}(\omega_0) & 0 & \dots & 0 \\ 0 & Y_{nm}(\omega_1) & \dots & 0 \\ | & | & \backslash & | \\ 0 & 0 & \dots & Y_{nm}(\omega_H) \end{bmatrix} \tag{3.106}$$

There are two key points regarding the above relationships. The first is that the equations become analytic — that is, the Jacobian entries are complex numbers, rather than quads. The second point is that each Jacobian block (now an $(H+1) \times (H+1)$ complex submatrix) is purely diagonal. This latter point is critical to fast and efficient factorization of the approximate low-distortion Jacobian matrix.

3.6 Summary

This chapter has presented an overview of harmonic balance algorithm fundamentals. When compared to transient analysis in the context of analog RF simulation, harmonic balance offers numerous advantages. These include the ability to directly capture the steady state response of nonlinear systems, almost complete insensitivity to wide frequency spacings of multi-tone spectral inputs, excellent handling of distributed linear elements, and good dynamic range for accurate resolution of low-distortion products. Much of HB's advantage over standard time domain methods is due to quasiperiodic transforms and remapping functions that are utilized in lieu of finite-difference methods or brute-force one-dimensional Fourier transforms. A survey of these was presented, and the

choice to use remapping functions instead of the multidimensional Fourier transform was made.

The formulation of the harmonic balance equations was discussed next. The formulation of both the right hand side residual and the Jacobian matrix was discussed. Given the large size of semiconductor device problems, direct solution methods are clearly impractical. Nevertheless, a section on direct solution methods was included, with some emphasis placed on the role that direct matrix factorization techniques play in the more suitable algorithmic approaches of the next two chapters.

Chapter 4

Solving the Harmonic Balance Equations with Newton-Iterative Methods

The Newton-Raphson algorithm is perhaps the most widely used technique for solving nonlinear systems of algebraic equations. Its chief strength lies in its locally quadratic convergence behavior when starting from sufficiently good initial guesses. When combined with continuation methods such as source-stepping or arclength continuation, Newton-Raphson is a robust and reliable method for solving the harmonic balance equations.

The first generation of practical harmonic balance circuit simulators relied primarily on Newton-Raphson with direct LU factorization as the central workhorse algorithm. As shown in Chapter 3, however, direct LU factorization methods result in memory usage and CPU time growth rates that are thoroughly impractical for large-scale systems of equations. As early as 1991, Newton-Iterative methods (also known as Inexact Newton methods) based on Krylov subspace linear solvers were proposed for solving the harmonic balance system of circuit equations [38]. Since then, other authors have successfully applied Krylov subspace solvers to large scale systems of HB circuit [39][42][44] and device [1][2] equations.

In this chapter, we present the basic theory of Krylov subspace solution methods, along with their application to solving systems of harmonic balance device equations. Standard preconditioners are reviewed, and novel preconditioners for solving multi-tone device distortion problems are presented. In addition, approximate spectral storage

schemes are developed for further reducing the memory required in large-scale device simulation problems.

4.1 Krylov Subspace Solution Techniques

Krylov subspace methods attempt to solve the linear problem

$$A\boldsymbol{x} = \boldsymbol{b} \tag{4.1}$$

by iteratively adjusting $\boldsymbol{x}$ to minimize some measure of error. In general, at the kth iteration, Krylov subspace methods minimize the error over the affine space

$$\boldsymbol{x}_0 + K_k, \tag{4.2}$$

where $\boldsymbol{x}_0$ is the initial iterate, and

$$K_k = \text{span}\left(\boldsymbol{r}_0, A\boldsymbol{r}_0, A^2\boldsymbol{r}_0, \ldots, A^{k-1}\boldsymbol{r}_0 \right) \tag{4.3}$$

is the kth Krylov subspace of matrix A, with initial residual of $\boldsymbol{r}_0 = \boldsymbol{b} - A\boldsymbol{x}_0$. Krylov solution methods have shown themselves to be superior to their stationary iterative counterparts such as SOR, Gauss-Seidel, etc. [48][50], and are the methods we focus on in this section.

A common aspect of all the Krylov subspace algorithms is their need to carry out matrix-vector products of the form $A\boldsymbol{v}_k$ (and possibly $A^T\boldsymbol{v}_k$) at each iteration k. The matrix A itself need never be explicitly stored so long as the matrix-vector products can be computed. It turns out that when A is a harmonic balance Jacobian, a compact representation for forming such products is readily available. We defer a description of harmonic balance matrix-vector products to Section 4.2, and first briefly present the basic theory underlying GMRES, our Krylov subspace algorithm of choice.

4.1.1 Generalized Minimum Residual (GMRES)

The Generalized Minimum RESidual Algorithm (GMRES) [46] was developed in 1986 as a general-purpose Krylov subspace method for nonsymmetric linear systems. The key idea behind GMRES is to minimize at the kth iteration the residual $\boldsymbol{r}_k = \boldsymbol{b} - A\boldsymbol{x}_k$ in the 2-norm over the space $\boldsymbol{x}_0 + K_k$. Formally, this amounts to solving the least squares problem

$$\min_{\boldsymbol{x}_k \in \boldsymbol{x}_0 + K_k} \left\| \boldsymbol{b} - A\boldsymbol{x}_k \right\|_2 \tag{4.4}$$

at each iteration k. Since the kth Krylov subspace contains k basis vectors, the least squares problem has k degrees of freedom.

If we let $V_k \in \Re^{N \times k}$ denote an orthonormal basis for K_k, the kth iterate can be written as

$$\boldsymbol{x}_k = \boldsymbol{x}_0 + V_k \boldsymbol{y}_k, \tag{4.5}$$

where $\boldsymbol{y}_k \in \Re^k$ is to be determined by the least squares equation(4.4):

$$\min_{\boldsymbol{y}_k \in \Re^k} \left\| \boldsymbol{b} - A(\boldsymbol{x}_0 + V_k \boldsymbol{y}_k) \right\|_2 = \min_{\boldsymbol{y}_k \in \Re^k} \left\| \boldsymbol{r}_0 - A V_k \boldsymbol{y}_k \right\|_2 . \tag{4.6}$$

The orthonormal basis V_k is constructed via the Arnoldi process, which is the Gram-Schmidt process applied to a given Krylov subspace. The k orthonormal columns of $V_k = [\boldsymbol{v}_1, \boldsymbol{v}_2, \ldots \boldsymbol{v}_k]$ are given by $\boldsymbol{v}_1 = \boldsymbol{r}_0 / \left\| \boldsymbol{r}_0 \right\|$ for the first column, and

$$\boldsymbol{v}_{i+1} = \frac{A\boldsymbol{v}_i - \sum_{l=1}^{i} \left(\boldsymbol{v}_l^T A \boldsymbol{v}_i \right) \boldsymbol{v}_l}{\left\| A\boldsymbol{v}_i - \sum_{l=1}^{i} \left(\boldsymbol{v}_l^T A \boldsymbol{v}_i \right) \boldsymbol{v}_l \right\|} \tag{4.7}$$

for subsequent columns ($i \geq 1$). In practice, the classical Gram-Schmidt algorithm as presented above suffers from numerical stability problems which cause the columns of V_k to lose their orthogonality [48]. In actual implementations, either modified Gram-Schmidt orthogonalization [48] or Householder reflections [47] are used to carry out the Arnoldi process. In theory, the Householder-Arnoldi algorithm is regarded as numerically more stable. In our experience, however, there is virtually no difference between the two approaches as far as harmonic balance device simulation is concerned.

The orthonormality of the basis matrix V_k allows the least squares problem (4.6) to be solved efficiently. From equation (4.7), one can readily derive the relationship [51]

$$A V_k = V_{k+1} H_k, \tag{4.8}$$

where $H_k \in \Re^{k+1 \times k}$ is upper Hessenberg — that is, upper triangular with a single stripe right below the diagonal. For example, at $k = 5$, H_5 would have the structure

$$H_5 = \begin{bmatrix} x & x & x & x & x \\ x & x & x & x & x \\ & x & x & x & x \\ & & x & x & x \\ & & & x & x \\ & & & & x \end{bmatrix}. \tag{4.9}$$

Taking advantage of the fact that $\boldsymbol{v}_1 = \boldsymbol{r}_0 / \|\boldsymbol{r}_0\|$ is the first column of V_k, we can re-write the least squares problem as

$$\min_{\boldsymbol{y}_k \in \Re^k} \|\boldsymbol{b} - A(\boldsymbol{x}_0 + V_k \boldsymbol{y}_k)\|_2 = \min_{\boldsymbol{y}_k \in \Re^k} \|V_{k+1}(\beta e_1 - H_k \boldsymbol{y}_k)\|_2 \tag{4.10}$$

where e_1 is a unit basis vector along the first dimension, and $\beta = \|\boldsymbol{r}_0\|$. Furthermore, because V_{k+1} is orthonormal, it has no impact on the 2-norm, and may thus be removed from the relation above to yield the upper Hessenberg least squares problem

$$\min_{\boldsymbol{y}_k \in \Re^k} \|\beta e_1 - H_k \boldsymbol{y}_k\|_2. \tag{4.11}$$

The QR factorization of the upper Hessenberg matrix H_k is readily performed through k Givens rotations [48]. Because Givens rotation matrices are orthonormal, they also do not affect the 2-norm in the least squares problem. For instance, applying the first two Givens rotations G_1 and G_2 to the example matrix H_5 in (4.9) would eliminate two of the lower-diagonal entries as follows:

$$G_2 G_1 H_5 = \begin{bmatrix} x & x & x & x & x \\ 0 & x & x & x & x \\ & 0 & x & x & x \\ & & x & x & x \\ & & & x & x \\ & & & & x \end{bmatrix}. \tag{4.12}$$

When all k Givens rotations are applied (let's write $G = G_k \cdot \ldots \cdot G_1$), the resulting matrix $R = GH_k$ assumes an upper triangular form, and the least squares problem

$$\min_{\boldsymbol{y}_k \in \Re^k} \|\beta e_1 - H_k \boldsymbol{y}_k\|_2 = \min_{\boldsymbol{y}_k \in \Re^k} \|\beta G e_1 - R \boldsymbol{y}_k\|_2 \tag{4.13}$$

becomes easy to solve.

One serious drawback of the GMRES algorithm as presented above is the storage cost associated with the orthonormal basis[1] V_k. Because an extra basis vector of size N has to be stored for each GMRES iteration, the storage cost can become prohibitive if many

iterations need to be taken. Consequently, it is necessary in practice to use a ‘‘restarted’’ variant of GMRES, where the iterative process begins anew after a fixed number of iterations. In practice, we have found a restart value of 10 to be more than enough for harmonic balance applications.

4.1.2 Other Krylov Subspace Algorithms

In addition to GMRES, several other Krylov subspace methods for solving indefinite non-symmetric systems exist. These include algorithms such Quasi-Minimal Residual (QMR) [53], Transpose-Free Quasi-Minimal Residual (TFQMR) [54], and Biconjugate Gradient Stabilized (BICGSTAB) [55]. In particular, the QMR family of algorithms are sometimes preferred over GMRES because they can execute in a fixed amount of storage which doesn’t increase with the iteration count. In some applications, restarted variants of GMRES are known to ‘‘stall’’ at a given value of the residual, and are not able to reduce the norm unless the restart value is increased. Because QMR algorithms do not need to be restarted, they are sometimes able to converge when GMRES cannot.

In this work, we have found restarted GMRES to be superior to QMR/TFQMR, both in terms of speed and in terms of robust convergence behavior. This is in all likelihood due to the relatively good preconditioners that are available for the harmonic balance problem. Because GMRES works so well relative to its alternatives for low values of the restart parameter, we use it exclusively in this work. All the results presented in subsequent sections are based on the Householder-Arnoldi variant of GMRES [47] using a restart value of 10, unless explicitly stated otherwise.

4.2 Matrix-Vector Products Involving the Harmonic Balance Jacobian

As we’ve seen, matrix-vector products are central to Krylov subspace solution algorithms. Fast computation of these products, along with efficient storage of the harmonic balance Jacobian representation, is essential for practical application of the

1. In the Householder variant of GMRES, it is the Householder vectors that are explicitly stored, rather than the orthonormal basis. The storage cost between the two methods is virtually identical for large problems.

algorithms to solving large-scale HB equations. In this section, we outline an FFT-based algorithm [39] that carries out the matrix-vector products in $O(S\log(S))$ floating point operations and $O(S)$ storage requirements, where S is the number of time samples used in the HB analysis. In Section 4.4, we will present algorithms which further reduce memory storage requirements, at the cost of slowing down the matrix-vector multiplies by a constant factor which is independent of the number of harmonics H or time samples S.

Recall from Section 3.4.2 that the harmonic balance Jacobian can be written as

$$\boldsymbol{F}'(\boldsymbol{X}) = \frac{\partial \boldsymbol{F}}{\partial \boldsymbol{X}}(\boldsymbol{X}) = \Gamma_N \cdot \frac{\partial \boldsymbol{g}}{\partial \boldsymbol{x}}\left(\Gamma_N^{-1}\boldsymbol{X}\right) \cdot \Gamma_N^{-1} + \Omega_N \Gamma_N \cdot \frac{\partial \boldsymbol{q}}{\partial \boldsymbol{x}}\left(\Gamma_N^{-1}\boldsymbol{X}\right) \cdot \Gamma_N^{-1} + Y, \quad (4.14)$$

where Γ_N is a block diagonal matrix of DFT operators defined by equation (3.64), and Ω_N is a block-diagonal matrix representing the derivative operation (see equation (3.65)). Our goal is to carry out matrix-vector products of the form

$$\boldsymbol{F}'(\boldsymbol{X}) \cdot \boldsymbol{V} = \quad (4.15)$$

$$\Gamma_N \cdot \frac{\partial \boldsymbol{g}}{\partial \boldsymbol{x}}\left(\Gamma_N^{-1}\boldsymbol{X}\right) \cdot \Gamma_N^{-1}\boldsymbol{V} + \Omega_N \Gamma_N \cdot \frac{\partial \boldsymbol{q}}{\partial \boldsymbol{x}}\left(\Gamma_N^{-1}\boldsymbol{X}\right) \cdot \Gamma_N^{-1}\boldsymbol{V} + Y\boldsymbol{V}$$

where $\boldsymbol{V}$ is an arbitrary real $(2H+1)N \times 1$ vector that, like $\boldsymbol{X}$, can be written in block form as

$$\boldsymbol{V} = [\boldsymbol{V}_1, \boldsymbol{V}_2, \ldots, \boldsymbol{V}_N]^T, \quad (4.16)$$

$$\boldsymbol{V}_m = \left[V_{m0}, V_{m1}^R, V_{m1}^I, \ldots, V_{mH}^R, V_{mH}^I\right]^T, \; 1 \le m \le N. \quad (4.17)$$

Consider first the resistive portion of the product. The operation

$$\Gamma_N \cdot \frac{\partial \boldsymbol{g}}{\partial \boldsymbol{x}}\left(\Gamma_N^{-1}\boldsymbol{X}\right) \cdot \Gamma_N^{-1}\boldsymbol{V} \quad (4.18)$$

may be carried out efficiently in three steps. First, $\Gamma_N^{-1}\boldsymbol{V}$ is computed using N FFT operations. Because each block $\partial \boldsymbol{g}_n / \partial \boldsymbol{x}_m$ in

$$\frac{\partial \boldsymbol{g}}{\partial \boldsymbol{x}} = \begin{bmatrix} \frac{\partial \boldsymbol{g}_1}{\partial \boldsymbol{x}_1} & \frac{\partial \boldsymbol{g}_1}{\partial \boldsymbol{x}_2} & \cdots & \frac{\partial \boldsymbol{g}_1}{\partial \boldsymbol{x}_N} \\ \frac{\partial \boldsymbol{g}_2}{\partial \boldsymbol{x}_1} & \frac{\partial \boldsymbol{g}_2}{\partial \boldsymbol{x}_2} & \cdots & \frac{\partial \boldsymbol{g}_2}{\partial \boldsymbol{x}_1} \\ | & | & \backslash & | \\ \frac{\partial \boldsymbol{g}_N}{\partial \boldsymbol{x}_1} & \frac{\partial \boldsymbol{g}_N}{\partial \boldsymbol{x}_2} & \cdots & \frac{\partial \boldsymbol{g}_N}{\partial \boldsymbol{x}_N} \end{bmatrix} \tag{4.19}$$

is strictly diagonal (see (3.68)), the product $\frac{\partial \boldsymbol{g}}{\partial \boldsymbol{x}}\left(\Gamma_N^{-1}\boldsymbol{X}\right)\cdot\Gamma_N^{-1}\boldsymbol{V}$ can then be carried out in $O(H)$ floating point operations. An additional N FFTs complete the steps required to compute (4.18). The corresponding evaluation of the capacitive product

$$\Omega_N\Gamma_N\cdot\frac{\partial \boldsymbol{q}}{\partial \boldsymbol{x}}\left(\Gamma_N^{-1}\boldsymbol{X}\right)\cdot\Gamma_N^{-1}\boldsymbol{V} \tag{4.20}$$

proceeds in an exactly analogous manner, with the additional (cheap) multiplication by the derivative operator Ω_N. Lastly, the product

$$Y\boldsymbol{V} \tag{4.21}$$

can be computed efficiently by noting that each structurally non-zero block of Y is diagonal.

Because the semiconductor device equations are of the form (2.29)-(2.30), there are no nonlinear capacitive terms present within the drift diffusion state equations themselves. Consequently, within the semiconductor device domain, the Jacobian reduces to

$$\boldsymbol{F}'(\boldsymbol{X}) = \frac{\partial \boldsymbol{F}}{\partial \boldsymbol{X}}(\boldsymbol{X}) = \Gamma_N\cdot\frac{\partial \boldsymbol{g}}{\partial \boldsymbol{x}}\left(\Gamma_N^{-1}\boldsymbol{X}\right)\cdot\Gamma_N^{-1} - \mathrm{diag}\,(0, \Omega, \Omega, 0, \Omega, \Omega, \ldots)\,, \tag{4.22}$$

and the corresponding matrix vector product

$$\frac{\partial \boldsymbol{F}}{\partial \boldsymbol{X}}\cdot\boldsymbol{V} = \Gamma_N\cdot\frac{\partial \boldsymbol{g}}{\partial \boldsymbol{x}}\left(\Gamma_N^{-1}\boldsymbol{X}\right)\cdot\Gamma_N^{-1}\boldsymbol{V} - \mathrm{diag}\,(0, \Omega, \Omega, 0, \Omega, \Omega, \ldots)\,\boldsymbol{V} \tag{4.23}$$

contains no nonlinear capacitive multiplies (4.20). Of course, if nonlinear capacitors or linear distributed elements are present outside the semiconductor device domain, then the corresponding products (4.20) and (4.21), respectively, would need to be carried out over the circuit portion of the matrix.

4.3 Preconditioning

The performance of linear iterative solvers can be improved dramatically through the use of preconditioners. Instead of solving the linear system $A\boldsymbol{x} = \boldsymbol{b}$, we instead solve the preconditioned system

$$\left(M_L^{-1} A M_R^{-1} \right) (M_R \boldsymbol{x}) = M_L^{-1} \boldsymbol{b}. \tag{4.24}$$

M_L is called the left-preconditioner, and M_R is referred to as the right-preconditioner. In this work, we restrict ourselves to applying either the left or the right preconditioner, but not both simultaneously.

Preconditioning modifies some aspect of the original matrix (e.g., an improved condition number or a better clustering of eigenvalues) that allows a given iterative linear solver to take fewer iterations. Since the preconditioner must be applied on every iteration, the trade-off must be such that the reduction in iteration count more than offsets the increased work necessary on every iteration. Ideally, a preconditioning matrix M should be a good approximation to the original matrix A, while also being fast and easy to factor.

Many general-purpose preconditioning schemes have been documented in the literature ([49], [50], and references therein). Being general in nature, these turn out to be sub-optimal for preconditioning the harmonic balance Jacobian. As we saw in Section 3.5.4, the HB Jacobian at low distortion levels reduces to a block-diagonal form. It turns out that this matrix is an excellent preconditioner for the harmonic balance problem, and typically continues to perform well even at relatively high distortion levels. In the rest of this section, we will present problem-specific preconditioners for the HB device equations. In addition to the aforementioned block-diagonal preconditioner, we will introduce the so-called sectioned preconditioner for large multi-tone distortion problems, and briefly discuss future work that remains to be done on the problem.

4.3.1 The Block-Diagonal Preconditioner

As was shown in Section 3.5.4, the harmonic balance Jacobian assumes a complex-valued block-diagonal form under the low-level distortion approximation. This block-diagonal matrix is a natural candidate for preconditioning the harmonic balance equations. We can expect such a preconditioner to be outstanding at low power levels, with its effectiveness gradually diminishing as the distortion levels increase. The usefulness of the

preconditioner hinges on its applicability at the power levels of interest in a given application. In practice, this requirement appears to be met in the majority of realistic semiconductor device simulation problems.

$$M_{BD} = \begin{bmatrix} \begin{bmatrix} \alpha_{11}^0 & 0 & 0 & 0 \\ 0 & \alpha_{11}^1 & 0 & 0 \\ 0 & 0 & \alpha_{11}^2 & 0 \\ 0 & 0 & 0 & \alpha_{11}^3 \end{bmatrix} & & & \begin{bmatrix} \alpha_{13}^0 & 0 & 0 & 0 \\ 0 & \alpha_{13}^1 & 0 & 0 \\ 0 & 0 & \alpha_{13}^2 & 0 \\ 0 & 0 & 0 & \alpha_{13}^3 \end{bmatrix} \\ \begin{bmatrix} \alpha_{21}^0 & 0 & 0 & 0 \\ 0 & \alpha_{21}^1 & 0 & 0 \\ 0 & 0 & \alpha_{21}^2 & 0 \\ 0 & 0 & 0 & \alpha_{21}^3 \end{bmatrix} & \begin{bmatrix} \alpha_{22}^0 & 0 & 0 & 0 \\ 0 & \alpha_{22}^1 & 0 & 0 \\ 0 & 0 & \alpha_{22}^2 & 0 \\ 0 & 0 & 0 & \alpha_{22}^3 \end{bmatrix} & \begin{bmatrix} \alpha_{23}^0 & 0 & 0 & 0 \\ 0 & \alpha_{23}^1 & 0 & 0 \\ 0 & 0 & \alpha_{23}^2 & 0 \\ 0 & 0 & 0 & \alpha_{23}^3 \end{bmatrix} & \\ & & & \begin{bmatrix} \alpha_{33}^0 & 0 & 0 & 0 \\ 0 & \alpha_{33}^1 & 0 & 0 \\ 0 & 0 & \alpha_{33}^2 & 0 \\ 0 & 0 & 0 & \alpha_{33}^3 \end{bmatrix} \end{bmatrix}$$

Figure 4.1 An example of the block-diagonal preconditioner matrix structure for *N*=3, *H*=3. Each block within the matrix corresponds to a single Jacobian entry in the time domain Jacobian.

Referring back to equations (3.104) - (3.106), we define α_{nm}^h for notational convenience to be the *h*th diagonal term in the *(n,m)* block of the low-distortion HB Jacobian:

$$\alpha_{nm}^{h} = \frac{\partial F_{nh}}{\partial X_{mh}} = \Lambda_0^{nm} + j\omega_h \Theta_0^{nm} + Y_{nm}(\omega_h) \; . \tag{4.25}$$

The key to fast and efficient factorization of the block-diagonal preconditioning matrix is noting that it can be performed through $H+1$ LU factorizations of sparse $N \times N$ matrices. To illustrate this point, consider an example with $N = 3$ and $H = 3$ (Figure 4.1). By permuting the rows and columns of the preconditioning matrix M_{BD}, it is possible to transform it into the form shown in Figure 4.2. The permutation transforms the

$$\Pi \cdot M_{BD} = \begin{bmatrix} \begin{bmatrix} \alpha_{11}^0 & 0 & \alpha_{13}^0 \\ \alpha_{21}^0 & \alpha_{22}^0 & 0 \\ 0 & 0 & \alpha_{33}^2 \end{bmatrix} & & & \\ & \begin{bmatrix} \alpha_{11}^1 & 0 & \alpha_{13}^1 \\ \alpha_{21}^1 & \alpha_{22}^1 & 0 \\ 0 & 0 & \alpha_{33}^1 \end{bmatrix} & & \\ & & \begin{bmatrix} \alpha_{11}^2 & 0 & \alpha_{13}^2 \\ \alpha_{21}^2 & \alpha_{22}^2 & 0 \\ 0 & 0 & \alpha_{33}^2 \end{bmatrix} & \\ & & & \begin{bmatrix} \alpha_{11}^3 & 0 & \alpha_{13}^3 \\ \alpha_{21}^3 & \alpha_{22}^3 & 0 \\ 0 & 0 & \alpha_{33}^3 \end{bmatrix} \end{bmatrix}$$

Figure 4.2 The block diagonal preconditioner of Figure 4.1 after a permutation operation Π which groups blocks on the basis of frequencies rather than nodes. Each of the H diagonal blocks has dimension $N \times N$ and retains the sparsity structure of the original time domain Jacobian.

matrix into a set of $H + 1$ decoupled $N \times N$ blocks, each having the sparsity pattern of the original Jacobian. That is, the permuted Jacobian takes on the form

$$\Pi \cdot M_{BD} = \begin{bmatrix} J_{\text{ac}}(\omega_0) & & & \\ & J_{\text{ac}}(\omega_1) & & \\ & & \ddots & \\ & & & J_{\text{ac}}(\omega_H) \end{bmatrix}, \tag{4.26}$$

where $J_{\text{ac}}(\omega_h) \in C^{N \times N}$ can be viewed as an AC matrix [57] at harmonic balance frequency ω_h. This is in contrast with the unpermuted structure, which is an $N \times N$ block matrix having the sparsity pattern of the original Jacobian, with each entry being a diagonal block of dimension $(H + 1) \times (H + 1)$.

As readily seen from the preceding paragraph, both the memory requirements and the execution time for employing the block-diagonal preconditioner scale as $O(H)$ with the number of harmonics. Unfortunately, in multi-tone semiconductor device simulation problems, the number of harmonics can still be so large that it is impractical to store the entire preconditioner M_{BD}. Even in two-tone simulation, where the number of harmonics rises as $O(P^2)$ with the truncation order *P*, it is not particularly uncommon to have values of *H* exceeding 100 for high-distortion problems. Given a device structure whose AC Jacobian storage takes 10MB, for example, the storage of M_{BD} would require a gigabyte of RAM for $H = 100$. Clearly, such storage requirements can become prohibitive for large multi-tone simulations.

4.3.2 The Sectioned Preconditioner for Multi-Tone Problems

To overcome the problems posed by block-diagonal preconditioner storage in multi-tone analysis, we note that most multi-tone problems have distinct ‘‘bands’’ of harmonics that are very tightly spaced in frequency. For instance, a common two-tone input signal used for intermodulation distortion analysis is

$$V(t) = A_1 \cos(\Omega_1 t) + A_2 \cos(\Omega_2 t), \tag{4.27}$$

where the tone spacing $\Delta\Omega = \Omega_2 - \Omega_1$ is very small relative to the magnitudes of Ω_1 and Ω_2. Figure 4.3 illustrates the frequency ‘‘bunches’’ or ‘‘bands’’ that result from this type of stimulus.

It is possible to exploit this frequency-grouping phenomenon by noting (Section 2.4.2) that inside the semiconductor device, each state equation has the form

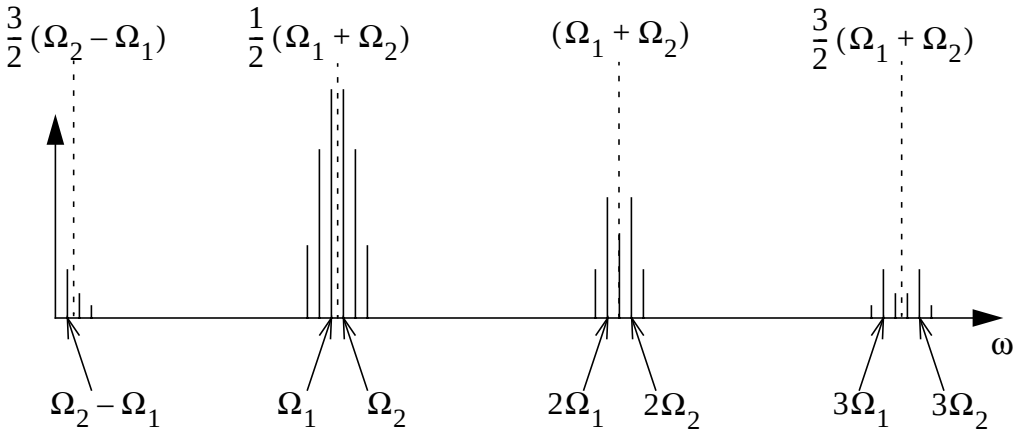

Figure 4.3 An illustration of tightly spaced frequency ‘‘bands’’ that occur when $\Delta\Omega = \Omega_2 - \Omega_1$ is small in a two-tone stimulus. The dashed lines and the frequencies above them indicate the center of each ‘‘band’’ in the spectrum.

$$\delta_{cont}\frac{dx_n}{dt} + g_n(\boldsymbol{x}(t)) - w_n(t) = 0, \tag{4.28}$$

where $1 \le n \le 3K$, and δ_{cont} is zero for the Poisson equations (n=1,4,7, ...) while being unity for the continuity equations (n=2,3,5,6,8,9, ...). Each AC Jacobian matrix $J_{\text{ac}}(\omega_h)$ can be partitioned as

$$J_{\text{ac}}(\omega_h) = \begin{bmatrix} J_{\text{dd}}(\omega_h) & J_{12}(\omega_h) \\ J_{21}(\omega_h) & Y_{\text{ckt}}(\omega_h) \end{bmatrix}, \tag{4.29}$$

where $J_{\text{dd}}(\omega_h) \in C^{3K\times 3K}$ represents the portion of the Jacobian corresponding to the derivative over the semiconductor domain (i.e., derivatives of the semiconductor equations (4.28) with respect to the semiconductor state variables), while $Y_{\text{ckt}}(\omega_h) \in C^{E\times E}$ represents the admittance matrix of the circuitry surrounding the semiconductor device. The remaining two sub-matrices represent the coupling between the circuit and semiconductor domains, taking on the dimensionalities $J_{12}(\omega_h) \in C^{3K\times E}$ and $J_{21}(\omega_h) \in C^{E\times 3K}$.

Because the derivative operator in the time domain equations (4.28) varies linearly with frequency (i.e., $d/dt \to j\omega$), the drift-diffusion sub-matrix $J_{\text{dd}}(\omega_h)$ varies linearly

as ω_h is varied. The circuit sub-matrix $Y_{\text{ckt}}(\omega_h)$, on the other hand, can vary quite rapidly with frequency when, for example, the external circuit network contains high-Q resonant circuitry or filters with sharp transitions. A key observation is that the dimensionality of the circuit sub-matrix is rather small (typically 3×3 or less), while the dimensionality of the drift-diffusion sub-matrix is very large (typically in the thousands). To efficiently factor the $H + 1$ matrices $J_{\text{ac}}(\omega_h)$ in the presence of tightly-spaced bands of harmonics (Figure 4.3), we make the approximation

$$J_{\text{ac}}(\omega_h) \approx \begin{bmatrix} J_{\text{dd}}(\tilde{\omega}_h) & J_{12}(\omega_h) \\ J_{21}(\omega_h) & Y_{\text{ckt}}(\omega_h) \end{bmatrix}, \tag{4.30}$$

where the frequency $\tilde{\omega}_h$ represents the center of the ''band'' containing ω_h. In general, the number of such bands is $P + 1$ — much smaller than $H + 1$, the total number of harmonic balance frequencies. The large drift-diffusion portion of the Jacobian need only be stored at these $P + 1$ band frequencies, while the small circuit portion can be stored at all $H + 1$ frequencies very cheaply. Dramatic reductions in memory usage and improvements in factorization speed result as a consequence.

The actual factorization of (4.30) is accomplished by standard block-LU factorization algorithms. A block system of the form

$$\begin{bmatrix} A_{11} & A_{12} \\ A_{21} & A_{22} \end{bmatrix} \begin{bmatrix} \boldsymbol{x}_1 \\ \boldsymbol{x}_2 \end{bmatrix} = \begin{bmatrix} \boldsymbol{b}_1 \\ \boldsymbol{b}_2 \end{bmatrix} \tag{4.31}$$

can be solved by defining the Schur complement matrix $S = A_{22} - A_{21}A_{11}^{-1}A_{12}$, and then obtaining the solution as

$$\begin{aligned} \boldsymbol{x}_2 &= S^{-1}\left(\boldsymbol{b}_2 - A_{21}A_{11}^{-1}\boldsymbol{b}_1\right) \\ \boldsymbol{x}_1 &= A_{11}^{-1}\boldsymbol{b}_1 - A_{11}^{-1}A_{12}\boldsymbol{x}_2 \end{aligned} \tag{4.32}$$

When applied to solving a sequence of $H + 1$ matrices $J_{\text{ac}}(\omega_h)$, the lion's share of the CPU and memory resources is taken up by the need to factor and store $P + 1$ large sparse matrices $J_{\text{dd}}(\tilde{\omega}_h)$, corresponding to A_{11} in the notation of (4.31) above. The cost for storing and factoring $H + 1$ Schur complement matrices S is negligible in our application, given the small size of the surrounding circuit network.[1] Storage of the $H + 1$ rectangular matrices $A_{11}^{-1}A_{12}$ and $A_{21}A_{11}^{-1}$ is likewise small in comparison.

To illustrate the large advantage to be gained through the use of sectioned preconditioners in multi-tone device-level HB simulation, we offer an example. Consider the high-Q single-BJT mixer configuration (Figure 6.12) which will be more fully discussed in Section 6.3. For good accuracy, the two tone mixer simulation should be done at a diamond truncation order of P=10, which corresponds to H=110 harmonics. Although the BJT mesh is relatively small by semiconductor device simulation standards (704 internal grid points, and N = 2114) the size and density of the Jacobian is such that utilizing non-sectioned preconditioning is prohibitive. The memory reduction obtained by using the sectioned preconditioner is even more significant for devices having larger mesh sizes. Figure 4.4 shows the preconditioner memory usage as a function of the truncation order P for both the sectioned and non-sectioned cases, while Figure 4.5 shows the GMRES convergence behavior in factoring the Jacobian at the solution point. The relatively modest decrease in the linear convergence rate is more than compensated for by the large memory reduction that is obtained. The decrease in preconditioner factorization time typically compensates the slight increase in the number of linear iterations. For linear solutions in the context of Newton's method, relative residual accuracies tighter than 10^{-3} are rarely called for, and Figure 4.5 shows the convergence behavior past this point merely for the sake of completeness.

1. External linear networks with large numbers of internal circuit nodes are collapsed into much smaller admittance matrices, having a dimensionality corresponding to the number of transistor terminals connected to the linear network.

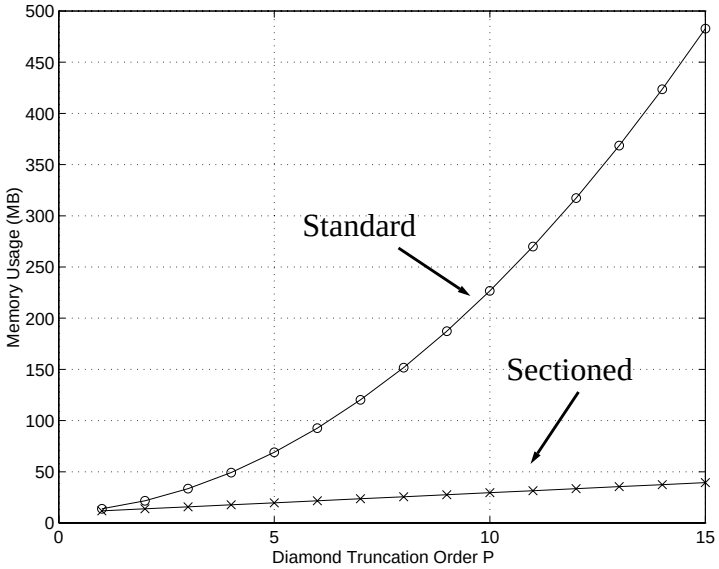

Figure 4.4 Memory usage comparison between the sectioned and non-sectioned preconditioners for the single-BJT mixer example.

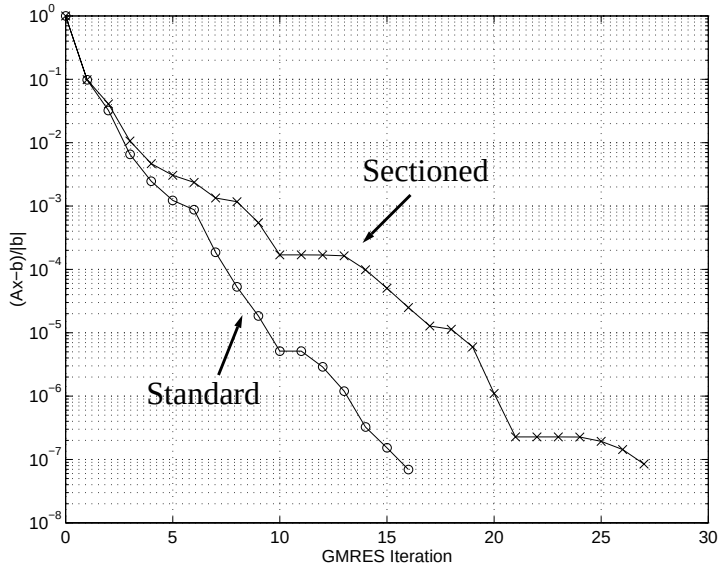

Figure 4.5 Convergence rate comparison between the sectioned and non-sectioned preconditioners for the single-BJT mixer example.

4.3.3 Other Preconditioners

The preconditioners discussed in the preceding sections are effective for a wide range of harmonic balance device simulation problems. There are two possible paths to follow for further improving their performance. In the low distortion regime, special-purpose matrix solvers geared specifically to the form of the drift-diffusion equations can be employed to reduce the memory requirements necessary for preconditioner storage [58]. In practice, however, because the sectioned preconditioner storage requirements are already relatively low, this approach is truly useful only in the case where the spectrum is such that a very large number of sections exist. This does not typically occur in semiconductor device simulation.

A far more useful improvement to the preconditioner is to incorporate additional off-diagonal elements in the harmonic balance Jacobian blocks. This is crucial to solving some highly nonlinear problems — indeed, as Section 4.6 will discuss, the block-diagonal preconditioner is typically adequate only up to gain compression levels of a few dB. Block-oriented incomplete-factorization solvers based on the techniques presented in Section 3.5.3 have been developed to incorporate some off-diagonal Jacobian stripes on a block-by-block basis [58], and have been used with some success in the context of circuit and small device simulation problems. However, because of the large Jacobian sizes and densities encountered in mainstream semiconductor device simulation examples, the methods developed by us to date have thus far fallen short of being practical. Clearly, more work is called for in this area.

4.4 Further Memory Reduction Strategies

4.4.1 Approximate Compact Spectral Storage

We saw in Section 4.2 that carrying out matrix-vector products involving the HB Jacobian requires storing $2S$ samples

$$\frac{\partial g_n}{\partial x_m}(t_s)\ ,\ 0 \le s \le 2S-1 \tag{4.33}$$

at the structurally non-zero Jacobian entries *(n, m)* over the semiconductor device domain. For large numbers of harmonics *H*, this storage cost can become quite substantial. As an example, typical ‘‘medium-size’’ meshes used in this work contain about 50,000 non-zero

Jacobian entries[1] prior to factorization. For a two-tone harmonic balance analysis at 100 frequencies, the memory cost of storing the samples (4.33) is almost 80 MB. For an analysis at 200 frequencies, the cost is almost 160 MB. Although this cost is bearable given the memory capacity of modern workstations, it nevertheless makes sense to examine algorithms for reducing the aforementioned memory usage.

Consider the set of samples

$$\lambda_s = \frac{\partial g_n}{\partial x_m}(t_s)\ ,\ 0 \le s \le 2S-1 \tag{4.34}$$

along with their Fourier transform

$$\Lambda_h = \sum_{s=0}^{2S-1} \lambda_s \exp\left(\frac{2\pi j}{2S+2} \cdot hs\right),\ 0 \le h \le S\,. \tag{4.35}$$

Ordinarily, the set of all $2S$ time domain samples λ_s is stored. The key to reducing storage requirements is to note that the spectrum Λ_h of these samples is quite sparse for most Jacobian entries *(n, m)*. This sparsity comes about because of the relatively low levels of harmonic distortion in many regions within the device. By Fourier transforming the samples (4.34), discarding those Fourier coefficients that fall below a certain threshold, and storing the remaining coefficients, an accurate approximation of the original Jacobian is retained. To perform matrix-vector multiplications during the GMRES process, the stored spectral coefficients are inverse-FFT'ed into the time domain element-by-element, at which point the algorithms of Section 4.2 can be applied.

An important consideration in implementing the above memory reduction scheme is determining the proper threshold for sparsifying the spectral samples Λ_h. Choosing too high a threshold will result in an inaccurate Jacobian, and thus a degradation in the rate of convergence. Choosing too low a value will result in very little sparsification of the spectrum, thus negating the benefits of the approach. For this work, the following simple heuristic has shown itself to be effective. Given a spectrum Λ_h, the threshold $\varepsilon_{\text{thresh}}$ is chosen to be

1. In actuality, many industrial users employ much larger mesh sizes.

$$\varepsilon_{\text{thresh}} = \max\left(\varepsilon_{\min}, \varepsilon_{\text{rel}} \frac{\Lambda_0 + \max\limits_{0 \le h \le H} \Lambda_h}{2}\right) \tag{4.36}$$

and all values Λ_h such that $\Lambda_h \le \varepsilon_{\text{thresh}}$ are discarded and effectively approximated as zero for the matrix-vector multiplies to follow. The purpose of the ε_{rel} parameter is to discard spectral components that fall below a certain ‘‘dynamic range.’’ For instance, typical values of 10^{-4} to 10^{-5} would ensure that spectral components that are 80-100 dB down are viewed as being insignificant to the accurate representation of the time domain waveform samples λ_s. The $\varepsilon_{\min}$ parameter ensures that spectral components that fall below a certain absolute value (say, 10^{-20}) are discarded as ‘‘noise’’ which is unimportant to the overall Jacobian representation. For example, a set of spectral components that range in value from 10^{-25} to 10^{-27} would all be included if only the relative dynamic range criterion was used, even though the Jacobian entry could very accurately be represented by zero for typical device problems.

An additional consideration in invoking the compact spectral storage option is the penalty in CPU time for carrying out the inverse FFT operation for each Jacobian entry during each matrix-vector multiplication. As shown in Section 4.2, $2N$ FFT operations[1] are necessary for each Jacobian-vector product when standard (time domain) storage is used. When spectral representations are utilized, however, an additional inverse FFT must be performed during each such Jacobian-vector product for every non-zero Jacobian entry.

Before concluding the section, we point out that a very similar memory reduction scheme was proposed in the context of circuit simulation by Long et al. [41]. The techniques presented above were developed independently, and implemented in our simulator before publication of the aforementioned work.

4.4.2 Approximate GMRES Vector Storage

Another potentially large source of memory consumption is the storage of the Krylov subspace basis vectors (for Gram-Schmidt GMRES) or Householder reflection vectors (for Householder-Arnoldi GMRES). For a simulation problem having a million unknowns, each such vector would occupy 8 MB of RAM if standard double-precision

1. Actually, N FFT operations and N inverse FFTs.

storage was used. Thus, for a restart value of 10, about 80 MB of additional storage would be required. While this may not seem like much relative to other storage requirements inherent in HB device simulation, it is nevertheless significant.

The memory usage associated with the GMRES vectors can be reduced by following an approach similar to the one taken in the previous section [41]. It turns out that the GMRES vectors in both the Gram-Schmidt and Householder variants are numerically sparse, and that convergence rates are not significantly affected by discarding entries below a certain threshold. Furthermore, Long et al. [41] have observed that the vectors can be stored in single precision without adversely affecting the quality of the linear solve.

The GMRES sparsification option was implemented in our simulator. We have noticed, however, that for some ill-conditioned semiconductor device simulation problems[1] the threshold must be set far lower than the value of 10^{-6} suggested in [41]. Consequently, we've made the decision that the benefits gained are not worth the extra heuristics inherent in having a user-specified threshold parameter. While the option is available, we discourage its use until such time as the code is improved to remove the source of potential ill-conditioning. Storing the GMRES vectors in single-precision format does seem to work well even in the ill-conditioned case, and use of this option (without sparsification) is encouraged.

4.4.3 Impact of Memory Reduction Strategies on Performance

Given the size and density of the device-level Jacobian, using the reduced preconditioner of Section 4.3.2 is crucial for efficient analysis of large two-tone problems. However, employing the additional memory reduction techniques of the preceding two sections can be quite beneficial as well. We quantify these choices by applying them to the high-Q single-BJT mixer example of Section 6.3 for an analysis at $H = 110$ harmonics, which corresponds to an HB problem with 467,194 unknowns.

Table 4.1 shows simulation results when the various memory reduction options are turned on or off. The Jacobian memory reduction utilized an ε_{rel} of 10^{-4}. The GMRES memory reduction option simply switched between single and double precision storage of the GMRES vectors, without actually sparsifying them. From the results below, it is

1. The ill-conditioning can arise from the small resistors that some mixed-level circuit/device PISCES variants insert in series with each terminal.

Sectioned precond.	Jacobian memory reduction	GMRES single prec. storage	Memory Usage	Simulation Time
yes	yes	yes	159 MB	95 min. 27 sec.
yes	yes	no	179 MB	91 min. 45 sec.
yes	no	yes	199 MB	64 min. 54 sec.
yes	no	no	219 MB	64 min. 11 sec.
no	no	no	413 MB	70 min. 50 sec.

Table 4.1 A comparison of simulator performance under various memory reduction options.

apparent that usage of the sectioned preconditioner yields the biggest memory savings (a full 194 MB), while also speeding up the simulation by about 10%. (The computer used for the benchmark had 900MB of RAM; the speed-up obtained would be much more significant on machines with, say, only 250MB of RAM available.) Using single-precision GMRES storage saves an additional 20MB, without any noticeable loss in speed. Invoking compact Jacobian spectral storage saves an additional 20MB, albeit at a 50% performance penalty.

We point out that slightly over 40MB of memory is used by the static arrays in the Fortran-based core PISCES code. The harmonic balance module itself allocates anywhere from under 119MB with all memory-saving options turned on to 373MB with all options disabled. Before concluding this section, we mention that the memory reduction due to the sectioned preconditioner is more dramatic for larger devices, and that the reductions seen in Jacobian memory usage are more significant as the number of harmonics is increased and/or as the input power level is decreased. In this particular example, the BJT has no source resistance, and is driven by a local oscillator sinusoid with a 0.7V DC bias and a 0.15V amplitude.

4.5 Iterative Linear Solvers in the Newton Loop

Recall that the lth iteration ($l \geq 1$) of Newton-Raphson applied to (3.60) is

$$\boldsymbol{X}^{(l)} = \boldsymbol{X}^{(l-1)} + \Delta\boldsymbol{X}^{(l)}, \tag{4.37}$$

where $\Delta \boldsymbol{X}^{(l)}$ is the solution of the linear system

$$\boldsymbol{F}'\left(\boldsymbol{X}^{(l-1)}\right) \cdot \Delta \boldsymbol{X}^{(l)} = -\boldsymbol{F}\left(\boldsymbol{X}^{(l-1)}\right). \tag{4.38}$$

If the equation is solved to infinite precision, and if the nonlinear system $\boldsymbol{F}(\boldsymbol{X}) = \boldsymbol{0}$ satisfies certain (commonly encountered in practice) conditions [24], then the convergence is quadratic for initial guesses which are arbitrarily close to the solution. In finite-precision floating point arithmetic, however, there will always be some error in solving the linear Newton update equation. That is, the absolute and relative errors

$$\varepsilon_{\text{abs}} = \left\| \boldsymbol{F}'\left(\boldsymbol{X}^{(l-1)}\right) \cdot \Delta \boldsymbol{X}^{(l)} + \boldsymbol{F}\left(\boldsymbol{X}^{(l-1)}\right) \right\| \tag{4.39}$$

$$\varepsilon_{\text{rel}} = \frac{\varepsilon_{\text{abs}}}{\left\| \boldsymbol{F}\left(\boldsymbol{X}^{(l-1)}\right) \right\|} = \frac{\left\| \boldsymbol{F}'\left(\boldsymbol{X}^{(l-1)}\right) \cdot \Delta \boldsymbol{X}^{(l)} + \boldsymbol{F}\left(\boldsymbol{X}^{(l-1)}\right) \right\|}{\left\| \boldsymbol{F}\left(\boldsymbol{X}^{(l-1)}\right) \right\|} \tag{4.40}$$

will in practice always be non-zero, regardless of whether direct or iterative methods are used to solve the linear system.

Given that some level of error during the linear solve is unavoidable, it is prudent to study its effect on nonlinear convergence regardless of whether direct or iterative methods are employed. With iterative methods, however, the subject becomes particularly significant, because there is an important trade-off to be made. On the one hand, a particular implementation could choose to take many iterations during the linear stage, solving (4.38) to a high degree of accuracy in the hope of minimizing the number of nonlinear steps (4.37). On the other hand, it is conceivable that such an implementation would ‘‘over-solve’’ the linear system — that is, solve it to a much higher degree of accuracy at every nonlinear step than is necessary to assure adequately sharp nonlinear convergence. Because the linear solution time often dominates the overall CPU time, oversolving can lead to serious inefficiency. Consequently, Newton methods relying on iterative linear solvers make use of a sequence of ‘‘forcing terms’’ η_l satisfying

$$0 < \eta_l < 1 . \tag{4.41}$$

During the *l*th Newton-Raphson step, the linear problem is solved to a relative tolerance of $\varepsilon_{\text{rel}}^{(l)} \leq \eta_l$ — i.e.,

$$\left\| \boldsymbol{F}'\left(\boldsymbol{X}^{(l-1)}\right) \cdot \Delta \boldsymbol{X}^{(l)} + \boldsymbol{F}\left(\boldsymbol{X}^{(l-1)}\right) \right\| \leq \eta_l \cdot \left\| \boldsymbol{F}\left(\boldsymbol{X}^{(l-1)}\right) \right\| . \tag{4.42}$$

Ideally, the sequence of forcing terms must be chosen to yield a good compromise between spending an excessive amount of time in the linear phase and spending an

excessive amount of time by taking too many nonlinear Newton steps. Furthermore, a critically important question arises: what level of accuracy is necessary in the linear solution step to prevent flat-out divergence of the Newton-Raphson process?

To lay the groundwork for further discussion, and to partially answer the preceding question, a pair of theorems from [52] are introduced. Suppose that $\boldsymbol{X}^*$ is the solution point[1] (i.e., $\boldsymbol{F}(\boldsymbol{X}^*) = 0$), and that the initial iterate is $\boldsymbol{X}^{(0)}$ very close to the solution $\boldsymbol{X}^*$. Define the error at the lth iteration as

$$e_l = \left\| \boldsymbol{X}^{(l)} - \boldsymbol{X}^* \right\|. \tag{4.43}$$

Then, under assumptions which are in practice met in our work,

$$e_l \leq K\left(e_{l-1} + \varepsilon_{\text{rel}}^{(l)} \right) e_{l-1} \tag{4.44}$$

for some positive constant K. We immediately see that for the case where $\varepsilon_{\text{rel}} = 0$ (i.e., no error in the linear solve),

$$e_l \leq K e_{l-1}^2, \tag{4.45}$$

and so the convergence is quadratic. For a finite value of $\varepsilon_{\text{rel}}^{(l)}$, linear (or possibly superlinear) convergence will be obtained if the condition $K\left(e_{l-1} + \varepsilon_{\text{rel}}^{(l)} \right) < 1$ is satisfied. In general, however, even linear convergence cannot be assured using the Euclidean norm of (4.43). [51]

Somewhat surprisingly, however, the constraint (4.41) does guarantee at least linear convergence if the error is monitored in the weighted norm

$$e_l^* = \left\| \boldsymbol{X}^{(l)} - \boldsymbol{X}^* \right\|_* = \left\| \boldsymbol{F}'(\boldsymbol{X}^*) \cdot \left(\boldsymbol{X}^{(l)} - \boldsymbol{X}^* \right) \right\|, \tag{4.46}$$

and if the forcing terms don't accumulate at unity (i.e., if there exists $\eta_{\max} < 1$ such that $0 < \eta_l < \eta_{\max}$). This result is significant because it provides assurance that for initial guesses close enough to the solution, convergence will be obtained even for a very ''loose'' sequence of forcing terms. Although quadratic convergence of the outer Newton loop may be lost, linear convergence in the weighted norm will always be obtained. Furthermore, because

$$\boldsymbol{F}\left(\boldsymbol{X}^{(l)} \right) \approx \boldsymbol{F}'(\boldsymbol{X}^*) \cdot \left(\boldsymbol{X}^{(l)} - \boldsymbol{X}^* \right) \tag{4.47}$$

1. In the context of this discussion, the '*' symbol should not be confused with conjugation.

by Taylor's theorem, we see that linear convergence of the error in the weighted norm (4.46) is equivalent to linear convergence of the residual in the Euclidean norm $\left\| \boldsymbol{F}\left(\boldsymbol{X}^{(l)} \right) \right\|$.

In practical implementations of the inexact Newton method, the forcing sequence η_l is chosen such that the tolerance is relatively loose during the initial portion of the Newton solve, where convergence is typically slow. As the Newton method proceeds, the tolerance is tightened as a function of the decrease in the nonlinear residual. Ideally, the forcing terms will be small enough to ensure quadratic convergence toward the latter part of the iterative process. In our work, we use a variant of the technique presented in [51][52]. Initially, a forcing term of $\eta_0 = \eta_{\max} < 1$ is used. Subsequently, the forcing sequence is adjusted according to the formula

$$\eta_l = \max\left(\eta_{\min}, \min\left(\frac{\gamma \left\| \boldsymbol{F}\left(\boldsymbol{X}^{(l)} \right) \right\|^2}{\left\| \boldsymbol{F}\left(\boldsymbol{X}^{(l-1)} \right) \right\|^2}, \eta_{\max} \right) \right). \tag{4.48}$$

The constants $0 < \eta_{\min} < \eta_{\max} < 1$ are chosen to bound the forcing sequence and prevent under- or over-solving. In between these upper and lower bounds, the equation (4.48) attempts to reduce the forcing terms gradually as the Newton residual drops during the nonlinear solution process. Typical constants used by the simulator are $\eta_{\min} = 10^{-4}$, $\eta_{\max} = 0.1$, and $\gamma = 0.9$.

4.6 Convergence Issues

The harmonic balance algorithm is very fast, efficient, and robust for problems with low input power levels. As the power levels are gradually increased, harmonic balance requires more memory (since the number of harmonics due to distortion increases) and more Newton iterations to reach convergence.[1] A much more serious problem that occurs when Krylov subspace methods are employed is the appearance of strong off-diagonal elements within the HB Jacobian blocks. Because these are not accounted for by the block-diagonal preconditioners of Section 4.3, GMRES converges at a slower and slower

1. Source stepping or arc-length continuation must be used, with RF input power as the continuation parameter.

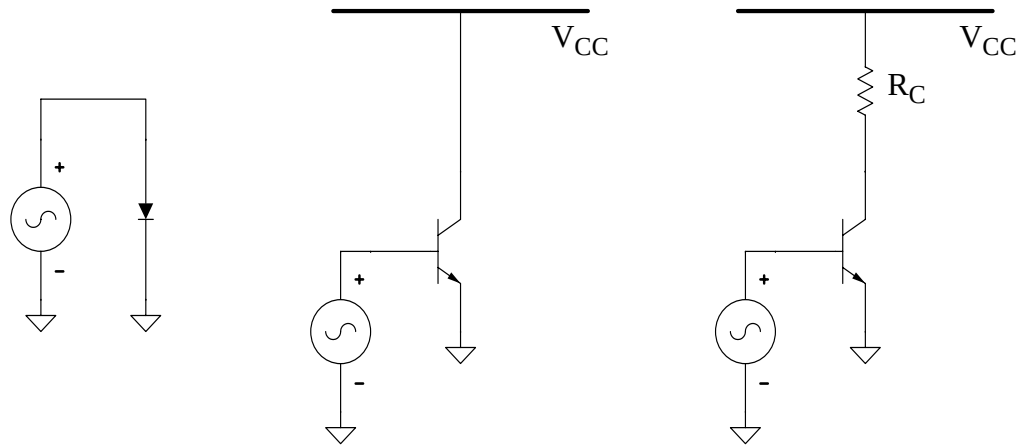

Figure 4.6 Three device configurations to illustrate when harmonic balance convergence problems can occur. The two leftmost configurations will not exhibit convergence difficulties. The rightmost configuration may, if the input RF power is large.

rate as the level of distortion is increased. Eventually, convergence can become so slow that the code cannot complete the simulation within a practical amount of time.

The discussion of the preceding paragraph would seem to imply that convergence difficulties will plague any harmonic balance device simulation when the nonlinear device is driven hard enough. Somewhat surprisingly, however, this is not the case. We have found, for example, that diode simulations can be carried out to absurdly high levels of rectification without any convergence problems. Similarly, simulations of bipolar transistors that don't saturate[1] are likewise easily handled for extremely high values of RF input power. Unfortunately, all practical transistor configurations are subject to some loading on the collector. If this load is such that the RF voltage swing on the collector node causes the device to enter saturation during some portion of the period, convergence degradation can result.

Consider the three device configurations in Figure 4.6. As discussed in the preceding paragraph, neither the diode circuit (left) nor the non-saturating BJT arrangement (center)

1. Or, equivalently, MOSFETs that don't enter the triode region.

will have any convergence problems, even for very large driving voltages. As an example, we show the simulated response of a diode structure to an input sinusoid of the form

$$V = (0.8V)\sin(\omega t) \tag{4.49}$$

in Figure 4.7 below. The harmonic balance code had absolutely no problems converging

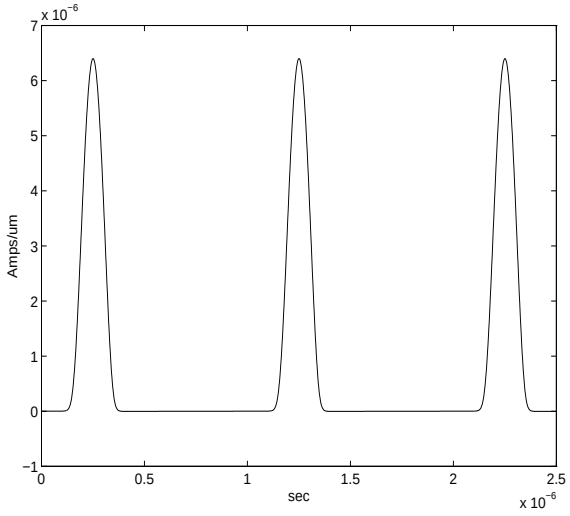

Figure 4.7 Steady-state time domain diode current in response to a 0.8V driving sinusoid. The results were computed with the harmonic balance PISCES device simulator.

on this extremely nonlinear example. Exactly the same type of robust convergence behavior is observed when bipolar transistors are driven by large-amplitude RF signals, so long as the collector voltage is fixed and the device is not allowed to saturate.

In practical amplifier configurations, the collector is attached to a non-negligible load. For instance, consider the rightmost circuit in Figure 4.6. It turns out that for situations such as this, the Krylov solver in the harmonic balance code *will* experience convergence degradation as the amplifier is driven into compression. As the input RF amplitude is increased, the swing of the collector voltage will increase as well. Eventually, the BJT will be in saturation for a portion of the period. We have found that the GMRES convergence will degrade as the amplifier exhibits more and more gain compression. Typically, the harmonic balance code will simulate to the 3dB compression point relatively easily, and have some difficulty beyond that point. We have, however, simulated gain compression

levels up to about 10dB in some industrial-grade examples (see Figure 6.14 on page 125, for instance). The various convergence issues are not yet fully understood by us; in particular, it is not entirely clear why some strong nonlinearities (such as diode junctions) can be simulated so easily, while others (amplifiers in compression) seem to cause quite a bit more difficulty. Clearly, further study is called for here.

4.7 Summary

The algorithms presented in this chapter make device-level harmonic balance analysis feasible on standard desktop workstations. GMRES, a Krylov subspace solution technique for linear systems, is used to solve the large matrix problems arising from Newton-Raphson iteration. Techniques for compact storage of the harmonic balance Jacobian are discussed, and algorithms for efficient computation of matrix-vector products involving the HB Jacobian are presented. After discussing standard block-diagonal preconditioners already used in circuit-level harmonic balance, the chapter proceeds to develop one of the main contributions of this thesis — the sectioned preconditioner, which is crucial to the efficient simulation of multi-tone device-level HB problems. Further memory reduction techniques based on frequency domain sparsification of the HB Jacobian samples are examined, along with sparsification and single-precision storage of the GMRES vectors.

After a brief overview of some heuristics associated with inexact Newton methods, a few comments on simulator convergence issues are given. In general, diode nonlinearities and forward-active BJTs simulate very well, even for extremely large levels of distortion. Amplifiers in compression, partially saturated BJTs, and MOSFETs whose operation takes them into the triode region have more convergence difficulties for large input powers. Gain compression levels of several dB are readily simulated, and although some examples continue to converge well for gain compression levels up to 10dB, others begin to have convergence difficulties when the 3dB compression point is reached.

Chapter 5

Competing Approaches

The preceding chapters have provided a detailed description of the harmonic balance algorithm, with most of the emphasis placed on Krylov subspace solution methods used in conjunction with the Newton-Raphson technique. In this chapter, we provide an overview of two competing simulation algorithms that are useful for analyzing nonlinear systems under large-signal drive. Although both algorithms have certain advantages over harmonic balance, they also have weaknesses which make them less suitable for many device-level simulation problems.

The first algorithm considered is circuit envelope, developed by Sharrit [59][60] for analyzing nonlinear systems in the presence of modulated sinusoids. Unlike harmonic balance, envelope is not a steady state analysis. Rather, it captures transient behavior in the presence of modulated carrier signals by expressing the state vector as a sum of time-varying phasors. It is ideal for simulation of phase lock loops, automatic gain control circuits, and digital communication systems. At the single-device (physics-based) level, however, its application is somewhat more limited.

The second competing algorithm discussed in this chapter is the matrix-implicit shooting method developed by Telichevesky, Kundert, et al. [65]. The shooting method is a steady state time domain simulation technique that, unlike harmonic balance, is very robust even in the presence of extremely nonlinear behavior. Its chief disadvantages relative to harmonic balance are its inability to economically handle true large signal

multi-tone inputs at widely spaced or incommensurate frequencies, along with its difficulties in handling convolution-based distributed linear components.

The chapter concludes with a comparison of the strengths and weaknesses of transient, harmonic balance, circuit envelope, and shooting method algorithms. We point out here that in the course of this work only harmonic balance was actually implemented in the PISCES-II device simulator.[1] Consequently, our comments regarding the other algorithms are of necessity somewhat speculative in nature, and should in the future be verified in actual implementations.

5.1 Envelope Simulation

The harmonic balance algorithm is based on representing the state variables as sums of sinusoidal basis functions. A direct consequence of this fact is that harmonic balance may be a sub-optimal algorithm for systems whose response is not most naturally expressed as a sum of sinusoids. For example, in applications where digitally modulated signals are present, the response vector is perhaps more effectively expanded in basis functions of the form

$$x(t) = \sum_h X_h(t) \exp(j\omega_h t) , \tag{5.1}$$

where the *envelopes* $X_h(t)$ represent modulation on top of ‘‘carrier’’ sinusoids at frequencies ω_h. Furthermore, in some situations, the designer may be interested in capturing transient behavior of systems containing modulated carriers.[2] Because harmonic balance is inherently a steady state simulation technique, it is by definition unsuitable for such applications. In this section, we present a brief overview of the circuit envelope simulation algorithm [59][60] developed to handle such problems efficiently.

5.1.1 Envelope Representation in the Presence of Nonlinearities

Before proceeding with a description of the circuit envelope algorithm, we first analyze what happens when a signal with an envelope representation is processed by an

1. The simulator already had standard transient analysis capability, however.

2. Examples of such application areas include analysis of automatic gain control circuits and simulation of capture transients in phase-locked loops.

algebraic nonlinearity. This approach is consistent with our previous treatment of harmonic balance, and is taken here to simplify subsequent algorithmic development. For notational convenience, the carrier frequencies ω_h will be assumed to all be multiples of a single fundamental ω_0, and only a single-variable (i.e., single-node) system will be considered. Extensions to non-harmonically related frequencies and multi-node systems are straightforward given the algorithms developed in Chapter 3.

Recall that Section 3.3 presented transform algorithms for obtaining the waveform generated by quasiperiodic signals passing through purely resistive (i.e., algebraic) nonlinearities. Following along the same lines, consider the waveform that results when the envelope-based signal

$$x(t) = \Re e\left\{ \sum_{h=0}^{H} X_h(t) \exp(j\omega_h t) \right\} \tag{5.2}$$

is processed by some well-behaved algebraic nonlinearity $g(x(t))$. Assuming that the envelope coefficients $\boldsymbol{X}(t) = [X_0(t), X_1(t), \ldots, X_H(t)]^T$ are known, let us define the function

$$\tilde{x}(\boldsymbol{X}(\tau_1), \tau_2) = \Re e\left\{ \sum_{h=0}^{H} X_h(\tau_1) \exp(j\omega_h \tau_2) \right\} \tag{5.3}$$

and note that $x(t) = \tilde{x}(\boldsymbol{X}(t), t)$. Now consider the function $g(\tilde{x}(\boldsymbol{X}(\tau_1), \tau_2))$. If τ_1 is held fixed while samples are taken along the τ_2 axis, we can compute Fourier coefficients

$$G_h(\boldsymbol{X}(\tau_1)) = \frac{1}{2H+2} \sum_{s=0}^{2H+1} g\left(\tilde{x}\left(\boldsymbol{X}(\tau_1), \frac{2\pi hs}{2H+2} \right) \right) \exp\left(j\frac{2\pi hs}{2H+2} \right) \tag{5.4}$$

such that, by the Fourier Transform Theorem, the relationship

$$g(\tilde{x}(\boldsymbol{X}(\tau_1), \tau_2)) \approx \Re e\left\{ \sum_{h=0}^{H} G_h(\boldsymbol{X}(\tau_1)) \exp(j\omega_h \tau_2) \right\} \tag{5.5}$$

is satisfied. The approximate equality above is due only to aliasing, and becomes exact if the order H is large enough to make aliasing effects insignificant. By setting $\tau_1 = \tau_2 = t$, recalling that $x(t) = \tilde{x}(\boldsymbol{X}(t), t)$, and ignoring aliasing, we see that (5.4) - (5.5) imply that $g(x(t)) = g(\tilde{x}(\boldsymbol{X}(t), t))$ can be expressed in the envelope representation as

$$g(x(t)) = \Re e\left\{ \sum_{h=0}^{H} G_h(\boldsymbol{X}(t)) \exp(j\omega_h t) \right\}, \tag{5.6}$$

where the envelope functions are computed by the transform

$$G_h(\boldsymbol{X}(t)) = \frac{1}{2H+2} \sum_{s=0}^{2H+1} g\left(\tilde{x}\left(\boldsymbol{X}(t), \frac{2\pi hs}{2H+2} \right) \right) \exp\left(j\frac{2\pi hs}{2H+2} \right). \tag{5.7}$$

To recap and clarify the treatment in this section, the key points are summarized in this final paragraph. Suppose we are given a waveform

$$x(t) = \Re e\left\{ \sum_{h=0}^{H} X_h(t) \exp(j\omega_h t) \right\} \tag{5.8}$$

with known envelope coefficient functions $\boldsymbol{X}(t) = [X_0(t), X_1(t), \ldots, X_H(t)]^T$ and carrier frequencies ω_h. When this waveform is processed by some algebraic nonlinearity $g(x(t))$, the resulting waveform can be expressed in the envelope representation (5.6). Furthermore, the time-varying envelope coefficients $\boldsymbol{G}(\boldsymbol{X}(t))$ can be computed at each time instance through the Fourier Transform relation (5.7).

5.1.2 The Circuit Envelope Algorithm

Having established the behavior of envelope-based signals in the presence of algebraic nonlinearities, we now present the circuit envelope algorithm for solving the prototype circuit/device equation

$$g(x(t)) + \frac{d}{dt} q(x(t)) = w(t) \tag{5.9}$$

when $w(t)$ is a stimulus of the form

$$w(t) = \sum_{h} W_h(t) \exp(j\omega_h t) . \tag{5.10}$$

When the state vector $x(t)$ is expanded into the envelope representation (5.2), both $g(x(t))$ and $q(x(t))$ assume the envelope form (5.6) by the discussion of the preceding section. Inserting this into the constitutive equation (5.9) results in

$$\sum_{h} G_h(\boldsymbol{X}(t)) \exp(j\omega_h t) + \frac{d}{dt} \sum_{h} Q_h(\boldsymbol{X}(t)) \exp(j\omega_h t) = \sum_{h} W_h(t) \exp(j\omega_h t) \tag{5.11}$$

or equivalently

$$\sum_h [\, G_h(\boldsymbol{X}(t)) + Q_h'(\boldsymbol{X}(t)) + j\omega_h Q_h(\boldsymbol{X}(t)) - W_h(t) \,] \exp(j\omega_h t) = 0. \quad (5.12)$$

For notational simplicity, define $\boldsymbol{G}(\boldsymbol{X}(t)) = [\, G_0(\boldsymbol{X}(t)), \ldots, G_H(\boldsymbol{X}(t)) \,]^T$, with analogous vector definitions for $\boldsymbol{Q}(\boldsymbol{X}(t))$ and $\boldsymbol{W}(t)$. To solve the system (5.12), we must thus solve the system of ordinary differential equations

$$\boldsymbol{G}(\boldsymbol{X}(t)) + \boldsymbol{Q}'(\boldsymbol{X}(t)) + \Omega \boldsymbol{Q}(\boldsymbol{X}(t)) = \boldsymbol{W}(t). \quad (5.13)$$

for the waveform envelopes $\boldsymbol{X}(t)$. As in ordinary transient analysis, the system of ODEs can be readily converted into a system of algebraic equations by applying finite-difference methods. For example, using the Backward Euler method, we obtain

$$\boldsymbol{G}(\boldsymbol{X}(t_k)) + \frac{\boldsymbol{Q}(\boldsymbol{X}(t_k)) - \boldsymbol{Q}(\boldsymbol{X}(t_{k-1}))}{t_k - t_{k-1}} + \Omega \boldsymbol{Q}(\boldsymbol{X}(t_k)) = \boldsymbol{W}(t_k). \quad (5.14)$$

This is a system of harmonic balance equations which can be solved for $\boldsymbol{X}(t_k)$ at every time step t_k. The inherent advantage of the envelope approach is that the time step spacing $t_k - t_{k-1}$ need only be small enough to resolve the envelopes around each carrier, without regard to the actual values of the carrier frequencies themselves. The harmonic balance algorithms developed in the preceding two chapters apply directly to the solution of (5.14).

5.1.3 Application to the Semiconductor Device Simulation Problem

Semiconductor device designers who develop transistors for power amplifier applications are typically most interested in the amplifier's response to modulated signals. In particular, as adoption of digital modulation schemes for wireless communication systems gains momentum, there is an increasing need to simulate the amplifiers using realistic digitally modulated inputs. While the single- and multi-tone harmonic balance capability presented in this work can be quite useful for semiconductor device design, it is not truly applicable to the computation of several important quantities that arise in the context of digital modulation. For example, a key concern is the spectral regrowth caused by amplifier nonlinearities. The adjacent channel power ratio (ACPR) [61] is a quantity which measures the extent to which distortion causes the spectral power in one channel to spill over into another. As we discuss below, this computation is currently beyond the reach of the harmonic balance device simulation algorithms presented in this work.

Let’s assume a (relatively typical) modulation format with a 1 GHz carrier and 30 kHz channel spacing. It has been shown [61] that a spectral resolution of roughly 50 Hz is desirable for accurate computation of ACPR. To include the ratios for both the lower and upper channels, a total simulation bandwidth of 90 kHz (3 channels) is required around the carrier. Thus, 18,000 spectral lines per carrier harmonic are necessary. If compact transistor models were to be used, such simulations could be readily carried out with Krylov-based harmonic balance algorithms. In physics-based semiconductor device simulation, however, where time domain problem sizes typically range from 3000 to 10,000 unknowns, attempting a direct harmonic balance analysis would result in a problem size of hundreds of millions, if not billions, of equations. Simply storing the solution vector or the right hand side residual would require Gigabytes of RAM. Clearly, such an approach would not be practical.

The envelope analysis technique could in theory be applied to the above problem, though in practice the simulation times would be prohibitive. Because there are 18,000 spectral lines within the ‘‘envelope’’ around each carrier frequency, at least 18,000 time samples would need to be taken. Assuming that the harmonic balance analysis at each time step takes about 5 minutes[1] (the number of HB harmonics would now be relatively small), it would take roughly 63 days to compute a solution, even though the memory requirements would be quite modest. Without resorting to supercomputers or parallel machines, solution of such problems is beyond the scope of current capabilities.

5.2 The Shooting Method

Recall that three key strengths of harmonic balance relative to standard time domain methods are its ability to directly capture a system’s steady state response, its insensitivity to spectral tone input spacings, and its efficient handling of distributed linear components. A weakness of harmonic balance relative to time domain methods is its potentially poorer handling of strongly nonlinear responses that are difficult to represent efficiently with sinusoidal basis functions. The shooting method [63][64][27] is a time domain simulation technique used to directly capture the steady state response of nonlinear systems. Unlike

1. This is in fact somewhat optimistic in the context of device simulation.

harmonic balance, it relies on numerical integration in the time domain, and is very robust for extremely nonlinear problems. Unfortunately, its reliance on time domain integration means that the shooting method suffers the same drawbacks as standard transient analysis with regards to handling multi-tone inputs with very narrow or very wide frequency spacing, and with regards to simulating systems containing convolution-based distributed passive components.

5.2.1 The Basic Algorithm

Consider once again the equation

$$\boldsymbol{g}(x(t)) + \frac{d}{dt}\boldsymbol{q}(x(t)) = \boldsymbol{w}(t), \tag{5.15}$$

where ***w(t)*** is a driving function of period *T*. The periodic steady state solution must satisfy the governing equation (5.15), along with the two-point boundary condition

$$\boldsymbol{x}(T) - \boldsymbol{x}(0) = \boldsymbol{0}. \tag{5.16}$$

As in Section 2.5, the time axis can be discretized over a given period into a collection of points $t_0, t_1, \ldots, t_M$, where in this case $t_0 = 0$ and $t_M = T$. A suitable discretization, such as the Backward Euler scheme

$$\boldsymbol{g}(\boldsymbol{x}(t_m)) + \frac{\boldsymbol{q}(\boldsymbol{x}(t_m)) - \boldsymbol{q}(\boldsymbol{x}(t_{m-1}))}{t_m - t_{m-1}} - \boldsymbol{w}(t_m) = 0 \tag{5.17}$$

allows us to compute the solution points $\boldsymbol{x}_m = \boldsymbol{x}(t_m)$ for *m* ranging from 0 to M. For a one-step method, a given point $\boldsymbol{x}_m$ for $m > 0$ is a function only of the preceding point — i.e., $\boldsymbol{x}_m = \varphi_{m,\,m-1}(\boldsymbol{x}_{m-1})$. In general, any solution point $\boldsymbol{x}_m$ can be viewed as a function of the initial guess $\boldsymbol{x}_0$:

$$\boldsymbol{x}_m = \varphi_{m0}(\boldsymbol{x}_0) \tag{5.18}$$

The goal of the shooting method is to find a value of $\boldsymbol{x}_0$ such that (5.16) is satisfied. In the context of the preceding discussion, this means that we must solve the nonlinear algebraic problem

$$\varphi_{M0}(\boldsymbol{x}_0) - \boldsymbol{x}_0 = \boldsymbol{0}. \tag{5.19}$$

The function φ is sometimes referred to as the state transition function.

In classical implementations of the shooting method, (5.19) is solved by using the Newton-Raphson algorithm with direct LU factorization. To obtain the analytic form of the relevant Jacobian, the chain rule can be used to obtain

$$\frac{d\varphi_{M0}}{d\boldsymbol{x}_0} = \frac{d\boldsymbol{x}_M}{d\boldsymbol{x}_0} = \frac{d\boldsymbol{x}_M}{d\boldsymbol{x}_{M-1}} \cdot \frac{d\boldsymbol{x}_{M-1}}{d\boldsymbol{x}_{M-2}} \cdot \ldots \cdot \frac{d\boldsymbol{x}_1}{d\boldsymbol{x}_0}. \tag{5.20}$$

To obtain each of the intermediate derivatives in the product above, we differentiate (5.17) with respect to $\boldsymbol{x}_{m-1}$ to find that

$$\boldsymbol{g}'(\boldsymbol{x}_m)\frac{d\boldsymbol{x}_m}{d\boldsymbol{x}_{m-1}} + \frac{1}{t_m - t_{m-1}}\left(\boldsymbol{q}'(\boldsymbol{x}_m)\frac{d\boldsymbol{x}_m}{d\boldsymbol{x}_{m-1}} - \boldsymbol{q}'(\boldsymbol{x}_{m-1})\right) = 0, \tag{5.21}$$

or equivalently

$$\frac{d\boldsymbol{x}_m}{d\boldsymbol{x}_{m-1}} = [\,(t_m - t_{m-1})\,\boldsymbol{g}'(\boldsymbol{x}_m) + \boldsymbol{q}'(\boldsymbol{x}_m)\,]^{-1}\boldsymbol{q}'(\boldsymbol{x}_{m-1})\,. \tag{5.22}$$

The shooting Jacobian may now be written in product form as

$$\frac{d\varphi_{M0}}{d\boldsymbol{x}_0} = \prod_{m=1}^{M} [\,(t_m - t_{m-1})\,\boldsymbol{g}'(\boldsymbol{x}_m) + \boldsymbol{q}'(\boldsymbol{x}_m)\,]^{-1}\boldsymbol{q}'(\boldsymbol{x}_{m-1})\,. \tag{5.23}$$

Like the standard transient Jacobian, the shooting matrix has dimensionality $N \times N$. However, standard transient Jacobians are sparse, because the derivative matrices $\boldsymbol{g}'(\boldsymbol{x}_m)$ and $\boldsymbol{q}'(\boldsymbol{x}_m)$ are sparse. The shooting Jacobian, on the other hand, is structurally dense, since the product of the inverses of sparse matrices is in general structurally dense. The cost to assemble and factor $d\varphi_{M0}/d\boldsymbol{x}_0$ is very expensive when compared to the factorization of conventional transient Jacobians — a fact that makes the shooting method with direct LU factorization impractical for large problems.

5.2.2 The Matrix-Implicit Variant

To apply the shooting method to large problems, a matrix-implicit variant of the algorithm was developed [65]. Krylov subspace algorithms are used to solve the linear matrix problem involving the shooting Jacobian, and the dense matrix is not be explicitly computed or stored. As in this work, GMRES is used as the solution method of choice. The authors report order-of-magnitude improvements over non-matrix-implicit shooting methods for moderately sized (< 400 nodes) circuit problems.

One serious drawback, present even in the matrix-implicit algorithm, is the large amount of storage required for simulation. To carry out the matrix-vector products needed by GMRES, the (sparse) factored Jacobian

$$(t_m - t_{m-1})\,\boldsymbol{g}'(\boldsymbol{x}_m) + \boldsymbol{q}'(\boldsymbol{x}_m) \tag{5.24}$$

along with the capacitive matrix $\boldsymbol{q}'(\boldsymbol{x}_m)$ must be stored in memory or written to disk at each time point *m*. Once this has been done at each time point of the shooting interval, the GMRES matrix-vector products can be computed efficiently as

$$\frac{d\varphi_{M0}}{d\boldsymbol{x}_0}\cdot\boldsymbol{v} = \prod_{m=1}^{M}\left[(t_m - t_{m-1})\,\boldsymbol{g}'(\boldsymbol{x}_m) + \boldsymbol{q}'(\boldsymbol{x}_m)\right]^{-1}\boldsymbol{q}'(\boldsymbol{x}_{m-1})\cdot\boldsymbol{v} \tag{5.25}$$

The products $\boldsymbol{q}'(\boldsymbol{x}_{m-1})\cdot\boldsymbol{v}$ can be carried out quickly because of the sparsity of $\boldsymbol{q}'(\boldsymbol{x}_{m-1})$. The remainder of the operation can be accomplished by backsolving with the factored matrices (5.24) residing in storage. As a point of comparison, we remark that a device simulation problem with a 10 MB DC Jacobian would require over a GB of storage if 100 time points were used over the shooting period.

5.2.3 Strengths and Weaknesses

When compared to harmonic balance, the shooting method's biggest (and perhaps only) appeal lies in its robust behavior for highly nonlinear problems. Unlike the Krylov-based harmonic balance technique, where high levels of nonlinearity cause the HB Jacobian to lose its diagonally dominant form and become difficult to precondition, the shooting method is not particularly sensitive to high levels of distortion. This can be a key advantage for some highly nonlinear applications.

In our attempt to develop a steady state solver for device-level applications, however, time domain shooting appears, on the whole, to be a less satisfactory technique than harmonic balance. One serious drawback of the shooting method is its inability to adequately handle large signal multi-tone inputs. For instance, consider applying a two-tone distortion test to a bandpass amplifier, where the two tones have equal amplitude and are spaced 30 kHz apart around a 1 GHz center frequency. The shooting period in this case would be 0.2 ms, whereas the time step would need to be well under 1 ns. Clearly, the million or so time points that are required by the shooting method for this type of simulation are well beyond the capability of any desktop workstation. The harmonic balance algorithms of the preceding chapter, however, are able to handle such problems routinely. We should point out that in cases where the amplitude of one of the input tones can be regarded as small-signal (as in the case of a low-amplitude RF mixer input, for example) a large-signal/small-signal analysis on top of the shooting method [67][68] is

available. However, in the common scenario where multiple tones are truly large-signal, the analysis of this paragraph holds.

Another area where time domain shooting runs into difficulty is in the simulation of distributed elements requiring use of the convolution integral $y(t) \otimes \boldsymbol{x}(t)$. In addition to the standard problems of passivity and causality[1] encountered by conventional time domain simulators, the shooting method runs into difficulties caused by the introduction of each time point's dependence on a potentially long past history. This dependence is introduced by long impulse responses in $y(t)$, and, at a minimum, presents moderately serious complications to the preconditioning scheme put forth in [66]. Harmonic balance, of course, faces no such problems — indeed, it excels at handling arbitrary linear circuitry, regardless of whether the associated impulse responses correspond to lumped or distributed elements.

5.3 Summary

The choice between transient analysis, harmonic balance, circuit envelope, or the shooting method depends on both the application and the problem to be simulated. In some cases, a given method is simply inapplicable for the problem at hand. For example, if a simulation of transient behavior is called for, neither harmonic balance nor the shooting method is applicable, because they're both steady state analysis techniques. In other cases, any of the four methods could be used in principle, although in practice their use could result in prohibitively expensive or inaccurate simulations, or even serious convergence problems.

The focus of this work is on large signal steady state analysis of semiconductor devices for RF and microwave applications, and thus the four aforementioned simulation algorithms are evaluated in this light. Table 5.1 presents a comparison illustrating the strengths, weaknesses, and areas of application for the various techniques. In practical terms, harmonic balance is the most realistic approach for handling multi-tone device-level RF simulation problems with a moderate number of harmonics (i.e., a couple

1. Passivity and causality arise as issues when measured frequency domain data is used in transient simulations.

hundred or less). As we've seen, transient analysis is entirely unsuitable for the task, both because it handles multi-tone inputs poorly, and because it requires lengthy integrations to reach steady state. The shooting method is a very robust simulation technique that is superior to harmonic balance in single-tone analysis of amplifiers driven into severe compression (Krylov-based HB with standard preconditioners typically begins to have some difficulties at 3dB of gain compression or so, although some amplifiers have been successfully simulated at significantly higher levels of compression). Unfortunately, the computational expense incurred for multi-tone shooting method simulation is thoroughly impractical for physics-based device simulation.

	Transient Analysis	Harmonic Balance	Circuit Envelope	Shooting Method
Steady state solver?	no	yes	no	yes
Ability to deal with widely-spaced carrier frequencies	poor	excellent	excellent	poor[a]
Handling of highly nonlinear problems	excellent	fair	fair to good	excellent
Handling of distributed linear elements	poor to fair	excellent	fair to good	poor
Ability to simulate highly complex modulated signals	poor	fair to good	excellent	poor
Efficient periodic large-signal / small-signal analysis?	no	yes	no	yes

Table 5.1 A comparison of simulation algorithms.

a. Assuming that the amplitudes are large-signal.

The important area of device-level simulation with digitally modulated signal inputs is also beyond the reach of our tools at the moment. Clearly, the circuit envelope algorithm, in conjuction with Krylov-based harmonic balance, brings the memory requirements down to a reasonable level. It is not clear, however, that the resulting simulation can be completed in a reasonable amount of time, and the envelope analysis was not implemented in the course of this research. Future work in this area will no doubt shed light on the practicality of such simulations.

Chapter 6

Examples and Results

The harmonic balance device simulator developed during the course of this work has been used to analyze a number of practical device structures from both industrial and academic sources. Silicon bipolar, MOS, SOI, and diode devices have been simulated in RF amplifier, mixer, and rectifier applications. GaAs MESFETs for use in microwave power amplifier circuits have been analyzed as well. In this chapter, these examples are presented in conjunction with simulator benchmark data, and, where possible, comparison with actual experimental results.

All simulation results reported in this section were obtained on an HP-J210 workstation with 190MB of RAM. The memory usage quoted in these examples includes an additional 40MB of PISCES static arrays which are not used by the harmonic balance engine. In principle, the memory usage quoted below could be reduced by 40MB with the same algorithms applied to a suitably modified PISCES code. The two-tone simulations quoted below were performed with sectioned preconditioners. No other memory reduction features were turned on, as all the examples fit quite comfortably into the available RAM.

6.1 A GaAs MESFET Example

This example focuses on the design a GaAs FET amplifier with low levels of harmonic distortion [7][2]. A key goal is the design of an impurity profile which keeps

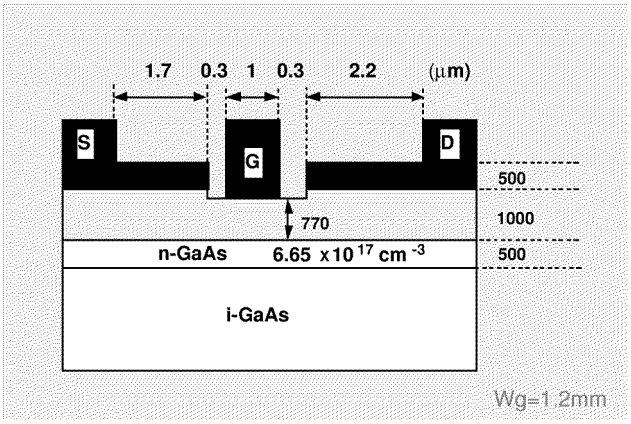

Figure 6.1 Cross-section of GaAs MESFET power device.

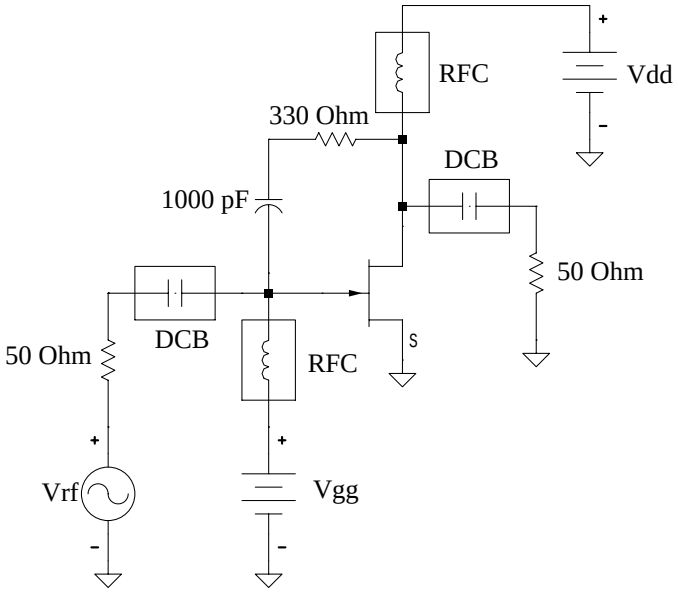

Figure 6.2 External circuit configuration for the GaAs MESFET power amplifier.

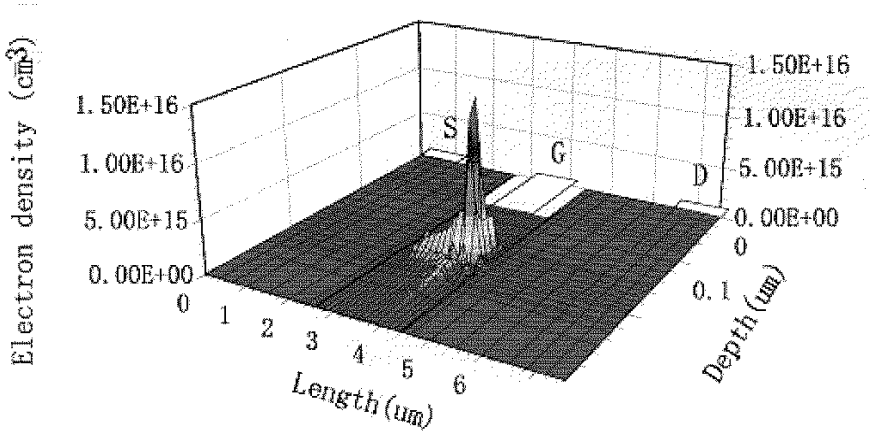

Figure 6.3 Bird's eye plot of distortion in electron concentration inside the MESFET of Figure 6.1.

transconductance constant and decreases the variation in gate-source and gate-drain capacitances. In order to analyze this device and compare the simulated results with measurements, the surrounding circuitry must be set up as in Figure 6.2. RF chokes and blocking capacitors are present, along with 50 Ω terminations on the RF input and output. Parasitics surrounding the device are also included. A comparison between simulated and measured data for a two-tone intermodulation distortion test is shown in Figure 6.4. For this test, the two input tone frequencies were set to 400 MHz and 500 MHz, and their power was swept from -30 dBm to 0 dBm under the bias conditions of V_{gs} = -2.5*V*, V_{ds} = 3*V*. As can be seen from the figure, the agreement is quite reasonable. Several single-tone measurements and simulations were performed as well, yielding agreement comparable to the two-tone case. To examine the causes of distortion with a view towards optimizing the device structure, plots of 2nd harmonic generation inside the device were generated by the harmonic balance device simulator (see Figure 6.3). By carefully studying such internal distortion plots, industrial device designers were able to alter the device structure to achieve improved distortion performance [70]. The interested reader is referred to [7] and [5] for additional experimental comparisons and physical insight.

In carrying out simulations for this device structure, 952 grid nodes and 2 auxiliary KCL equations were used, yielding a total time domain size of $N = 2858$. For single-tone HB analyses using 15 harmonics (i.e., $H = 15$), the total HB system size was 88,598

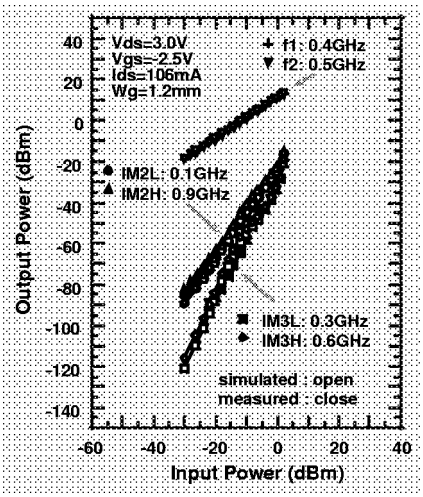

Figure 6.4 Comparison between experimental measurements and simulated results.

unknowns. Solution times varied from under 11 min. per HB analysis at RF source levels less than 100mV, to about an hour near 1V. Total memory usage was 121MB.

A larger GaAs FET was analyzed under two-tone excitation to illustrate the code's effectiveness on large-scale problems. A two-tone RF input was applied (2GHz and 1.9GHz), with both tone magnitudes at 100mV. The device had 1406 grid points and two auxiliary equations, for a time domain system size of $N = 4220$. For a two-tone analysis with $H = 110$, the total number of unknowns came to 932,620. Total execution time was 2hr. 8 min., with memory usage at 360MB.

6.2 Distortion Analysis of an SOI BJT

Figure 6.5 shows a Silicon-On-Insulator bipolar device, where the active region is isolated by a 0.5μm oxide layer. While the original structure [71] has an n^+ floating collector layer underneath the vertical *npn* transistor at the Si-SiO_2 interface, this structure relies on the back gate (i.e. the substrate) bias to form a high electron concentration layer at the interface. When the substrate bias is increased positively with respect to the emitter, an electron accumulation layer is formed as shown in Figure 6.6. This high concentration layer helps reduce the transit time for electrons to cross the collector region as is evident in

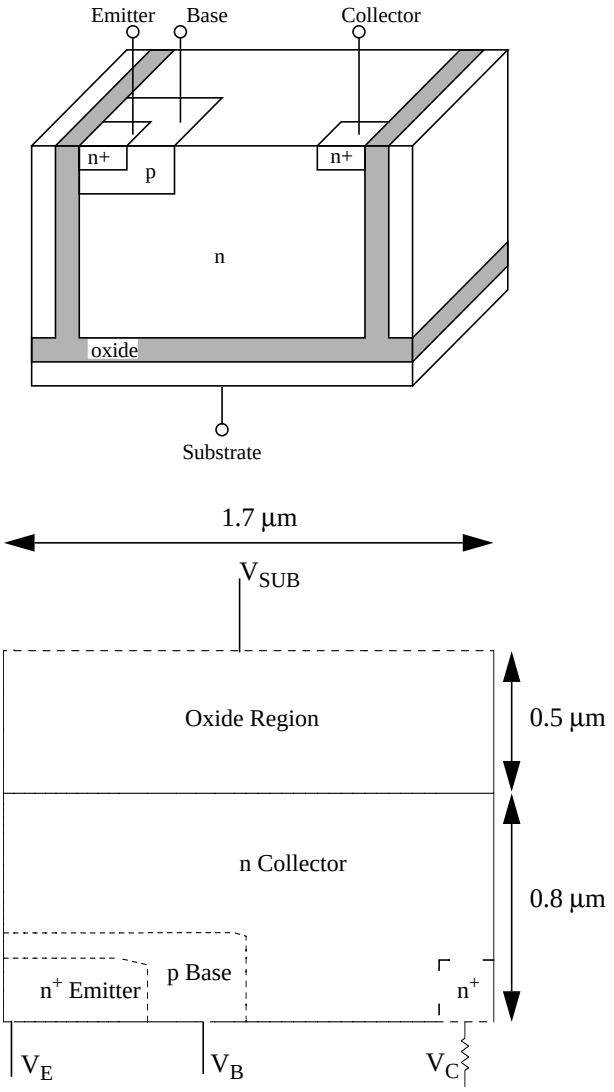

Figure 6.5 Power SOI BJT structure. The 3D rendering (top) is not to scale. The 2-D cross-section (bottom) is oriented such that it is consistent with subsequent contour and mesh plots.

Figure 6.7, where the cutoff frequency (f_T) is plotted vesus the collector current density. The improvement in f_T is about 10% for V_{sub}=10V. Furthermore, as our simulation shows, the overall distortion level in the output (i.e. collector) current is reduced by as much as

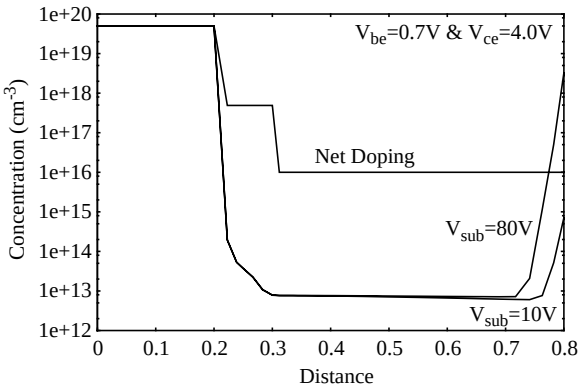

Figure 6.6 Formation of electron accumulation layer at the Si-SiO_2 interface induced by the positive substrate bias.

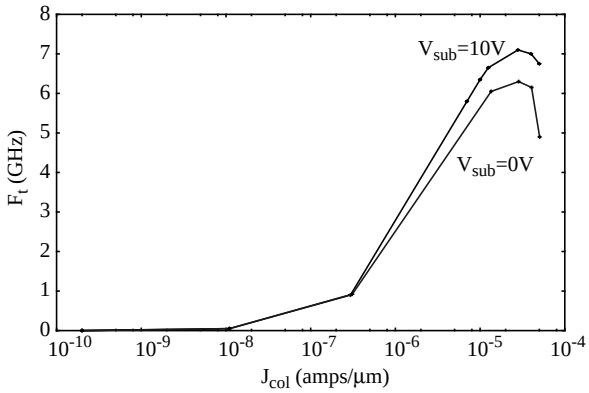

Figure 6.7 Improvement in f_T at V_{sub} = 10V (dashed line) over that at V_{sub} = 0V (solid line).

20% when compared to zero substrate bias. The physical explanation for this reduction is as follows.

One key contributor to distortion is the nonlinearity of the base-collector junction capacitance, which is modulated by the large swing of the output signal. When a high electron concentration layer is present at the Si-SiO_2 interface, the potential at this layer is essentially clamped (or “locked”), limiting the AC voltage swing across the base-collector

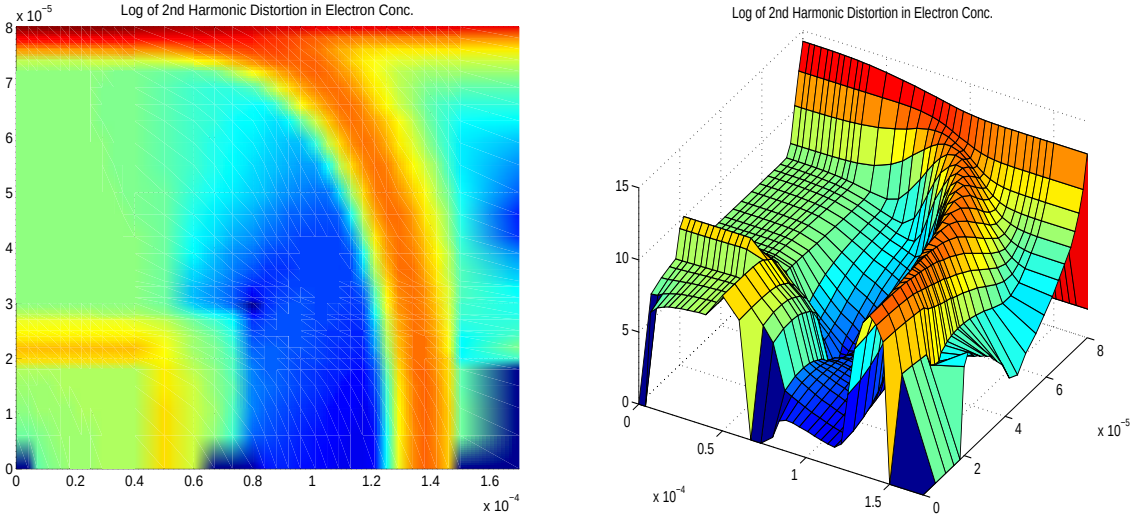

Figure 6.10 Logarithmic contour (left) and perspective (right) plots for the 2nd harmonic of electron concentration.

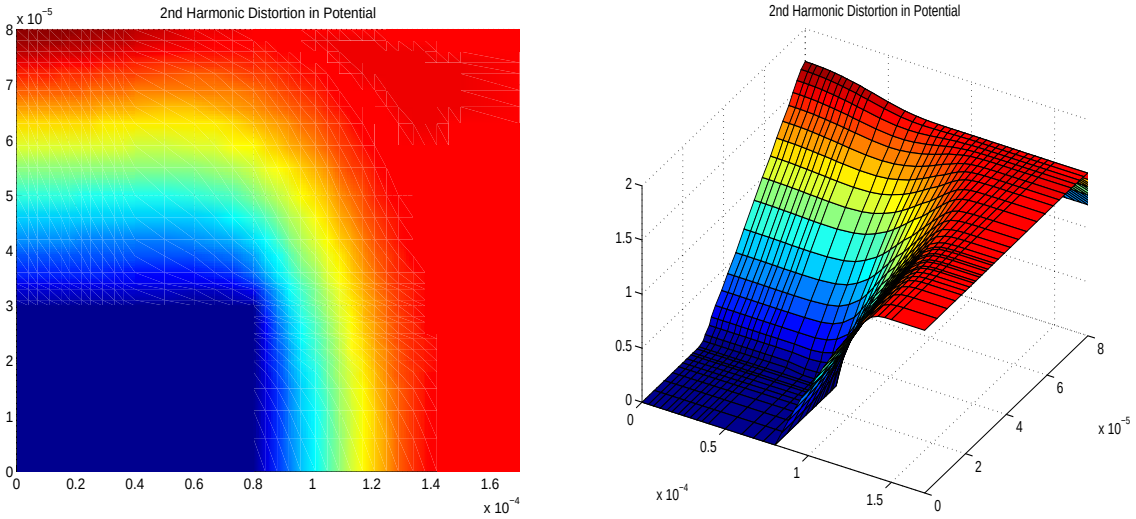

Figure 6.11 Logarithmic contour (left) and perspective (right) plots for the 2nd harmonic of electrostatic potential.

junction. This phenomenon causes a reduction in the distortion levels present throughout the transistor.

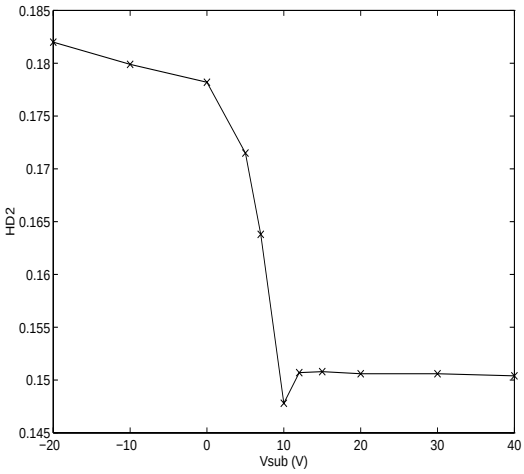

Figure 6.8 Harmonic distortion in collector current as a function of substrate bias.

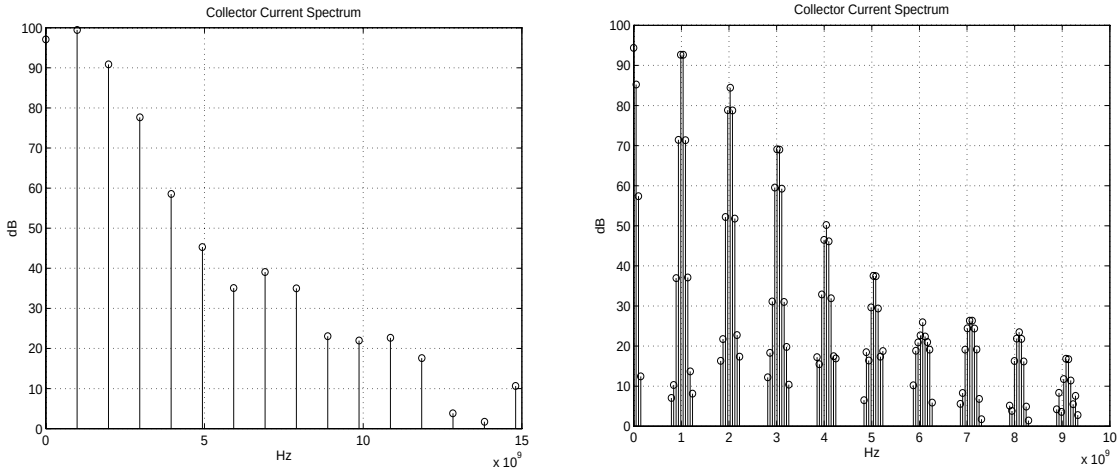

Figure 6.9 Collector current spectrum for one-tone (left) and two-tone (right) simulations.

The grid size for simulating this device was 1190 nodes. An $H = 15$ one-tone simulation at a 50mV drive level with a base-emitter bias of 0.7V took 52 min. and 150 MB of RAM. The total number of unknowns for this simulation was 110,670. For a two-tone intermodulation distortion analysis with 20mV tones and $H = 90$, the total number

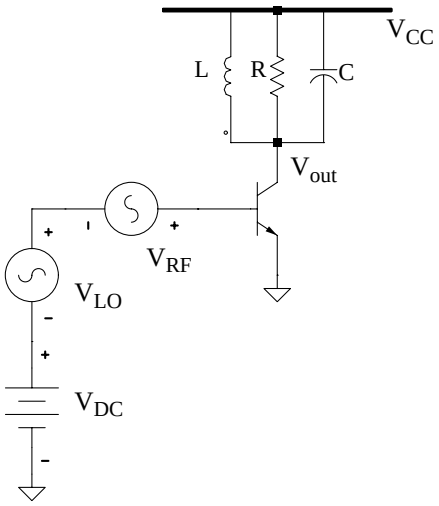

Figure 6.12 A single-device BJT mixer. The resonant circuit at the output is tuned to either the sum or the difference frequency of the LO and RF, depending on the application.

of unknowns was 646,170, the run-time was 3hr. 32 min., and the memory usage was 305 MB. Figure 6.8 shows the 2nd harmonic distortion as a function of substrate bias, while Figure 6.9 shows spectral plots of the collector current for both the one- and two-tone simulations. As in the GaAs MESFET example of the preceding section, we note that the simulator can compute harmonic distributions of fundamental variables inside the device. As an illustration, plots of the 2nd harmonic of electron concentration (Figure 6.10) and electrostatic potential (Figure 6.11) are shown. In the hands of an experienced device designer, such information can help to identify the origins of distortion, and assist in improving the device design.

6.3 A High-Q Single-BJT Mixer Example

A single-BJT mixer circuit is taken directly from [69], p. 445. The configuration is shown in Figure 6.12 of this paper. The goal of the mixer circuit is to downconvert a 500.1 MHz RF signal down to a 100 kHz IF, using a 500 MHz LO. A resonant RLC circuit having $Q=2\pi 100$ is used ($R = 15\ k\Omega$, $C = 66.667$ nF, $L = 37.995\ \mu H$). The resonant

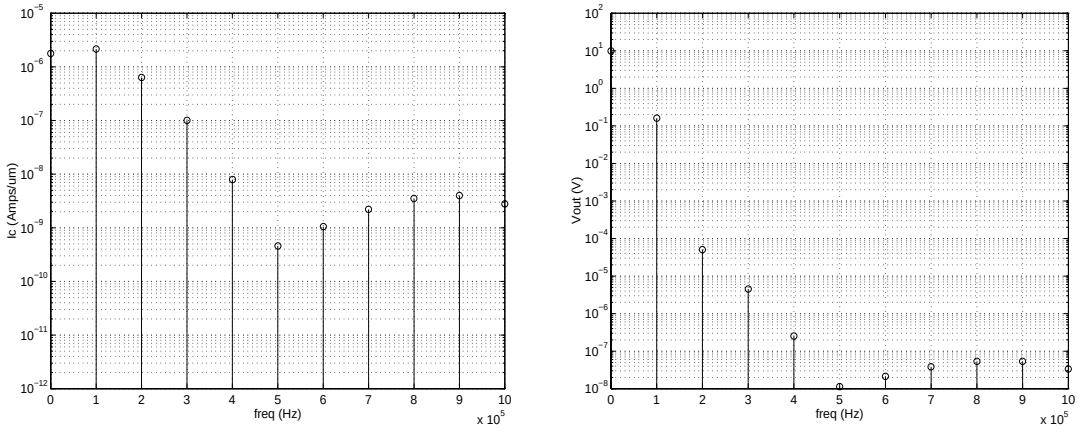

Figure 6.13 Baseband spectrum of the collector current (left) and output voltage (right). Note the suppression of distortion components by the resonant circuit in the output waveform.

frequency is 100 kHz, and the high Q effectively filters out the IF-band distortion products. The voltage source parameters used are $V_{CC} = 10V$, $V_{DC} = 0.7V$, $V_{RF} = 0.05V$ at 500.1 MHz, and $V_{LO} = 0.15V$ at 500 MHz. A silicon BJT from [72] was employed, resulting in a total (DC) system size of $N = 2114$. A harmonic balance analysis at $H = 110$ frequencies was carried out, for a total harmonic balance problem size of $(2H + 1)N = 467,194$. The simulation required 64 min. and 219 MB of RAM.

The results are presented in Figure 6.13. Only the relevant baseband portions of the spectrum are shown in the figure, due to the very large differential in the frequencies present. The large levels of distortion present in the BJT's collector current are effectively filtered out using the RLC resonator. Consequently, the 200 kHz distortion component is over 70 dB down relative to the desired IF signal at 100 kHz. The distortion level could be further reduced by using a resonator with a higher Q, or by reducing the relatively high RF drive level.

6.4 An LDMOS Device for RF Applications

There has been growing interest in the use of silicon MOS transistors, and in particular laterally-diffused (LDMOS) devices, for RF power amplification. Rotella has performed

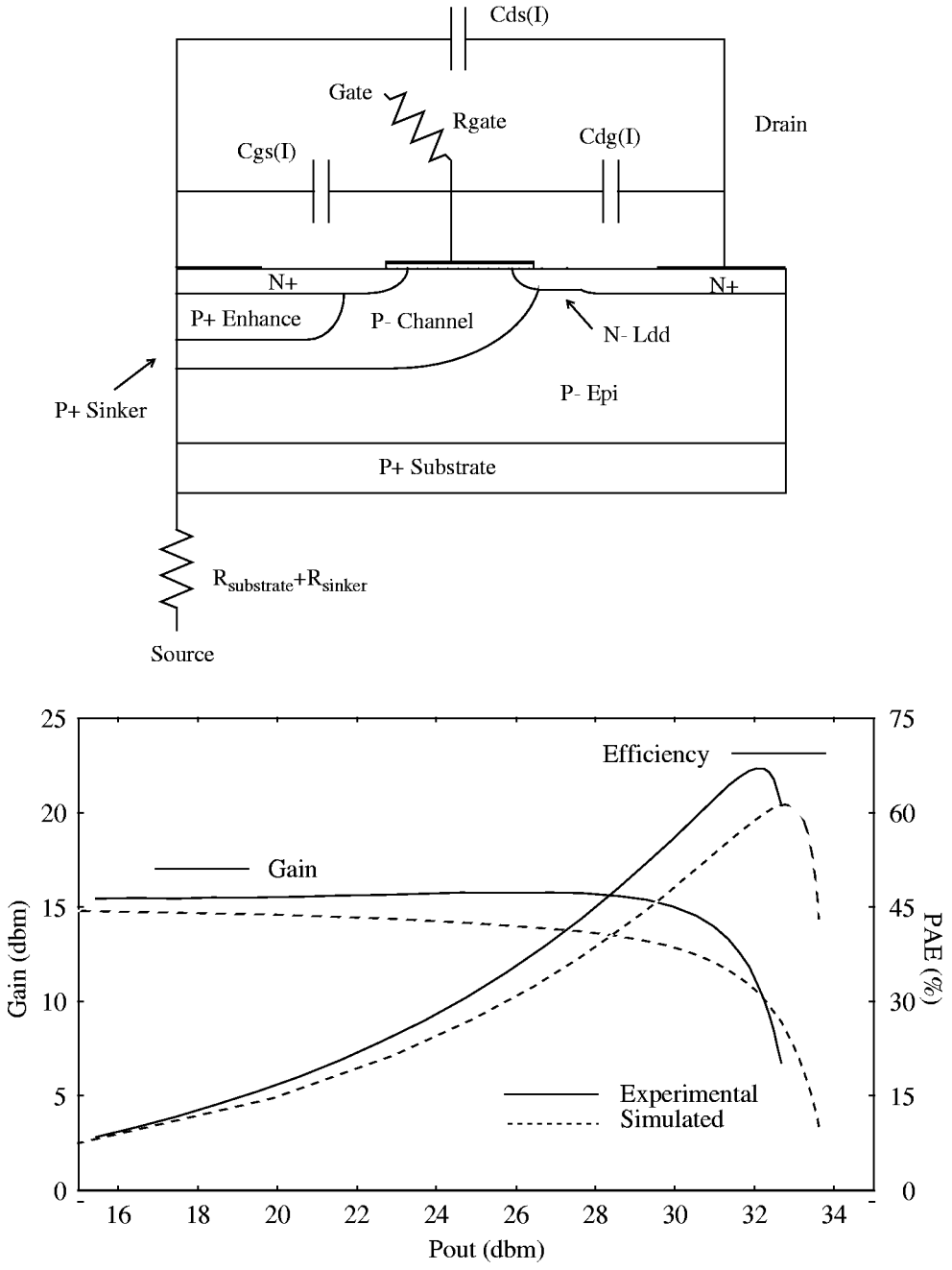

Figure 6.14 LDMOS device cross-section (top) and its simulated-vs-measured gain/PAE curves (bottom).

detailed harmonic balance PISCES simulations of an RF LDMOS device [6]. The transistor cross-section and parasitic packaging components, along with a comparison of the simulated vs. measured results, are shown in Figure 6.14. Several unique features are incorporated into the structure to improve the RF and power performance characteristics of the device [5]. Among these is a laterally diffused, graded channel that enhances the RF performance through a drift region and prevents punch-through, thus increasing the device's transconductance. A p^+ sinker, not shown in the figure but modeled by a side contact to the device for simulation purposes, connects the source and substrate together to eliminate extra bonding wires. An n-type LDD region decreases the electric field at the drain end of the channel, and improves BV_{dss} and C_{dg}.

For accurate RF simulation, proper modeling of parasitic components such as gate/source resistances and interconnect capacitances can be as important as the modeling of the intrinsic device structure itself. The comparison between simulated and measured power gain and power added efficiency in Figure 6.14 shows a reasonable level of agreement, especially considering the sensitivity of the results to parasitic components. A detailed discussion of all the results is beyond the scope and aim of the present section; for a more thorough treatment which includes the effect of device parameters on RF performance, the interested reader is referred to [6] and [5].

6.5 Summary

This chapter has presented several examples in order to demonstrate the simulator's applicability to practical problems, and to give the reader an indication of the kinds of computing resource requirements needed by the code. Below, we present a table summarizing the results. Due to the proprietary nature of the LDMOS example, the PISCES input deck for the device was not available to the author, and thus the benchmarks for the example are not supplied below.

Example	Grid Nodes	KCL Eqns	H	Total Size	CPU Time	RAM
GaAsFET (50mV) (medium-size grid)	952	2	15	88,598	6min 40sec	121MB
GaAsFET (100mV) (medium-size grid)	952	2	15	88,598	8min 27 sec	121MB
GaAsFET (100mV) (large grid)	1406	2	110	932,620	1hr 45min	360MB
SOI BJT (1-tone, 50 mV)	1190	0	15	110,670	29min 27sec	150MB
SOI BJT (2-tone, 20mV)	1190	0	90	646,170	3hr 10min	305MB
High-Q mixer (2-tone, 0.15V LO, 0.05 V RF)	704	2	110	467,194	64min 11sec	219MB

Table 6.1 Summary of simulation results for the examples of Chapter 6.

Chapter 7

Conclusion

7.1 Summary

The primary goal of this work was to develop algorithms for practical two-dimensional device-level harmonic balance simulation, and to implement these algorithms in a prototype code based on the PISCES-II simulator. Recent advances in large-scale harmonic balance circuit simulation provide an excellent starting point for solving the corresponding problem at the device level. However, the size, structure, and density of the semiconductor device Jacobian necessitates development of special-purpose techniques for solving device-level harmonic balance problems, particularly in the multi-tone case. The algorithms presented in this work are geared towards enabling physics-based HB device simulation on ordinary mid-range workstations. The prototype code developed during the course of this research has been successfully applied to a number of device structures from both industrial and academic sources, and has shown itself to be a practical tool for investigating large signal distortion effects at the physical level.

The primary contributions of this work can be summarized as follows:

- A practical harmonic balance device simulator was developed based on the PISCES-II code. To our knowledge, this is the first true harmonic balance based semiconductor device simulation tool. All of the standard PISCES models and

features are available — the HB analysis extension places no additional restrictions on the device being simulated.

- Krylov subspace techniques were applied to solve the large-scale systems of equations that arise in HB device simulation. An investigation of the various Krylov subspace solver variants showed that GMRES was superior to the alternatives in the context of semiconductor device simulation.
- A sectioned preconditioner was developed to cope with device-level multi-tone distortion analyses. The preconditioner provides dramatic reductions in memory usage when compared to the block-diagonal preconditioners commonly employed in circuit-level harmonic balance simulators.
- Techniques for reducing memory usage associated with storage of the HB Jacobian representation were developed.[1]
- One unique advantage of harmonic balance device simulation is the availability of internal state variables within the device structure. Plots of distortion in internal device quantities such as electrostatic potential, free carrier concentration, and conduction and displacement current densities have been presented in the course of this research for various device structures.

7.2 Future Work

Several areas of investigation should be pursued in the future to improve on the algorithms presented in this work, and to maximize the benefits of device-level HB analysis. Further research is suggested in the following areas:

- Better preconditioners, particularly in the high-distortion regime, need to be developed.
- Currently, the harmonic balance truncation orders are specified by the user. Ideally, the simulator should adjust the truncation scheme during the course of a simulation to provide sufficient accuracy.

1. These techniques were also independently developed by other groups working in the area of circuit simulation.

- Although the spectral content of internal device quantities has been plotted, and in some cases used by industrial device designers to optimize transistor structure, the physical insight provided by the distortion plots is not fully understood. Future work by device designers to exploit this information is called for.
- A parallel version of the simulator would speed simulation times considerably, as most of the time-consuming operations used by the code are readily parallelizable.
- Multiple device capability, particularly in the context of a parallel version of the code, would be useful for physics-based simulation of designs that require a small number of physically modeled transistors simulated in conjunction with circuit-based compact models.

References

[1] B. Troyanovsky, F. Rotella, Z. Yu, R. W. Dutton, and T. Arnborg, ‘‘Efficient multi-tone harmonic balance simulation of semiconductor devices in the presence of linear high-Q circuitry,’’ *Proc. SASIMI ’97*, Dec. 1997.

[2] B. Troyanovsky, F. Rotella, Z. Yu, R. W. Dutton, and J. Sato-Iwanaga, ‘‘Large signal analysis of RF/microwave devices with parasitics using harmonic balance device simulation,’’ *Proc. SASIMI ’96*, Nov. 1996.

[3] B. Troyanovsky, Z. Yu, L. So, and R. W. Dutton, ‘‘Relaxation-based harmonic balance technique for semiconductor device simulation,” *Proc. IEEE/ACM International Conf. on Computer-Aided Design*, pp. 700-703, Nov. 1995.

[4] B. Troyanovsky, Z. Yu, and R. W. Dutton, “Large signal frequency domain device analysis via the harmonic balance technique,” *Simulation of Semiconductor Devices and Processes*, Vol. 6, pp.114-117, Sep. 1995.

[5] R. W. Dutton, B. Troyanovsky, Z. Yu, T. Arnborg, F. Rotella, G. Ma, and J. Sato-Iwanaga, ‘‘Device simulation for RF applications,’’ to appear in *Proc. IEDM*, Dec. 1997.

[6] F. M. Rotella, B. Troyanovsky, Z. Yu, R. W. Dutton, and G. Ma, “Harmonic balance device analysis of an LDMOS RF power amplifier with parasitics and matching network,” *Proc. SISPAD `97*, p. 157, Sept. 1997.

[7] J. Sato-Iwanaga, K. Fujimoto, H. Masato, Y. Ota, K. Inoue, B. Troyanovsky, Z. Yu, and R. W. Dutton, ‘‘Distortion analysis of GaAs MESFETs based on physical model using PISCES-HB,’’ *Proc. IEDM*, pp. 163-166, Dec. 1996.

[8] R. W. Dutton, B. Troyanovsky, Z. Yu, E.C. Kan, K. Wang, T. Chen, and T. Arnborg, “TCAD for analog circuit applications: virtual devices and instruments,” *Proc. IEEE International Solid-State Circuits Conference*, pp. 78-79, 422, Feb. 1996.

[9] R. W. Dutton, Z. Yu, F. Rotella, S. Beebe, B. Troyanovsky, and L. So, ‘‘Virtual instruments for development of high performance circuit technologies,’’ *Proc. of the IEEE Custom Integrated Circuits Conference*, pp. 225-228, May 1995.

[10] M. R. Pinto, C. S. Rafferty, and R. W. Dutton, “PISCES II: Poisson and continuity equation solver,” Stanford Electronics Lab., Tech. Report, Sept. 1984.

[11] Z. Yu, D. Chen, L. So, and R.W. Dutton, *PISCES-2ET --- Two-Dimensional Device Simulation for Silicon And Heterostructures*, Stanford University, 1994.

[12] L. W. Nagel, *SPICE2: A Computer Program to Simulate Semiconductor Circuits*, Ph. D. Thesis, University of California at Berkeley, May 1975.

[13] *Hewlett-Packard Microwave Design System (MDS)*, Hewlett-Packard Co., Santa Rosa, CA.

[14] D. L. Scharfetter and H. K. Gummel, ‘‘Large-signal analysis of a Silicon Read diode oscillator,’’ *IEEE Transactions on Electron Devices*, vol. ED-16, pp. 66-77, 1969.

[15] B. Troyanovsky, N. Chang, and R. Dowell, ‘‘Integration of Transient S-Parameter Simulation Into HPSPICE,’’ *Proc. of the 1994 Design Technology Conference*, pp. 231-236, May 1994.

[16] S. Ramo, J. R. Whinnery, and T. Van Duzer, Fields and Waves in Communication Electronics, 2nd ed. New York: Wiley, 1984.

[17] G. Massobrio and P. Antognetti, *Semiconductor Device Modeling with SPICE*, 2nd ed., New York: McGraw-Hill, 1993.

[18] L. C. de Vreede, H. C. de Graaff, K. Mouthaan, M. de Kok, J. L. Tauritz, and R. G. Baets, ‘‘Advanced modeling of distortion effects in bipolar transistors using the MEXTRAM model,’’ *IEEE Journal on Solid-State Circuits*, vol. 31, pp. 114-121, Jan. 1996.

[19] R. E. Bank, W. M. Coughran, W. Fichtner, E. H. Grosse, D. J. Rose, and R. K. Smith, ‘‘Transient simulation of silicon devices and circuits,’’ *IEEE Transactions on Electron Devices*, vol. 32, pp. 1992-2007, Oct. 1985.

[20] A. Brambilla and D. D’Amore, ‘‘The simulation errors introduced by the SPICE transient analysis,’’ *IEEE Transactions on Circuits and Systems — I: Fundamental Theory and Applications*, vol. 40, pp. 57-60, Jan. 1993.

[21] M. S. Nakhla and J. Vlach, ‘‘A piecewise harmonic balance technique for determination of the periodic response of nonlinear systems,’’ *IEEE Transactions on Circuits and Systems*, vol. 23, pp. 85-91, Feb. 1976.

[22] K. S. Kundert and A. Sangiovanni-Vincentelli, ‘‘Simulation of nonlinear circuits in the frequency domain,’’ *IEEE Transactions on Microwave Theory and Techniques*, vol. 5, pp. 521-535, Oct. 1986.

[23] M. H. Protter and C. B. Morrey, *A First Course in Real Analysis*, New York: Springer-Verlag, 1977.

[24] J. Ortega and W. Rheinboldt, *Iterative Solution of Nonlinear Equations in Several Variables*, Orlando: Academic Press, 1970.

[25] K. S. Kundert, ‘‘Accurate Fourier analysis for circuit simulators,’’ *Proc. of the IEEE Custom Integrated Circuits Conference*, pp. 25-28, May 1994.

[26] D. Hente and R.H. Jansen, ‘‘Frequency domain continuation method for the analysis and stability investigation of nonlinear microwave circuits,’’ *IEE Proceedings*, part H, vol. 133, no.5, pp. 351-362, Oct. 1986.

[27] K. S. Kundert, J.K. White, and A. Sangiovanni-Vincentelli, *Steady-State Methods for Simulating Analog and Microwave Circuits*, Kluwer Academic Publishers, 1990.

[28] V. D.Hwang and T. Itoh, ‘‘Waveform-balance method for nonlinear MESFET amplifier simulation,’’ *IEEE 1989 MTT-S International Microwave Symposium Digest*, June 1989.

[29] V. Rizzoli and A. Neri, ‘‘State of the art and present trends in nonlinear microwave CAD techniques,’’ *IEEE Transactions on Microwave Theory and Techniques*, vol. 36, pp. 343-365, Feb. 1988.

[30] V. Rizzoli, C. Cecchetti, A. Lipparini, and F. Mastri, ‘‘General-purpose harmonic balance analysis of nonlinear microwave circuits under multitone excitation,’’ *IEEE Transactions on Microwave Theory and Techniques*, pp. 1650-1659, Dec. 1988.

[31] R. B. Bracewell, *The Fourier Transform and Its Applications, 2nd ed.*, New York: McGraw-Hill, 1986.

[32] P. L. Heron and M. B. Steer, ‘‘Jacobian calculation using the multidimensional Fast Fourier Transform in the harmonic balance analysis of nonlinear circuits,’’ *IEEE Transactions on Microwave Theory and Techniques*, vol. 38, pp. 429-431, April 1990.

[33] T. S. Parker and L. O. Chua, *Practical Numerical Algorithms for Chaotic Circuits*, New York: Springer-Verlag, 1989.

[34] L. O. Chua and P. M. Lin, *Computer-Aided Analysis of Electronic Circuits: Algorithms and Computational Techniques*, Englewood Cliffs, N.J.: Prentice-Hall, 1975.

[35] C. Ho, A. Ruehli, and P. A. Brennan, ‘‘The modified nodal approach to network analysis,’’ *IEEE Transactions on Circuits and Systems*, vol. CAS-32, pp. 504-509, June 1975.

[36] G. D. Hachtel, R. K. Brayton, and F. G. Gustafson, ‘‘The sparse tableau approach to network analysis and design,’’ *IEEE Transacations on Circuit Theory*, vol. CT-18, pp. 101-113, Jan. 1971.

[37] K. S. Kundert, ‘‘Sparse matrix techniques,’’ in *Circuit Analysis, Simulation, and Design*, North-Holland Publishing, pp. 281-324, 1986.

[38] P. Heikkila, M. Valtonen, and T. Veijola, ‘‘Harmonic balance of nonlinear circuits with multitone excitation,’’ *Proc. of the 10th European Conference on Circuit Theory and Design*, Copenhagen, Denmark, 1991.

[39] R. Melville, P. Feldmann, and J. Roychowdhury, ‘‘Efficient multi-tone distortion analysis of analog integrated circuits,‘’ *Proc. of the IEEE Custom Integrated Circuits Conference*, pp. 241-244, May 1995.

[40] P. Feldmann, R. Melville, and D. Long, ‘‘Efficient frequency domain analysis of large nonlinear analog circuits,‘’ *Proc. of the IEEE Custom Integrated Circuits Conference*, pp. 461-464, May 1996.

[41] D. Long, R. Melville, K. Ashby, and B. Horton, ‘‘Full-chip harmonic balance,’’ *Proc. of the IEEE Custom Integrated Circuits Conference*, pp. 379-382, May 1997.

[42] H. G. Brachtendorf, G. Welsch, and R. Laur, ‘‘Fast simulation of the steady-state of circuits by the harmonic balance technique,’’ *Proc. of the IEEE International Symposium on Circuits and Systems*, pp. 1388-1391, May 1995.

[43] H. G. Brachtendorf, G. Welsch, R. Laur, and A. Bunse-Gerstner, ‘‘Numerical steady state analysis of electronic circuits driven by multi-tone signals,’’ *Electrical Engineering*, vol. 79, pp. 103-112, April 1996.

[44] V. Rizzoli, F. Mastri, F. Sgallari, and G. Spaletta, ‘‘Harmonic balance simulation of strongly nonlinear very large-size microwave circuits by inexact Newton methods,’’ *IEEE MTT-S International Microwave Symposium Digest*, pp. 1357-1360, June 1996.

[45] M. R. Pinto, *Comprehensive Semiconductor Device Simulation for Silicon ULSI*, Ph.D. Thesis, Stanford University, Stanford, CA, Aug. 1990.

[46] Y. Saad and M.H. Schultz, ‘‘GMRES: a generalized minimal residual method for solving nonsymmetric linear systems,’’ *SIAM Journal on Scientific and Statisitical Computing*, vol. 7, pp. 856-869, July 1986.

[47] H. F. Walker, ‘‘Implementation of the GMRES method using Householder transformations,’’ *SIAM Journal on Scientific and Statisitical Computing*, vol. 9, pp. 152-163, Jan. 1988.

[48] G. H. Golub and C. F. Van Loan, *Matrix Computations*, Baltimore: The Johns Hopkins University Press, 1996.

[49] O. Axelsson, *Iterative Solution Methods*, New York: Cambridge University Press, 1996.

[50] Y. Saad, *Iterative Methods for Sparse Linear Systems*, Boston: PWS Publishing Company, 1996.

[51] C. T. Kelley, *Iterative Methods for Linear and Nonlinear Equations*, Philardelphia: SIAM, 1995.

[52] R. S. Dembo, S. C. Eisenstat, and T. Steihaug, ‘‘Inexact Newton methods,’’ *SIAM Journal on Numerical Analysis*, vol. 19, pp. 400-408, April 1982.

[53] R. W. Freund and N. M. Nachtigal, ‘‘QMR: a quasi-minimal residual method for non-Hermitian linear systems,’’ *Numerische Mathematik*, vol. 60, pp. 315-339, 1991.

[54] R. W. Freund, ‘‘A transpose-free quasi-minimal residual algorithm for non-Hermitian linear systems,’’ *SIAM Journal on Scientific and Statisitical Computing*, vol. 14, pp. 470-482, March 1993.

[55] R. Barrett, M. Berry, T. F. Chan, J. Demmel, J. M. Donato, J. Dongarra, V. Eijkhout, R. Pozo, C. Romine, and H. Van der Vorst, *Templates for the Solution of Linear Systems: Building Blocks for Iterative Methods*, Philadelphia: SIAM, 1994.

[56] P. N. Brown, A. C. Hindmarsh, and L. R. Petzold, ‘‘Using Krylov subspace methods in the solution of large-scale differential-algebraic systems,’’ *SIAM Journal on Scientific and Statisitical Computing*, vol. 15, pp. 1467-1488, Nov. 1994.

[57] S. E. Laux, ‘‘Techniques for small-signal analysis of semiconductor devices,’’ *IEEE Transactions on Electron Devices*, vol. 32, pp. 2028-2037, Oct. 1986.

[58] B. Troyanovsky et al., ‘‘Preconditioning the harmonic balance equations,’’ in preparation.

[59] D. Sharrit, ‘‘New Method of Analysis of Communication Systems,’’ in *IEEE Microwave Theory and Techniques Symposium WMFA: Nonlinear CAD Workshop*, June 1996.

[60] D. Sharrit, ‘‘Method For Simulating a Circuit,” US Patent No. 5,588,142, granted Dec. 1996.

[61] J. F. Sevic, M. B. Steer, and A. M. Pavio, ‘‘Nonlinear Analysis Methods for the Simulation of Digital Wireless Communication Systems,’’ *International Journal of Microwave and Millimeter-Wave Computer-Aided Engineering*, vol. 6, pp. 197-216, May 1996.

[62] P. Feldmann and J. Roychowdhury, ‘‘Computation of waveform envelopes using an efficient, matrix-decomposed harmonic balance algorithm,’’ *Proc. of the IEEE/ ACM Internation Conference on Computer-Aided Design*, pp. 295-300, Nov. 1996.

[63] H. Keller, *Numerical Solution of Two Point Boundary-Value Problems*, SIAM, 1976.

[64] T. J. Aprille and T. N. Trick, ‘‘Steady-state analysis for nonlinear circuits with periodic inputs,’’ *Proc. of the IEEE*, pp. 108-114, Jan. 1972.

[65] R. Telichevesky, K. Kundert, and J. White, ‘‘Efficient steady-state analysis based on matrix-free Krylov subspace methods,’’ *Proc. of the 32nd Design Automation Conference*, pp. 480-484, June 1995.

[66] R. Telichevesky, K. Kundert, I. Elfadel, and J. White, ‘‘Fast simulation algorithms for RF circuits,’’ *Proc. of the IEEE Custom Integrated Circuits Conference*, pp. 437-444, May 1996.

[67] R. Telichevesky, K. Kundert, and J. White, ‘‘Efficient AC and noise analysis of two-tone RF circuits,’’ *Proc. of the 33rd Design Automation Conference*, pp. 292-297, June 1996.

[68] R. Telichevesky, K. Kundert, and J. White, ‘‘Receiver characterization using periodic small-signal analysis,’’ *Proc. of the IEEE Custom Integrated Circuits Conference*, pp. 449-452, May 1996.

[69] D. O. Pederson and K Mayaram, *Analog Integrated Circuits for Communication*, Kluwer Academic Publishers, 1991.

[70] J. Sato-Iwanaga, private communication.

[71] T. Arnborg, “Modeling and simulation of high speed, high voltage bipolar SOI transistor with fully depleted collector,” *Proc. IEDM*, pp. 743-746, Dec. 1994.

[72] P. Vande Voorde, D. Pettengill, and S.Y. Oh, ‘‘Hybrid simulation and sensitivity analysis for advanced bipolar device design and process development,’’ *Proc. of the IEEE Bipolar Circuits and Technology Meeting*, pp. 114-117, Sep. 1990.

[73] *Mathematica*, Wolfram Research.